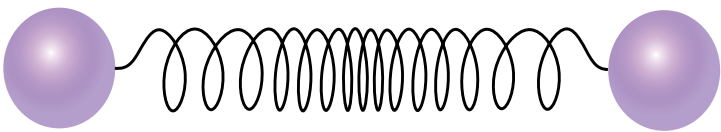
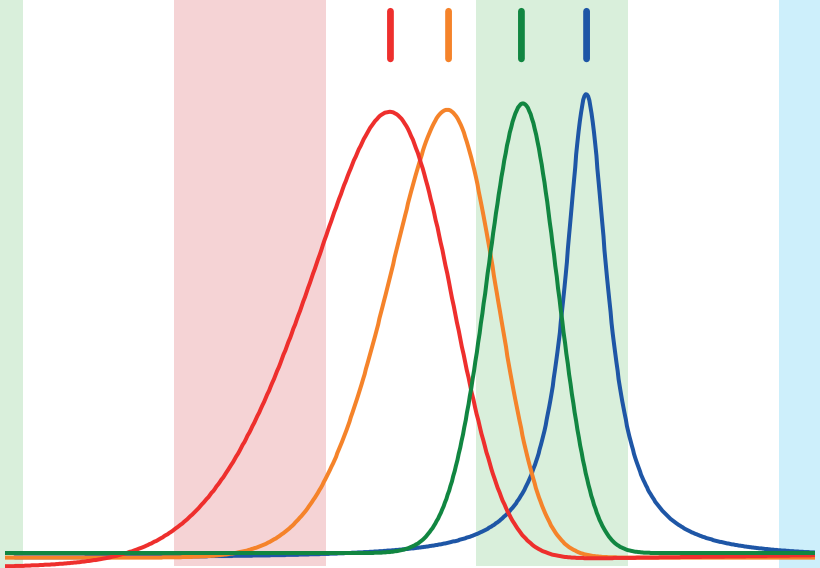


# Precision REMPI and CARS studies on molecular hydrogen and tritium

Madhu Trivikram Talluri



**Precision REMPI and CARS studies on  
molecular hydrogen and tritium**



VRIJE UNIVERSITEIT

# **Precision REMPI and CARS studies on molecular hydrogen and tritium**

ACADEMISCH PROEFSCHRIFT

ter verkrijging van de graad Doctor aan  
de Vrije Universiteit Amsterdam,  
op gezag van de rector magnificus  
prof.dr. V. Subramaniam,  
in het openbaar te verdedigen  
ten overstaan van de promotiecommissie  
van de Faculteit der Bètawetenschappen  
op donderdag 7 februari 2019 om 11.45 uur  
in de aula van de universiteit,  
De Boelelaan 1105

door

**Madhu Trivikram Talluri**

geboren te Narasarao Pet, India

promotor: prof.dr. W.M.G. Ubachs  
copromotor: dr. E.J. Salumbides

This thesis was reviewed by the members of the reviewing committee:  
Prof. Ch. Jungen (Laboratoire Aime Cotton, Orsay, France)  
Prof. dr. K. Jungmann (Rijksuniversiteit Groningen)  
Dr. ir. H.L. Offerhaus (Universiteit Twente)  
Prof. G.H. Raven (Vrije Universiteit)  
Prof. dr. H. B. van Linden van den Heuvel (Universiteit van Amsterdam)



The work was supported by the Vrije Universiteit Amsterdam, and carried out at the LaserLaB of the Vrije Universiteit.



# Contents

<b>1</b>	<b>Introduction</b>	<b>1</b>
1.1	The hydrogen molecule	2
1.2	Tests of molecular theory	3
1.3	Search for physics beyond the Standard Model	6
1.4	Outline and summary of the thesis	8
<b>2</b>	<b>Precision measurements and test of molecular theory in highly-excited vibrational states of <math>H_2</math> (<math>v = 11</math>)</b>	<b>11</b>
2.1	Introduction	12
2.2	Experiment	14
2.2.1	Resonant ionization	18
2.2.2	Frequency calibration	19
2.2.3	Uncertainty estimates	22
2.3	AC-Stark shift and broadening	23
2.3.1	Line shape model	24
2.3.2	AC-Stark coefficients	30
2.4	Results and discussion	33
2.5	Conclusion	34
<b>3</b>	<b>Precision spectroscopy of the <math>EF^1\Sigma_g^+ - X^1\Sigma_g^+</math> system in <math>H_2</math> at large internuclear separation: A combined study of photofragment imaging and autoionization towards labeling and detection</b>	<b>37</b>
3.1	Introduction	39
3.2	Experimental setup	41
3.3	Doppler-free precision spectroscopy on $F - X$ transitions	43
3.3.1	Resonant detection and improved ac-Stark analysis	43
3.3.2	Assignment of the transitions in $F - X(0, 11)$ band	45

3.3.3	Tentative assignments of transitions probing $X(v = 14)$	49
3.4	$H_2^+(v)$ production via photolysis of $H_2S$ : Quantum-state specific kinetics	53
3.5	Autoionization from outer-well levels $F^1\Sigma_g^+$ ( $v = 0, J = 4 - 7$ )	58
3.6	Conclusion	66
<b>4</b>	<b>CARS spectroscopy of the (<math>v = 0 \rightarrow 1</math>) band in <math>T_2</math></b>	<b>67</b>
4.1	Introduction	68
4.2	Experiment	69
4.3	Results and discussion	71
4.4	Conclusion	75
<b>5</b>	<b>Relativistic and QED effects in the fundamental vibration of <math>T_2</math></b>	<b>77</b>
5.1	Introduction	78
5.2	Experimental setup	79
5.3	Frequency calibration of CARS spectra	80
5.4	AC-Stark effect	81
5.5	Results and discussion	85
5.6	Summary and outlook	87
<b>6</b>	<b>Perturbations in the <math>A^1\Pi, v = 0</math> state of <math>^{12}C^{18}O</math> investigated via complementary spectroscopic techniques</b>	<b>89</b>
6.1	Introduction	90
6.2	$2 + 1'$ REMPI laser spectroscopy	92
6.2.1	Experimental details	92
6.2.2	Results	92
6.3	Fourier-transform emission in the visible range (VIS-FT)	94
6.3.1	Experimental details	94
6.3.2	Results	96
6.4	Fourier-transform absorption in the vacuum ultraviolet (VUV-FT)	102
6.4.1	$A^1\Pi \leftarrow X^1\Sigma^+(0,0)$	102
6.4.2	$B^1\Sigma^+ \leftarrow X^1\Sigma^+(0,0)$	108
6.5	Perturbation analysis	110
6.6	Conclusion	117
	<b>Bibliography</b>	<b>119</b>

Contents

**List of publications** 141

**Acknowledgements** 142



---

## Introduction

Spectroscopy is the study of the interaction of electromagnetic radiation with matter. In the nineteenth century, early spectroscopic experiments by Fraunhofer observed a set of dark absorption features in the visible part of the solar spectrum, now called 'Fraunhofer lines.' Balmer and Rydberg gave the first mathematical description for the observed spectral lines of the hydrogen atom. This was followed by Planck's quantum interpretation for the observed intensity distribution of blackbody radiation as a function of wavelength that had led to the advent of modern spectroscopy. Planck's quantum hypothesis formed the basis for the Bohr model of the Hydrogen atom suggesting the quantization of its energy level structure. According to Bohr, electromagnetic radiation is either emitted or absorbed by an atom only when the energy of the light quantum (photon) is precisely equal to the energy difference between two levels ( $E_i$  and  $E_f$ ),

$$|\Delta E_{fi}| = |E_f - E_i| = h\nu_{fi} \quad (1.1)$$

where  $h$  is Planck's constant and  $\nu_{fi}$  is the frequency of the photon. This quantization condition forms the foundation of line-resolved spectroscopy for understanding the structure of atomic and molecular systems. Subsequently, the development of quantum mechanics with the seminal works of Heisenberg, Schrödinger, and Dirac have provided the understanding of the internal structure of atoms and molecules. Currently, high-resolution molecular spectroscopy with the aid of these theoretical frameworks unravel the

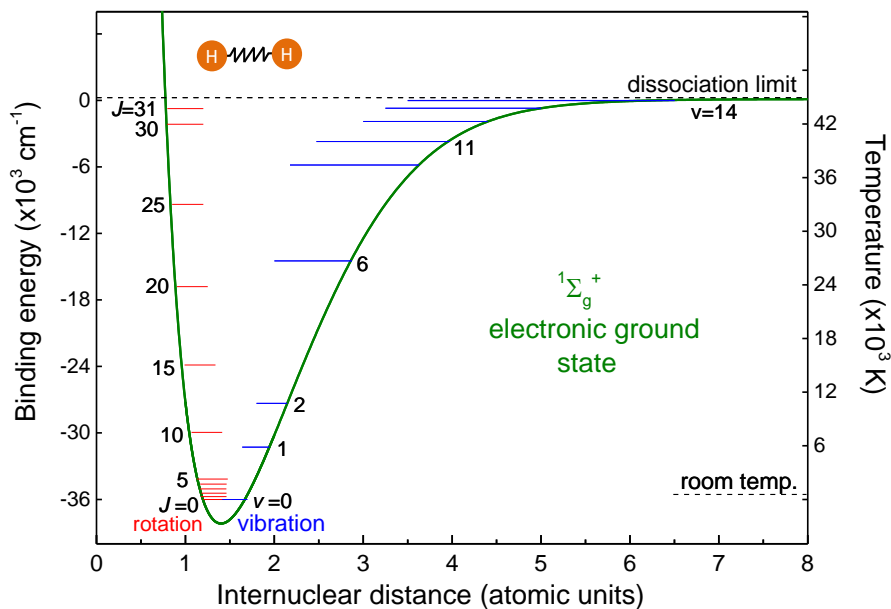


**Figure 1.1** Potential energy curve of the electronic ground state of H<sub>2</sub> molecule.

fundamental physics aspects embedded in the quantum level structure of molecules.

## 1.1 The hydrogen molecule

H<sub>2</sub> is the simplest neutral molecule in which two protons are held together by a surrounding charge cloud of two electrons. Quantum mechanically, the hydrogen molecule may be described as a linear combination of atomic orbitals of two H(1s) atoms where the electronic state can be represented by a unified stable *bonding* molecular orbital ( $1s\sigma_g$ )<sup>2</sup>. According to the Heitler-London theory for H<sub>2</sub>, the reason for the strong attraction of H atoms lies in the exchange degeneracy that is present when the atoms are separated at large internuclear distances due to their indistinguishable original elec-

tronic configurations. As the two atoms approach each other within a few Bohr radii ( $a_0$ ), an electron exchange interaction causes the overlap of their wavefunctions and then leads to splitting into two states of different energies. These exchange interactions form an attractive potential for the antiparallel spin configuration in accordance with Pauli exclusion principle [1].

In diatomic molecules, there are two additional modes of motion *i.e.* vibration and rotation of the nuclei. Due to their heavy mass, the nuclei move very slowly compared to electrons and this leads to an hierarchy in their internal energy structure,  $E_{mol}$ ; first electronic ( $E_{el}$ ), then vibrational ( $E_{vib}$ ), and finally rotational energy ( $E_{rot}$ ), as shown in figure 1.1.

$$E_{mol} = E_{el} + E_{vib} + E_{rot} \quad (1.2)$$

Molecular theory predicts the existence of 302 ro-vibrational bound states in the electronic ground state of  $H_2$  before it dissociates into two individual H-atoms. Following the Boltzmann population distribution only the first 5 rotational states have a significant probability to be populated at room temperature.

## 1.2 Tests of molecular theory

Due to the simplicity of the hydrogen molecule, its internal electronic energy structure can to a large extent be accounted for using first principles: starting with the Born-Oppenheimer (BO) approximation [2]. The  $E_{BO}$  term in eq.(1.2) essentially decouples the motion of electrons from that of the nuclei, as the fast-moving and light electrons instantaneously respond to the slower vibrational and rotational motion of the heavy nuclei.

$$E_{level} = E_{BO} + E_{AD} + E_{NAD} + \mathcal{O}(\mu^{-n}) \quad (1.3)$$

Due to the finite nuclear mass, however, electrons follow the motion of nuclei adiabatically, and hence the molecule remains in the same electronic state [3]. The adiabatic term,  $E_{AD}$ , is a correction to the BO term that is less than three orders smaller and scales with the electron-to-nucleus mass ratio, ( $m_e/\mu$ ) where  $\mu$  is the reduced mass of the nuclei. These mass-dependent corrections are treated, in general, using a perturbative approach. Similarly, the leading order non-adiabatic effects,  $E_{NAD}$ , are derived from second-order perturbation theory to quantify the coupling between electron and nuclear

motion which is ignored in the earlier BO case [3].  $\mathcal{O}(\mu^{-n})$  represents mass-dependent higher  $n$ th-order corrections in non-adiabatic perturbation treatment. Until this point, the molecular level structure is discussed in the framework of non-relativistic quantum mechanics and the non-relativistic Schrödinger equation for this four body system is numerically solved with an accuracy of  $10^{-7} \text{ cm}^{-1}$  [4–6].

Despite the high degree of accuracy obtained in the non-relativistic framework, electrons moving in the vicinity of nuclei should be treated relativistically [7]. For the Hydrogen atom, the most probable distance between electron and nucleus is given by

$$a_0 = \frac{\hbar}{m_e c \alpha} \quad (1.4)$$

where  $a_0$  is the Bohr radius,  $\hbar$  is the reduced Planck's constant and  $c$  is the velocity of light. Due to its relativistic motion, the electron's relativistic gain in mass increases its binding energy as it moves closer to the atomic nucleus. Here  $\alpha$  is the fine structure constant and can be formulated as

$$\alpha = \frac{e^2}{4\pi\epsilon_0\hbar c} \quad (1.5)$$

where  $\epsilon_0$  is the permittivity of the vacuum. Apart from relativistic mass dependence, there are other relativistic contributions: the interaction between spin and orbital angular momenta of the electron, and the Darwin term which smears the effective potential seen by the electron. For the ground state (1s) of H-atom there is no spin-orbit coupling, but the Darwin correction is maximum for the  $\ell = 0$  orbital [7]. These relativistic contributions were extended to a compound system, the hydrogen molecule and calculated by computing the expectation value of the Breit-Pauli Hamiltonian operator [8, 9]. The binding energies for the rovibrational levels of the electronic ground state,  $\text{H}_2 \ ^1\Sigma_g^+$ , are slightly reduced due to the relativistic effects [8, 10]. At this juncture, the energy levels of hydrogen molecule can be precisely expressed in terms of  $\alpha$  [10],

$$E_{level}(\alpha) = E^{(0)} + E^{(2)}\alpha^2 + E^{(3)}\alpha^3 + E^{(4)}\alpha^4 + \dots \quad (1.6)$$

where  $E^{(0)}$  is the non-relativistic energy given eq. (1.3).  $E^{(2)}\alpha^2$  is the Dirac term which deals with relativistic and fine structure effects.

The next higher-order terms ( $\alpha^3 E^{(3)}, \alpha^4 E^{(4)}, \dots$ ), in the expression (1.6) are due to subtle quantum electrodynamics (QED) effects [11, 12]. These QED

contributions arise because of the electron's self energy and vacuum polarization. The former corresponds to the emission and reabsorption of virtual photons by the electron, and the latter is ascribed to the creation and the annihilation of virtual electron-positron pairs. In a nutshell, an electron interacts with the zero-point energy of the vacuum field that results from the quantization of the electromagnetic field as prescribed by QED theory. This interaction induces the electron's position to fluctuate and modifies the Coulomb potential experienced by the electron. For  $1s$  atomic orbital, QED effects slightly reduce the binding energy of the electron. This translates into more smearing out of the electron cloud and thus a slight reduction in binding energy of rovibrational levels of  $H_2$ . These effects are calculated perturbatively and are proportional to  $(Z\alpha^2)\alpha^3$  or simply  $E^{(3)}\alpha^3$  for the first order. The fine structure constant  $\alpha$ , introduced in eq.(1.5) describes the interaction strength between photon and electron, and thus it is one of the most important dimensionless fundamental constants in nature [13]. These radiative corrections, in general for atoms and molecules, are evaluated in the non-relativistic formalism of QED (NRQED), as bound electrons move at considerably lower velocities than that of photons. Together, relativistic and QED effects contribute at the  $10^{-5}$  level to the binding energy of  $H_2$  for its ground state,  $X(v=0, J=0)$  [10].

Ever since the Heitler-London approximation, significant improvements have been made to molecular theory. Starting with the basis wavefunctions developed by James-Coolidge [14] and aided by rapid progress in computational power, many significant contributions have been made by Kolos [15–17] and Wolniewicz [16, 18, 19] using first principles. The ground state potential has been refined to include relativistic and radiative corrections. In recent years Pachucki and coworkers have performed calculations including higher order QED effects to the order of  $m\alpha^6$  or  $E^{(4)}\alpha^6$  term in the expansion (1.6) which accounts for the two-loop self energy term [20, 21].

The quest for accurate calculations has been stimulated by tremendous strides in ever increasing experimental precision. Ever since the advent of laser-based spectroscopic measurements, experimental precision has outpaced theoretical accuracy. For example, in the case of dissociation energy  $D_0(H_2)$ , there has been an excellent agreement between precision spectroscopic measurements and *ab initio* calculations up to a few p.p.b. level [22]. The experimental accuracy, in that case, was an order better than then existing theoretical uncertainty. Later, experimental investigations also quantified rela-

tivistic, and QED contributions in the progression of rotational quantum states ( $J = 0 - 16$ ) in the vibrational ground ( $v = 0$ ) state of  $\text{H}_2$  [23] and were found to be in good agreement with theory. Precision spectroscopic measurements were further extended to measure the fundamental vibrational splitting ( $v = 0 \rightarrow 1$ ) of hydrogen and its deuterated isotopologues and the measurements coincide within  $1\sigma$  uncertainty with *ab initio* calculations at  $2 \times 10^{-4} \text{ cm}^{-1}$  level [24]. At this level of agreement, molecular theory attempts to address queries related to physics beyond the Standard Model, which is briefly explained in the following section.

This thesis work extends the precision spectroscopic measurements on the  $\text{H}_2$  molecule in two different directions: (i) probing the quantum states at large internuclear separation  $\sim 4$  a.u., and (ii) probing the fundamental vibrational quantum splitting of its heaviest isotopologue,  $\text{T}_2$ .

### 1.3 Search for physics beyond the Standard Model

The Standard Model of physics provides a theoretical description for fundamental particles and how they interact via the fundamental forces in nature i.e. electromagnetic, strong and weak interactions. The gravitational interaction is not included within this framework. The gravitational force between two protons is negligible and is  $10^{37}$  times weaker than electromagnetic force between them. The strong interactions are confined to nuclear length (femtometer) scales and can be completely ignored at Ångström length scales corresponding to molecular bond lengths. However, the nuclear spin ( $I_N$ ) interacts with that of the electrons leading to hyperfine splitting of energy levels. In addition to this, the finite nuclear size or nuclear charge radius effects also modify the wavefunction of the electron due its non-zero probability inside the nucleus and causes a shift in its binding energy [25]. These nuclear structure effects contribute in the order of  $10^{-6} \text{ cm}^{-1}$  to the rovibrational level energies of  $\text{H}_2$  [10]. The weak interaction, which influences fermions in SM contributes only at the Hz level in electronic transitions for the hydrogen atom and are assumed to contribute in similar order for  $\text{H}_2$  [26].

The molecular theory that is explained in the previous section, has been developed in the framework of NRQED which works in the realm of electromagnetic interactions. Precision molecular spectroscopic studies on rovibrational level energies of neutral hydrogen molecules and its deuterated isotopologues are in excellent agreement with *ab initio* calculations and provide

a stringent test on applicability of quantum electrodynamics in chemically bound systems [22, 24, 27]. In other words, these studies serve as test of the Standard Model of physics at atomic length scales. In most of the cases the discrepancy between experiment and calculations ( $\Delta E$ ) has been verified to be less than the quadrature ( $\delta E$ ) of combined uncertainties in experiment ( $\delta E_{exp}$ ) as well as theory ( $\delta E_{calc}$ ) [28].

$$\begin{aligned} \delta E &= \sqrt{\delta E_{exp}^2 + \delta E_{calc}^2} \\ \Delta E &< \delta E \end{aligned} \quad (1.7)$$

With this conclusion,  $\delta E$  can serve as a limit to constrain effects of physics beyond Standard Model.

The manifestation of a hypothetical fifth force between two hadrons can be parameterized using a Yukawa-like potential [29]

$$V_5(R) = \alpha_5 N_1 N_2 \frac{\exp(-R/\lambda_5)}{R} \hbar c \quad (1.8)$$

where  $\alpha_5$  is the coupling strength of this force analogous to the previously described fine structure constant,  $\alpha$ , for electromagnetic interactions and  $\lambda$  is the range of the interaction. Using interpretations of quantum field theory, this force is mediated by the exchange of a hypothetical force-carrying bosonic particle of mass  $m_5 = \hbar/\lambda_5 c$ .  $N_1$  and  $N_2$  represent the nucleon numbers for each hadron. For example,  $N = 1$  for the proton,  $N = 2$  for the deuteron, and  $N = 3$  for the triton. The latter makes the tritium molecule ( $T_2$ ) a more sensitive test ground than the lighter isotopologues.

Interactions of this kind can be anticipated between two hadronic nuclei that are bound on the Ångström scale within a simple diatomic molecule like  $H_2$  and its isotopologues. The expectation value of a fifth force on the energy of molecular state  $\psi_{vJ}(R)$  can be expressed as

$$\langle V_5(R) \rangle = \alpha_5 N_1 N_2 \langle Y_\lambda \rangle \hbar c \quad (1.9)$$

where

$$\langle Y_\lambda \rangle = \left\langle \psi_{vJ}(R) \left| \frac{\exp(-R/\lambda_5)}{R} \right| \psi_{vJ}(R) \right\rangle \hbar c \quad (1.10)$$

and  $R$  is the inter-hadronic or internuclear distance. The expectation values can be numerically evaluated for various rovibrational levels using the exact wavefunctions  $\psi_{vJ}(R)$  developed by Pachucki and co-workers [8, 10, 30].

Fifth force contributions to molecular transition frequencies ( $\Delta Y_\lambda$ ) are obtained by taking the differences in expectation values for ground ( $\psi_{v''J''}(R)$ ) and excited states ( $\psi_{v'J'}(R)$ ). The difference between the precision spectroscopic measurement and *ab initio* calculations for the transition energy can be used to limit the contribution to a fifth force. Constraints on its coupling strength can be formulated as

$$\alpha_5 < \frac{\delta E}{N_1 N_2 \Delta Y_\lambda} \quad (1.11)$$

Based on the combined analysis of various molecular transitions, at present, the fifth forces are constrained to be at least a billion times weaker than electromagnetic force, *i.e.*  $\alpha_5/\alpha < 10^{-9}$  [28, 29]. Suggestions have been made to expand the parameter space and improve the sensitivity and hence derive tighter constraints [31].

## 1.4 Outline and summary of the thesis

In this thesis Chapter 2 focusses on precision measurements on large amplitude vibrations of nuclei, especially on the  $X^1\Sigma_g^+(v = 11)$  state of  $\text{H}_2$ . Due to the proximity of these vibrational levels to the excited electronic states, the non-adiabatic contributions increase by more than an order compared to that for the vibrational ground state  $X(v = 0)$  [10, 32]. This also leads to higher theoretical uncertainties, which are greater than  $5 \times 10^{-3} \text{ cm}^{-1}$ , for the binding energies of  $v = 8 - 11$  compared to those of  $1 \times 10^{-3} \text{ cm}^{-1}$  for  $v = 0$ . Due to the lack of an electric dipole moment in homonuclear molecules like  $\text{H}_2$ , these states cannot be populated by direct optical means. Instead, we employ photochemical routes to generate vibrationally-hot neutral hydrogen molecules [33]. It has been demonstrated that two-photon photodissociation of  $\text{H}_2\text{S}$  molecule at 290 nm produces  $\text{H}_2^*(v = 10 - 14)$  among other pathways. Subsequently, the nascent photoproduct  $\text{H}_2^*(v)$  is subjected to the high resolution  $2 + 1$  Doppler-free REMPI spectroscopy on  $F - X$  electronic transitions to determine accurate level energies for  $X, v = (11, J)$ , similar to earlier studies [23, 24, 34]. These experimental results are in  $1\sigma$  agreement with first principle calculations including relativistic and QED contributions, while the achieved experimental accuracy ( $\sim 45 \text{ MHz}$ ) is three times better than that of the calculations [35].

Chapter 3 revisits the precision measurements on  $E, F - X$  transitions in  $\text{H}_2$  at an internuclear separation of  $R \sim 4 \text{ a.u.}$  This chapter describes the pre-

liminary preparation step, i.e., the photolysis of the precursor molecule, and the final detection stage of resonant ionization scheme. The photofragment imaging method is implemented for the photodissociation of  $\text{H}_2\text{S}$  to understand the quantum state specific kinetics of photoproducts. An approach to determine the vibrational quantum specifics of  $\text{H}_2^*(v)$  from the velocity map imaging of  $\text{H}_2^+$  ions produced in the REMPI scheme is presented. The role of autoionization resonances to greatly reduce the ac-Stark effect in  $2+1$  REMPI precision spectroscopic measurements, and to assign few unknown  $F-X$  transitions using the combinational differences is explained. Finally, the chapter attempts to understand the Rydberg structure of  $\text{H}_2$  at  $R \geq 4$  a.u. from the autoionization spectra recorded from a doubly excited outer-well state for the first time. The interpretation of the high lying molecular Rydberg level structure covered by present studies would require extensions to the multichannel quantum defect theory (MQDT) to provide a numerical simulation of photoionization spectra..

In Chapter 4 and 5, precision studies are extended to the fundamental vibrational tone of the tritium molecule, the heaviest and radioactive isotope of hydrogen. Spectroscopic investigations on a  $\text{T}_2$  gas sample are facilitated by a collaboration between VU-LaserLaB Amsterdam and Karlsruhe Institute of Technology (KIT), Germany. Unlike studies in the previous chapters, molecular beam methods cannot be implemented for  $\text{T}_2$  due to its radioactive nature. Like  $\text{H}_2$ ,  $\text{T}_2$  also does not possess an electric dipole moment, and thus, the non-linear spectroscopic technique of Coherent Anti-Stokes Raman Spectroscopy (CARS) is employed to measure its fundamental vibrational splitting ( $v = 0 \rightarrow 1$ ). Chapter 4 discusses the importance of spectroscopic measurements on  $\text{T}_2$ , handling of a tritium gas cell and recording of its CARS spectrum using a broadband pulsed dye laser (PDL) source. Transition energies  $Q(J = 0 - 5)$  are determined with an accuracy of  $0.02 \text{ cm}^{-1}$ , which is a fivefold improvement over earlier studies on  $\text{T}_2$  and are in good agreement with nonrelativistic calculations [36]. Further improvement to these transitions is achieved by implementing high resolution CARS studies using a transform-limited narrowband pulsed dye amplifier (PDA) system. These are described in Chapter 5. Line positions are determined with an experimental uncertainty of  $4 \times 10^{-4} \text{ cm}^{-1}$  through careful application of frequency calibration procedures and systematic analysis of the ac-Stark effect. This unprecedented accuracy enables us for the retrieval of relativistic and QED effects in the fundamental vibration of  $\text{T}_2$  experimentally for the first

time [37]. These studies provide an impetus for *ab initio* molecular theory which is yet to account for relativistic and radiative effects for tritiated isotopologues.

In addition spectroscopic investigations on these two different systems ( $\text{H}_2$  and  $\text{T}_2$ ) does not only provide a stringent test on QED theory, but also help to increase the parameter space for searching for physics beyond Standard Model as explained in section 1.3. The precision measurements on  $X(v = 11)$  of  $\text{H}_2$ , corresponding to the vibrational splitting of  $\Delta v = 11$  or  $v = 0 \rightarrow 11$  transition would show better sensitivity for probing fifth force contributions ( $\langle \Delta V_5 \rangle \propto \Delta Y_\lambda$ ) compared to those on the fundamental vibration splitting  $v = 0 \rightarrow 1$ . This is because in the former case the spatial extent of the wavefunction is increased by more than a factor five from the equilibrium position [29]. The splitting  $v = 0 \rightarrow 11$  is observed to be consistent with QED theory from the molecular theory based on the average deviation over four rovibrational levels ( $\Delta E \sim \delta E \sim 0.0056 \text{ cm}^{-1}$ ). When it comes to  $\text{T}_2$ , the inherent sensitivity for hypothetical fifth forces is increased by almost an order of magnitude compared to  $\text{H}_2$  following the equation (1.8) where  $N_1 N_2 = 9$  with the addition of two nucleons on each triton nucleus. However, at this moment tests for new physics on  $\text{T}_2$  are hampered due to the lack of fully relativistic calculations.

Finally, Chapter 6 discusses perturbations in diatomic molecules due to non-Born-Oppenheimer vibronic interactions among different electronic states. The CO molecule has become the benchmark system for understanding these effects. A detailed analysis of various perturbations in the  $A^1\Pi(v = 0)$  state of  $^{12}\text{C}^{18}\text{O}$  molecule is presented. Accurate level energies of  $A^1\Pi(v = 0)$  and  $B^1\Sigma^+(v = 0)$  are determined by employing three complementary spectroscopic methods —(i) Doppler-free two-photon laser on  $A^1\Pi - X^1\Sigma^+(0,0)$  band (VU-LaserLaB Amsterdam), (ii) Fourier-transform emission spectroscopy in the visible range on  $B^1\Sigma^+ - A^1\Pi(0,0)$  band (University of Rzeszów, Poland), and (iii) One photon Fourier-transform absorption spectroscopy in the VUV range on  $A - X(0,0)$  and  $B - X(0 - 0)$  bands (SOLEIL synchrotron, France). Many optically forbidden extra/perturber lines are identified due to spin-orbit and rotational-electronic ( $L$ -uncoupling) interaction of  $A^1\Pi$  state with triplet states,  $d^3\Delta$ ,  $e^3\Sigma^-$ , and  $a^3\Sigma^+$ . The deperturbed term origin of  $A^1\Pi(v = 0)$  is determined with a precision of  $0.001 \text{ cm}^{-1}$  which can be compared with the isotope shift in  $A - X(0,0)$  band of other isotopologues [38–43].

---

## Precision measurements and test of molecular theory in highly-excited vibrational states of $\text{H}_2$ ( $v = 11$ )

### Abstract

Accurate  $EF^1\Sigma_g^+ - X^1\Sigma_g^+$  transition energies in molecular hydrogen were determined for transitions originating from levels with highly-excited vibrational quantum number,  $v = 11$ , in the ground electronic state. Doppler-free two-photon spectroscopy was applied on vibrationally excited  $\text{H}_2^*$ , produced via the photodissociation of  $\text{H}_2\text{S}$ , yielding transition frequencies with accuracies of 45 MHz or  $0.0015 \text{ cm}^{-1}$ . An important improvement is the enhanced detection efficiency by resonant excitation to autoionizing  $7p\pi$  electronic Rydberg states, resulting in narrow transitions due to reduced ac-Stark effects. Using known  $EF$  level energies, the level energies of  $X(v = 11, J = 1, 3 - 5)$  states are derived with accuracies of typically  $0.002 \text{ cm}^{-1}$ . These experimental values are in excellent agreement with, and are more accurate than the results obtained from the most advanced *ab initio* molecular theory calculations including relativistic and QED contributions.

## 2.1 Introduction

The advance of precision laser spectroscopy of atomic and molecular systems has, over the past decades, been closely connected to the development of experimental techniques such as tunable laser technology [44], saturation spectroscopy [45], two-photon Doppler-free spectroscopy [46], cavity-locking techniques [47], and ultimately, the invention of the frequency comb laser [48], developments to which Prof. Theodore Hänsch has greatly contributed. These inventions are being exploited to further investigate at ever-increasing precision the benchmark atomic system – the hydrogen atom, evinced by the advance in spectroscopic accuracy of atomic hydrogen measurements by more than seven orders of magnitude since the invention of the laser [49]. The spectroscopy of the 1S-2S transition in atomic hydrogen, at  $4 \times 10^{-15}$  relative accuracy [50], provides a stringent test of fundamental physical theories, in particular quantum electrodynamics (QED). Currently, the theoretical comparison to precision measurements on atomic hydrogen are limited by uncertainties in the proton charge radius  $r_p$ . The finding that the  $r_p$ -value obtained from muonic hydrogen spectroscopy is in disagreement by some  $7\text{-}\sigma$  [51] is now commonly referred to as the *proton-size puzzle*.

Molecular hydrogen, both the neutral and ionic varieties, are benchmark systems in molecular physics, in analogy to its atomic counterpart. Present developments in the *ab initio* theory of the two-electron neutral  $\text{H}_2$  molecule and the one-electron ionic  $\text{H}_2^+$  molecule, as well as the respective isotopologues, have advanced in accuracy approaching that of its atomic counterpart despite the increased complexity. The most accurate level energies of the entire set of rotational and vibrational states in the ground electronic state of  $\text{H}_2$  were calculated by Komasa *et al.* [10]. An important breakthrough in these theoretical studies was the inclusion of higher-order relativistic and QED contributions, along with a systematic assessment of the uncertainties in the calculation. Recently, further improved calculations of the adiabatic [5] as well as non-adiabatic [52] corrections have been performed, marking the steady progress in this field.

In the same spirit as in atomic hydrogen spectroscopy, the high-resolution experimental investigations in molecular hydrogen are aimed towards confronting the most accurate *ab initio* molecular theory. For the  $\text{H}_2^+$  and  $\text{HD}^+$  ions, extensive efforts by Korobov and co-workers over the years, have recently led to the theoretical determination of ground electronic state level en-

## Introduction

ergies at 0.1 ppb accuracies [53]. The latter accuracy enables the extraction of the proton-electron mass ratio,  $m_p/m_e$ , when combined with the recent HD<sup>+</sup> spectroscopy using a laser-cooled ion trap [54]. These are currently at lower precision than other methods but prospects exist that competitive values can be derived from molecular spectroscopy. Similarly Karr *et al.* [55] recently discussed the possibility of determining  $R_\infty$  using H<sub>2</sub><sup>+</sup> (or HD<sup>+</sup>) transitions as an alternative to atomic hydrogen spectroscopy. Even for the neutral system of molecular hydrogen, the determination of  $r_p$  from spectroscopy is projected to be achievable, from the ongoing efforts in both calculation [4] and experiments [28]. Molecular spectroscopy might thus be posed to contribute towards the resolution of the proton-size puzzle.

In contrast to atomic structure, the added molecular complexity due to the vibrational and rotational nuclear degrees of freedom could constitute an important feature, with a multitude of transitions (in the ground electronic state) that can be conscripted towards the confrontation of theory and experiments. From both experimental and theoretical perspectives, this multiplicity allows for consistency checks and assessment of systematic effects. In recent years, we have tested the most accurate H<sub>2</sub> quantum chemical calculations using various transitions, for example, the dissociation limit  $D_0$  or binding energy of the ground electronic state [22]; the rotational sequence in the vibrational ground state [23]; and the determination of the ground tone frequency ( $v = 0 \rightarrow 1$ ) [24]. The comparisons exhibit excellent agreement thus far, and have in turn been interpreted to provide constraints of new physics, such as fifth-forces [29] or extra dimensions [56].

Recently, we reported a precision measurement on highly-excited vibrational states in H<sub>2</sub> [32]. The experimental investigation of such highly-excited vibrational states probe the region where the calculations of Komasa, Pachucki and co-workers [10] are the least accurate, specifically in the  $v = 6 - 12$  range. The production of excited H<sub>2</sub><sup>\*</sup> offers a unique possibility on populating the high-lying vibrational states, that would otherwise be practically inaccessible by thermodynamic means (corresponding temperature of  $T \sim 47,000$  K for  $v = 11$ ).

Here, we present measurements of level energies of  $v = 11$  rovibrational quantum states that extend the spectroscopy in Ref [32] and that implement improvements, leading to a narrowing of the resonances. This is achieved by the use of a resonant ionization step to molecular Rydberg states, thereby enhancing the detection efficiency significantly. The enhancement allows for

the use of a low intensity spectroscopy laser minimizing the effect of ac-Stark induced broadening and shifting of lines. The ac-Stark effect is identified as the major source of systematic uncertainty in the measurements, and a detailed treatment of this phenomenon is also included in this contribution.

## 2.2 Experiment

The production of excited  $\text{H}_2^*$  from the photodissociation of hydrogen sulfide was first demonstrated by Steadman and Baer [33], who observed that the nascent  $\text{H}_2^*$  molecules were populated at predominantly high vibrational quanta in the two-photon dissociation of  $\text{H}_2\text{S}$  at UV wavelengths. That study used a single powerful laser for dissociation, for subsequent  $\text{H}_2$  spectroscopy, and to induce dissociative ionization for signal detection. Niu *et al.* [32] utilized up to three separate laser sources to address the production, probe, and detection steps in a better controlled fashion. The present study, targeting  $\text{H}_2(v = 11)$  levels, is performed using the same experimental setup as in Ref. [32], depicted schematically in Fig. 3.2. The photolysis laser at 293 nm, generated from the second harmonic of the output of a commercial pulsed dye laser (PDL) with Rhodamine B dye, serves in the production of  $\text{H}_2^*$  by photolysing  $\text{H}_2\text{S}$ . The narrowband spectroscopy laser radiation at around 300–304 nm is generated by frequency upconversion of the output of a continuous wave (cw)-seeded pulsed dye amplifier system (PDA) running on Rhodamine 640 dye. The ionization laser source at 302–305 nm, from the frequency-doubled output of another PDL (also with Rhodamine 640 dye), is used to resonantly excite from the  $EF$  to autoionizing Rydberg states to eventually form  $\text{H}_2^+$  ions. This  $2 + 1'$  resonance-enhanced multiphoton ionization (REMPI) scheme results in much improved sensitivities compared to our previous study [32].

The  $\text{H}_2\text{S}$  molecular beam, produced by a pulsed solenoid valve in a source vacuum chamber, passes through a skimmer towards a differentially pumped interaction chamber, where it intersects the laser beams perpendicularly. The probe or spectroscopy laser beam is split into two equidistant paths and subsequently steered in a counter-propagating orientation, making use of a Sagnac interferometer alignment for near-perfect cancellation of the residual first-order Doppler shifts[57]. Moreover, the probe laser beams pass through respective lenses, of  $f = 50$ -cm focal length, to focus and enhance the probe intensity at the interaction volume. Finally, the ionization beam is aligned

## Experiment

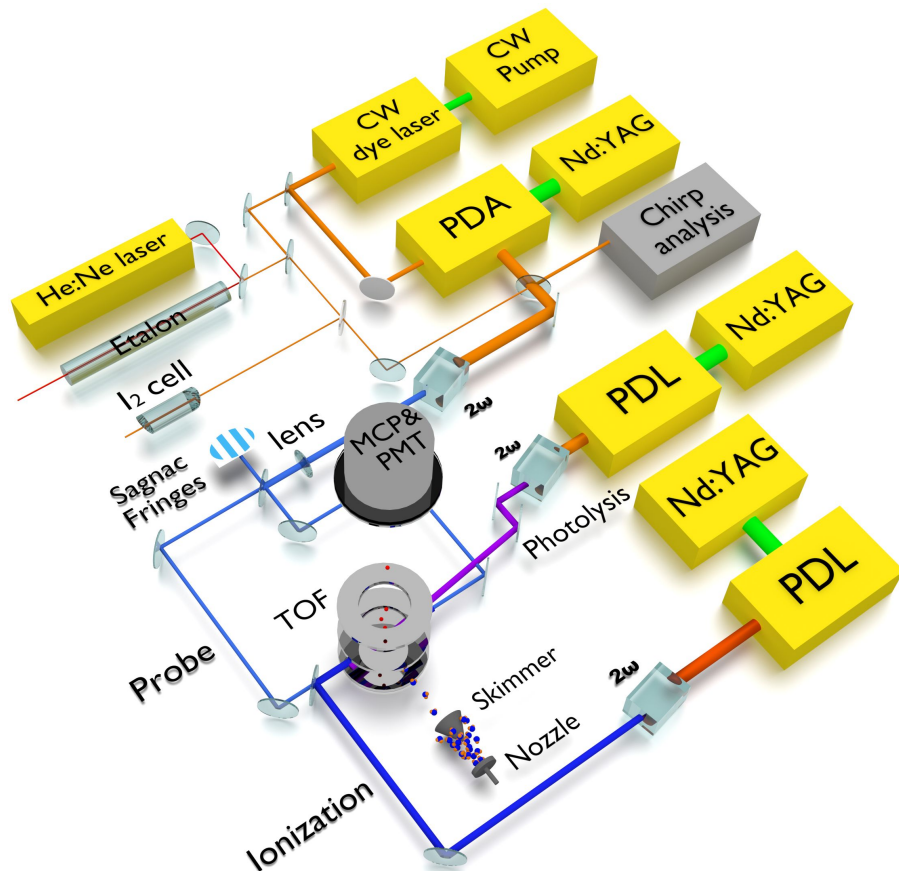


**Figure 2.1** Schematic of experimental setup indicating the three main radiation sources: the *photolysis* laser at 293 nm for  $\text{H}_2^+$  production from  $\text{H}_2\text{S}$  dissociation; the *probe* laser from a narrowband dye amplifier (PDA) for the  $EF-X$  spectroscopy transition; and the *ionization* laser for resonant  $\text{H}_2^+$  ion production, subsequently detected as signal. Doppler-free two-photon excitation is facilitated by the Sagnac interferometric alignment of the counter-propagating probe beams. Absolute frequency calibration is performed with respect to  $\text{I}_2$  hyperfine reference lines, aided by the relative frequency markers from the transmission fringes of a length-stabilized Fabry-Pérot etalon. The frequency offset between the cw-seed and PDA pulse output, induced by chirp effects in the dye amplifier, is measured and corrected for, post-measurement. [cw: continuous wave; PDL: pulsed dye laser;  $2\omega$ : frequency-doubling stage; TOF: time-of-flight region; MCP: multichannel plates; PMT: photomultiplier tube]

in almost co-linear fashion with the other laser beams to ensure maximum spatial overlap. To avoid ac-Stark shifts during the spectroscopic interrogation, induced by the photolysis laser ( $\sim 6$  mJ typical pulse energy;  $\sim 10$ -ns pulse duration), a 15-ns delay between the photolysis and probe pulses is established with a delay line. For a similar reason, the ionization pulse ( $\sim 1$  mJ typical pulse energy;  $\sim 10$ -ns pulse duration) is also delayed by 30 ns with respect to the probe pulse. The 1 mJ ionization pulse energy is sufficient for saturating the ionization step.

The ions produced in the interaction volume are accelerated by ion lenses, further propagating through a field-free time-of-flight (TOF) mass separation region before impinging on a multichannel plate (MCP) detection system. Scintillations in a phosphor screen behind the MCP are monitored by a photomultiplier tube (PMT) and a camera, culminating in the recording of the mass-resolved signals. In the non-resonant ionization step as in Ref. [32], predominantly  $\text{H}^+$  ions were produced and were thus used as the signal channel for the  $EF - X$  excitation. In contrast, the resonant ionization scheme employed here predominantly produces  $\text{H}_2^+$  ions. In addition to the enhancement of sensitivity, the  $\text{H}_2^+$  channel offers another important advantage as it is a background free channel, whereas the  $\text{H}^+$  channel includes significant contributions from  $\text{H}_2\text{S}$ , as well as  $\text{SH}$ , dissociative ionization products. To avoid dc-Stark effects on the transition frequencies, the acceleration voltages of the ion lens system are pulsed and time-delayed with respect to the probe laser excitation.

Niu *et al.* [32] confirmed the observation of  $\text{H}_2$  two-photon transitions in various  $EF - X$  ( $v', 10-12$ ) bands, first identified by Steadman and Baer [33], but only for transitions to the outer  $F$ -well of the  $EF$  electronic potential in  $\text{H}_2$ . Franck-Condon factor (FCF) calculations, to assess the transition strengths of the photolysis-prepared levels of  $X(v'')$  to levels in the combined inner ( $E$ ) and outer ( $F$ ) wells of the  $EF$  double well potential, were performed by Fantz and Wunderlich [58, 59]. While Niu *et al.* [32] performed precision measurements probing the  $X(v'' = 12)$  levels, presently  $X(v'' = 11)$  levels are probed. Note that for the excited state two different numberings of vibrational levels exist: one counting the levels in the combined  $EF$  well, and the other counting the levels in the  $E$  and  $F$  wells separately. Then  $EF(v' = 5)$  corresponds to  $F(v' = 3)$ , while  $EF(v' = 1)$  corresponds to  $F(v' = 0)$ . In the following, we will refer to the vibrational assignments following the  $F$ -well notation. The FCF for the  $F - X(3, 12)$  band, used in Ref. [32], amounts to

## Experiment

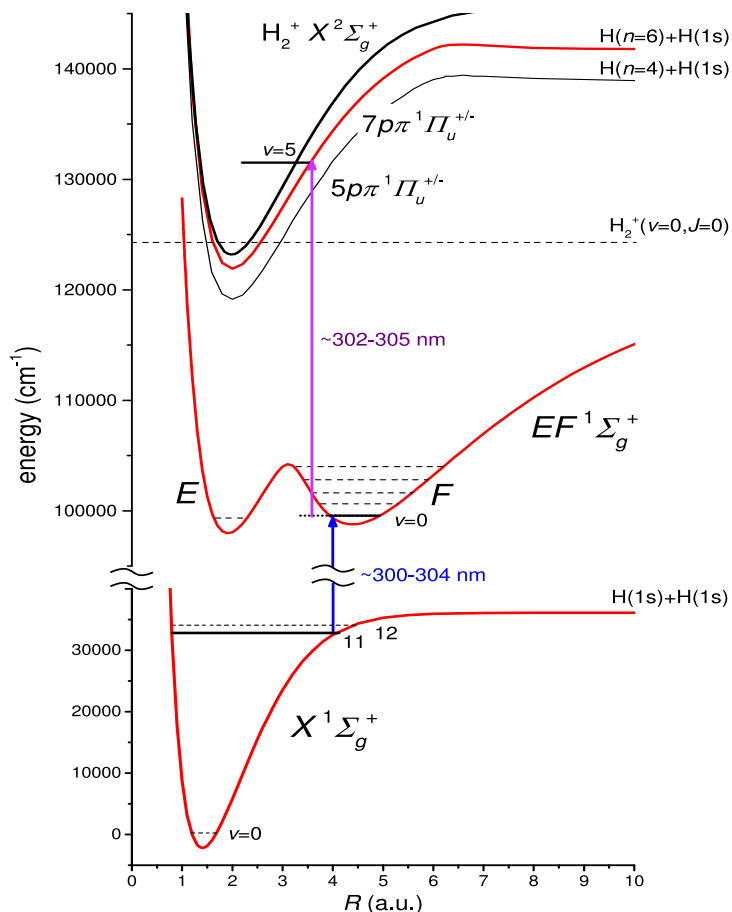


**Figure 2.2** Potential energy diagram showing the relevant  $\text{H}_2$  electronic states in the  $2 + 1'$  REMPI study. Two-photon Doppler-free spectroscopy is applied on the  $F - X$  (0,11) band. Resonant excitation to the  $7p\pi$  state by the detection laser follows the spectroscopic excitation, leading to subsequent autoionization yielding enhanced  $\text{H}_2^+$  ion signal.

0.047 [59] and that of the presently used  $F - X(0, 11)$  band amounts to 0.17, making the latter band's transitions three times stronger.

### 2.2.1 Resonant ionization

The non-resonant ionization step was the major limitation in [32], since this prohibits the spectroscopy to be carried out at sufficiently low probe laser intensities. Due to ac-Stark effects, the lines were broadened to more than 1 GHz, while the expected instrumental linewidth is less than 200 MHz. Moreover, at higher probe intensities asymmetric line profiles are observed, reducing the accuracy of the line position determination and ultimately limiting the ac-Stark extrapolation to the unperturbed line position.

While signal improvement was observed when employing a detection laser in the range between 202-206 nm in Ref. [32], the enhancement was limited since no sharp resonances were found, indicating excitation to some continuum. For the present study, a thorough search for resonances from the  $F$  state was undertaken. The  $np\pi$  and  $np\sigma$  Rydberg series, with principal quantum number  $n = 5-7$  were identified as potential candidates based on the FCFs for the outer  $F$ -well. The search was based on reported FCFs for the  $D^1\Pi_u - F^1\Sigma_g^+$  ( $\nu', 1$ ) bands [59]. It was further assumed that the FCFs for the  $np\pi^1\Pi_u - F^1\Sigma_g^+$  electronic systems are comparable to that of  $3p\pi D^1\Pi_u - F^1\Sigma_g^+$ , since the potential energy curves for the  $np\pi^1\Pi_u$  Rydberg states are similar as they all converge to the  $\text{H}_2^+$  ionic potential. Note the particular characteristic of the  $n = 5-7$   $np^1\Pi_u$  Rydberg states, that dissociate to a ground state atom and another with a principal quantum number  $H(n-1)$ , i.e.  $5p\pi \rightarrow \text{H}(1s) + \text{H}(4f)$ ;  $6p\pi \rightarrow \text{H}(1s) + \text{H}(5f)$ ;  $7p\pi \rightarrow \text{H}(1s) + \text{H}(6d)$  [60–62]. The electron configuration changes as a function of the internuclear distance  $R$ , e.g. the low vibrational levels of the  $5p^1\Pi_u$  follow a diabatic potential that extrapolates to the  $n = 5$  limit, and not the  $n = 4$  dissociation limit at  $R \rightarrow \infty$ . This peculiarity is explained by  $l$ -uncoupling [63], as the molecule changes from Hund's case b (Born-Oppenheimer) to Hund's case d (complete nonadiabatic mixing) with increasing principal quantum number, corresponding to the independent nuclear motion of the residual ion core  $\text{H}_2^+$  and the excited Rydberg electron  $np$ . Such transition in Hund's cases occurs at  $n \sim 7$  for low rotational quantum numbers [61].

The  $np\pi^1\Pi_u$  Rydberg states decay via three competing channels: by fluorescence to lower  $n$  electronic configurations; by predissociation, where the

## Experiment

nascent H atom is further photoionized to yield  $H^+$  ions; and lastly, by autoionization to yield  $H_2^+$  ions. Recent analysis of one-photon absorption measurements using XUV synchrotron radiation in the range of 74–81 nm demonstrated that autoionization completely dominates over the other two competing channels in the case of  $n > 5$  [64]. Using the  $n = 5 - 7$  level energies of the Rydberg levels reported in [60–62], the detection laser was scanned in the vicinity of the expected transition energies, where it turned out that transitions to  $7p\pi, v = 5$  resulted in sufficient  $H_2^+$  signal enhancement. The maximum FCF overlap for the  $D^1\Pi_u - F^1\Sigma_g^+$  system is 0.34 for the (8,0) band, while the corresponding  $D - F$  (5,0) band only has an FCF of 0.022 [59]. Although the (8,0) band with better FCF could be used, the ionization step is already saturated using the weaker (5,0) band. Autoionization resonances are shown in Fig. 2.3 and assigned to  $R(3)$  and  $P(4)$  lines in the  $7p\pi^1\Pi_u - F^1\Sigma_g^+$  (5,0) bands, whose widths are in good agreement with the synchrotron data [60]. The neighboring resonances of the  $R(3)$  line in Fig. 2.3 are not yet assigned but is not relevant to the  $F - X$  investigation here. Appropriate  $7p\pi - F$  transitions are used for the ionization of particular  $F - X$  two-photon  $Q(J)$  transitions.

### 2.2.2 Frequency calibration

A representative high-resolution spectrum of the  $F^1\Sigma_g^+ - X^1\Sigma_g^+$  (0,11)  $Q(5)$  transition taken at low probe intensity is displayed in Fig. 2.4. Simultaneous with the  $H_2$  spectroscopy, the transmission fringes of the PDA cw-seed radiation through a Fabry-Pérot interferometer were also recorded to serve as relative frequency markers, with the free spectral range of  $FSR = 148.96(1)$  MHz. The etalon is temperature-stabilized and its length is actively locked to a frequency-stabilized HeNe laser. The absolute frequency calibration is obtained from the  $I_2$  hyperfine-resolved saturation spectra using part of the cw-seed radiation. For the  $Q(5)$  line in Fig. 2.4, the  $I_2 B - X(11, 2) P(94)$  transition is used, where the line position of the hyperfine feature marked with an \* is  $16482.83312(1) \text{ cm}^{-1}$  [65, 66]. The accuracy of the frequency calibration for the narrow  $H_2$  transitions is estimated to be 1 MHz in the fundamental or 4 MHz in the transition frequency, after accounting for a factor of 4 for the harmonic up-conversion and two-photon excitation.

For sufficiently strong transitions probed at the lowest laser intensities, linewidths as narrow as 150 MHz were obtained. This approaches the Fourier-

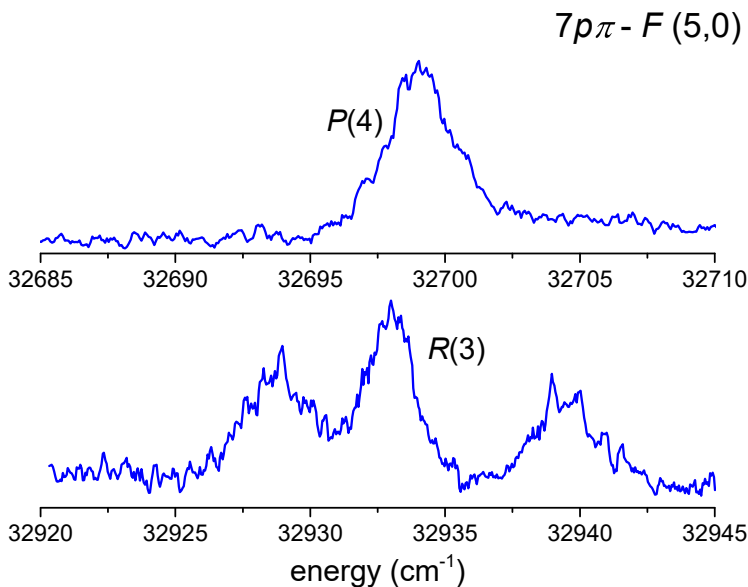


**Figure 2.3** Autoionizing  $R(3)$  and  $P(4)$  resonances of the  $7p\pi^1\Pi_u - F^1\Sigma_g^+(5,0)$  band which are crucial in enhancing the  $\text{H}_2^+$  signal strength of the  $F - X$  spectroscopy .

transform limited instrumental bandwidth of 110 MHz, for the 8-ns pulse widths at the fundamental, approximated to be Gaussian, that also includes a factor two to account for the frequency upconversion. The narrow linewidth obtained demonstrates that despite of the photodissociation process imparting considerable kinetic energy on the produced  $\text{H}_2^+$ , additional Doppler-broadening is not observed. Although not unexpected due to the Doppler-free experimental scheme implemented, this strengthens the claim that residual Doppler shifts are negligible.

Since the frequency calibration is performed using the cw-seed while the spectroscopy is performed using the PDA output pulses, any cw-pulse frequency offset need to be measured and corrected for [67]. A typical recording of the chirp-induced frequency offset for a fixed PDA wavelength is shown in Fig. 2.5. While the measurements can be done online for each pulse, this

## Experiment

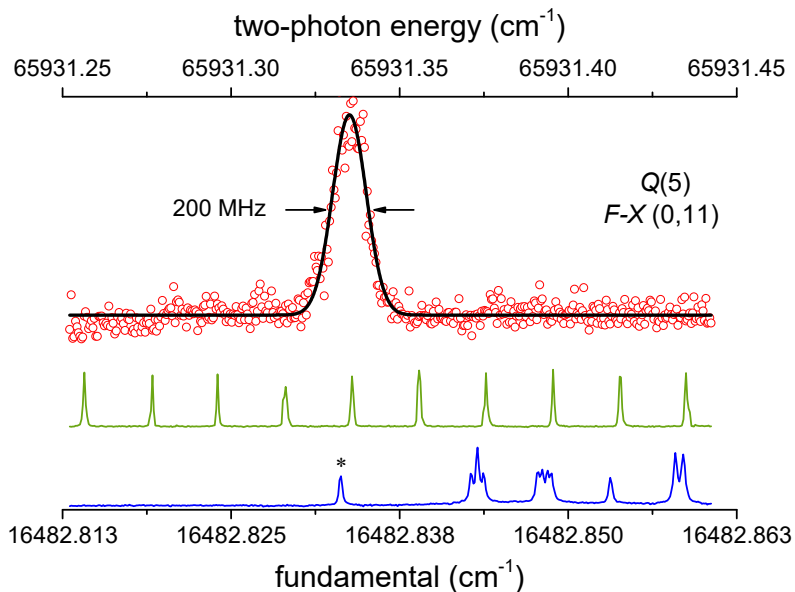


**Figure 2.4** Recording of the  $F^1\Sigma_g^+ - X^1\Sigma_g^+ (0,11) Q(5)$  transition is shown at a probe laser intensity of  $280 \text{ MW/cm}^2$  and detection in the  $\text{H}_2^+$  signal channel. The transmission markers of a length-stabilized Fabry-Pérot etalon ( $\text{FSR}=148.96 \text{ MHz}$ ) are used in the relative frequency calibration, while the hyperfine feature marked with \* of the  $\text{I}_2 B - X(11,2)P(94)$  transition serves as an absolute frequency reference (\* at  $16482.83312 \text{ cm}^{-1}$ ).

comes at the expense of a slower data acquisition speed, and was only implemented for a few recordings in order to assess any systematic effects. A flat profile of the cw-pulse offset when the wavelength was tuned over the measurement range accessed in this study justifies this offline correction. Typical cw-pulse frequency offset values were measured to be  $-8.7(1.2) \text{ MHz}$  in the fundamental, which translates to  $-35(5) \text{ MHz}$  in the transition frequency.

### 2.2.3 Uncertainty estimates

The sources of uncertainties and the respective contributions are shown in Table 2.1. The contributions of each source are summed in quadrature in order to obtain the final uncertainty for each transition. Data sets from which separate ac-Stark extrapolations to zero-power were performed on different days, and were verified to exhibit consistency within the statistical uncertainty of  $0.0014 \text{ cm}^{-1}$ . Note that the estimates shown in Table 2.1 are only for the low probe intensity measurements used to obtain the highest resolutions. The uncertainties of the present investigation constitute more than a factor of two improvement over our previous study in [32]. The dominant source of systematic uncertainty is the ac-Stark shift and is discussed in more detail in the following section.

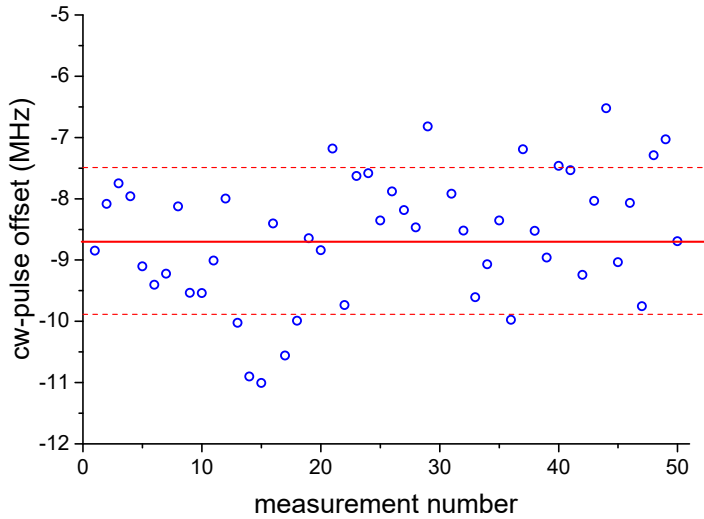


**Figure 2.5** Chirp-induced cw-pulse frequency offset of the fundamental radiation for a fixed PDA wavelength. The solid line indicates the average and the dashed lines indicate the standard deviation.

### 2.3 AC-Stark shift and broadening

In the perturbative regime, the leading-order energy level shift  $\Delta E_n$  of a state  $|n\rangle$  induced by a linearly-polarized optical field with an amplitude  $\mathcal{E}_0$ , and frequency  $\nu$  can be described as

$$\Delta E_n = \frac{1}{2} \sum_m \left\{ \frac{\langle n | \vec{\mu} \cdot \vec{\mathcal{E}}_0 | m \rangle \langle m | \vec{\mu} \cdot \vec{\mathcal{E}}_0 | n \rangle}{E_n - E_m - h\nu} + \frac{\langle n | \vec{\mu} \cdot \vec{\mathcal{E}}_0 | m \rangle \langle m | \vec{\mu} \cdot \vec{\mathcal{E}}_0 | n \rangle}{E_n - E_m + h\nu} \right\}, \quad (2.1)$$

where  $\langle n | \mu | m \rangle$  is the transition dipole moment matrix element between states  $n$  and  $m$ , with an energy  $E_m$  for the latter [68]. Thus  $\Delta E_n$  has a quadratic dependence on the field, or a linear dependence on intensity for this frequency-dependent ac-Stark level shift. In a simple case, when there is one near-resonant coupling to state  $m$  whose contribution dominates  $\Delta E_n$ , the sign of the detuning with respect to transition frequency  $\nu_{mn} = |E_n - E_m|/h$  determines the direction of the light shifts with intensity. When the probing radiation is blue-detuned, i.e.  $\nu > \nu_{mn}$ , the two levels  $|n\rangle$  and  $|m\rangle$  shift toward each other, while for red-detuning,  $\nu < \nu_{mn}$ , the levels repel each other. In the case when all accessible states are far off-resonant, both terms in Eq. (2.1) contribute for each state  $m$ , and numerous  $m$ -states need to be included in the calculations to explain the magnitude and sign of  $\Delta E_n$ . The energy shifts of the upper ( $\Delta E_u$ ) and lower ( $\Delta E_l$ ) levels in turn translate into an ac-Stark shift,

$$h\delta_S = \alpha I, \quad (2.2)$$

where  $\alpha$  is the ac-Stark coefficient. The measured *transition* energy is  $h\nu = h\nu_0 + \alpha I$ , where  $\nu_0 = |E_u - E_l|/h$  is the unperturbed (zero-field) transition frequency. The ac-Stark coefficient  $\alpha$  depends on the coupling strengths of the  $|u\rangle$  and  $|l\rangle$  levels to the dipole-accessible  $|m\rangle$  states, as well as the magnitude and sign of the detuning. We note that in a so-called *magic wavelength* configuration, the frequency  $\nu$  is selected so that the level shifts of the upper and lower states cancel out, leading to ac-Stark free transition frequencies [69].

The first experimental study of ac-Stark effects in molecules associated with REMPI processes was performed by Otis and Johnson on NO [70]. The broad ac-Stark-induced features in NO were later explained in the extensive

**Table 2.1** Uncertainty contributions in units of  $10^{-3} \text{ cm}^{-1}$ .

Source	Correction	Uncertainty
line-fitting	–	0.5
ac-Stark <sup>a</sup>	–	1.0
frequency calibration	–	0.3
cw-pulse offset	-1.2	0.2
residual Doppler	0	< 0.1
dc-Stark	0	< 0.1
total		1.5

<sup>a</sup> correction depends on transition

models by Huo *et al.* [71]. An investigation of ac-Stark effects on two-photon transitions in CO was performed by Girard *et al.* [72]. For molecular hydrogen, various studies have been performed on the two-photon excitation in the  $EF - X$  system over the years [24, 34, 73–75]. In the following, we present our evaluation of the ac-Stark effect in  $F - X$  (0,11) transitions where we first discuss line shape effects. This is followed by a discussion on the ac-Stark coefficients extracted from the analysis and comparisons with previous determinations on the  $EF - X$  system.

### 2.3.1 Line shape model

The line profiles of the  $F - X$  (0,11) Q(3) transition, recorded at different probe laser intensities, are displayed in Fig. 2.6. The ac-Stark broadening and asymmetry is readily apparent at higher intensities, and only at low intensities can the profile be fitted by a simple Gaussian line shape. Note that the shift in peak position at the highest probe intensity amounts to several linewidths of the lowest-intensity recording.

The asymmetry at high intensities is highly problematic with regards to the extraction of the line positions. In our previous study [32], a skewed Gaussian function  $g(f)$  was used to fit the spectra,

$$g(f) = \frac{A}{\Gamma_G} \exp\left(\frac{-(f - f_c)^2}{2\Gamma_G^2}\right) \times \left\{ 1 + \operatorname{erf}\left(\xi \frac{f - f_c}{\sqrt{2}\Gamma_G}\right) \right\}, \quad (2.3)$$

## AC-Stark shift and broadening

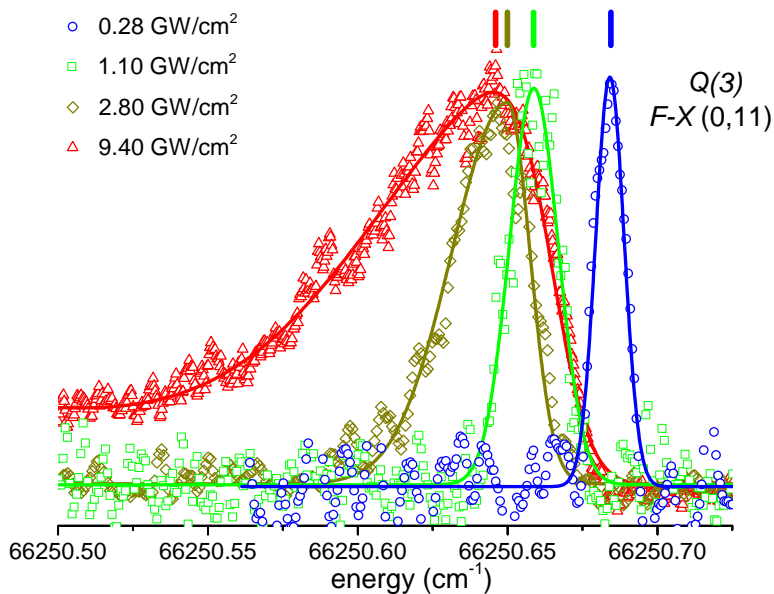


**Figure 2.6** Line profiles of the  $F-X(0,11)Q(3)$  transition recorded at different probe laser intensities. The vertical lines above each profile denote the peak position used in the subsequent extrapolation.

where  $f_c$  is the Gaussian peak position in the absence of asymmetry,  $\Gamma_G$  is the linewidth,  $A$  is an amplitude scaling parameter and  $\xi$  is the asymmetry parameter. The center  $f_c$  of the error function,  $\text{erf}(f)$ , is arbitrarily chosen to coincide with the Gaussian center. For sufficiently high intensities, a satisfactory fit is only possible if a linear background  $B(f)$  is added, and thus a revised fitting function,  $g'(f) = g(f) + B(f)$ , is used. This phenomenological fit function resulted in better fits than symmetric Lorentzian, Gaussian or Voigt profiles. However, since it does not include any consideration of the underlying physics, the interpretation of the extracted  $f_c$  and  $\xi$  parameters, as well as the background  $B(f)$ , is not straightforward. The energy position of the skewed profile maximum, instead of  $f_c$ , is used as the ac-Stark shifted frequency in the subsequent extrapolations.

## 2 Precision measurements and test of molecular theory in $\text{H}_2$ ( $\nu = 11$ )

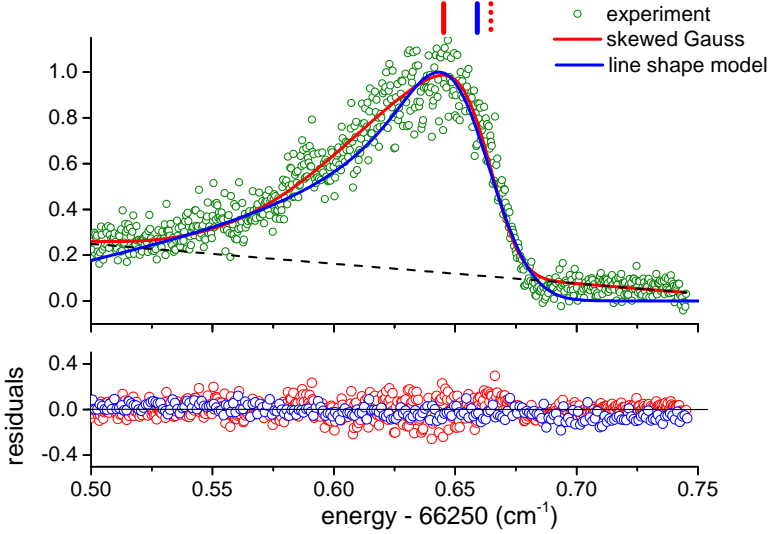


**Figure 2.7**  $F - X(0,11)Q(3)$  transition taken at high probe intensity ( $9.4 \text{ GW/cm}^2$ ) fitted with a skewed Gaussian (red solid line), with the fitted linear background indicated by the black dashed line. The fitted curve for line shape model is plotted as the blue solid line, which includes the effects of spatial and temporal intensity distribution. The red vertical line above the profile indicates the line position for the skewed Gaussian fit, while the blue vertical line indicates position shifted by  $\delta_0$  obtained from the line shape model. For comparison, the  $f_c$  parameter obtained from skewed Gaussian fitting is also indicated (dotted red line).

A more physically-motivated asymmetric line shape function was derived by Li *et al.* [76] for the analysis of multiphoton resonances in the  $\text{NO } A^2\Sigma^+ - X^2\Pi(0,0)$  band. Their closed-form line shape model accounted for effects of the spatial and temporal distributions of the light intensity. Here, we reproduce their line shape as a function of  $\delta_L = \nu - \nu_0$ , the laser frequency shift from the zero-field line position

$$S(\delta_0, \Gamma, \delta_L) = \kappa \int_0^{\delta_0} d\delta' \frac{K\left(\ln\left(\frac{\delta_0}{\delta'}\right)\right)}{\delta'} G(\Gamma, \delta' - \delta_L), \quad (2.4)$$

where  $\delta_0$  is the maximum ac-Stark shift induced at the peak intensity  $I_0$ .  $K$  contains the dependence on the temporal profile, as well as the transverse

AC-Stark shift and broadening

(Gaussian beam profile) and longitudinal intensity (focused) distribution, parametrized in [76] as

$$K(x) = \left[ 0.6366/x + 2.087e^{x/2} - e^{-x/2}(1.087 + 0.90x + 0.45x^2 + 0.3x^3) \right]^{-1}. \quad (2.5)$$

$G$  is a Gaussian distribution with full width at half maximum (FWHM)  $\Gamma$ ,

$$G(\Gamma, \delta' - \delta_L) = \frac{1}{\sqrt{\pi}} \frac{2\sqrt{\ln 2}}{\Gamma} \times \exp\left(-\left(\frac{2\sqrt{\ln 2}}{\Gamma}\right)^2 (\delta' - \delta_L)^2\right), \quad (2.6)$$

that accounts for other sources of line broadening, such as the spectral width of the laser or natural linewidth. The parameter  $\kappa = 1.189$  is a normalization factor which ensures that

$$\int_{-\infty}^{\infty} S(\delta_0, \Gamma, \delta_L) d\delta_L = 1 \quad (2.7)$$

for any  $\Gamma$  and  $\delta_0$ . It appears that the spatial and temporal intensity distribution were also treated in the investigations of Huo *et al.* [71] and Girard *et al.* [72], but the expressions were not explicitly given. When comparing different probe intensity recordings, the normalized profile given by Eq. (2.4), should be multiplied by a factor that scales with light intensity as  $\sim I_0^2$ , with the exact form given in Ref. [76]. Note that the error function in the skewed Gaussian model of Eq. (2.3) effectively captures the result of the integration in Eq. (2.4). However, the physical interpretation of the  $f_c$  and  $\xi$  parameters from the skewed Gaussian model is ambiguous, while the background,  $B(f)$ , is an *ad hoc* addition.

Li *et al.* [76] presented intuitive explanations of qualitative behavior of the line profile at two extreme cases: 1) of a perfectly collimated probe beam and 2) of a conically-focused beam. In case 1) the laser intensity is spatially homogeneous, so that the temporal intensity distribution is the dominant effect. Almost all contribution to the resonant excitation comes from the peak of the pulse, causing the line peak position to be shifted by almost  $\delta_0$ . In case 2) the strongly inhomogeneous spatial intensity plays the dominant role,

and molecules located at the focus, having the highest Stark shift  $\delta_0$ , have a smaller contribution relative to those from the entire interaction volume. The majority of the excited molecules come from a region of low intensities outside the focus, therefore the integrated line profile is only slightly shifted from the field-free resonance. Our experimental conditions lie in between these two cases, where a loose focus is implemented and a molecular beam, that overlaps to within a few Rayleigh ranges of the laser beam, is employed.

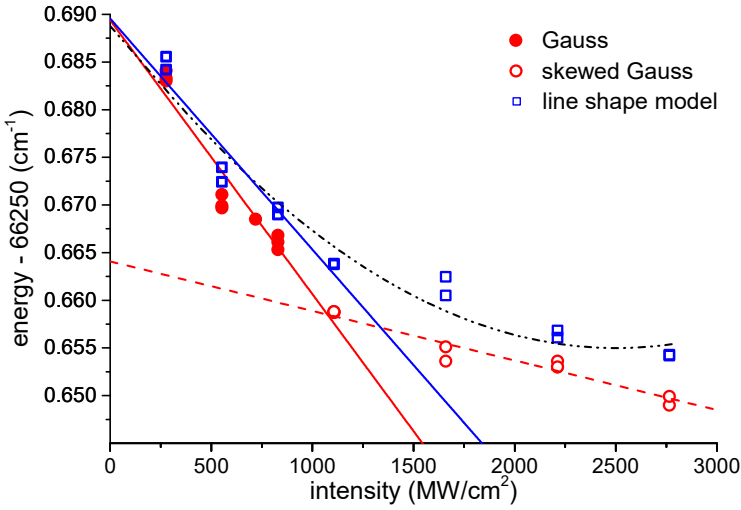


**Figure 2.8** Extracted line positions of the  $F - X(0,11)Q(3)$  transition from measurements at different probe laser intensities. Squares (blue) are obtained from fits using the line shape model of Eq. (2.4), while circles (red) are obtained from Gaussian fits. The solid circles (red) are symmetric profiles fitted with a simple Gaussian, while unfilled circles are fitted with skewed Gaussian profiles. The solid lines are linear fits to low-intensity data points, while the dashed lines is a linear fit using the high-intensity points only. The dash-dotted line is a second-order polynomial fit for the whole intensity range using the data points obtained from the line shape model (squares).

Using the line shape model expressed in Eq. (2.4) and appropriate experimental parameters, the asymmetric line profiles can be well fitted. For a recording at a particular intensity  $I_0$ , the maximum ac-Stark shift from the zero-field resonance,  $\delta_0$ , is obtained from the fit. The line shape asymme-

try, in particular the skew handedness, is consistent with the direction of the light shift observed at different intensities, validating the expected behavior from Eq. (2.4). In Fig. 2.7, fits using the physical line shape model and skewed Gaussian profile are shown for the  $Q(3)$  transition recorded at  $\sim 9.4 \text{ GW/cm}^2$ . The linear background  $B(f)$  (dashed line) was necessary for a satisfactory fit with the skewed Gaussian, while no additional background functions were used for the line shape model. The extracted line positions are indicated in Fig. 2.7 by vertical lines above the profiles, where the difference in the line positions of the two fit functions amounts to about  $0.006 \text{ cm}^{-1}$ . For reference, the  $f_c$  position obtained by using Eq. (2.3) is also indicated by a dotted line, although this is not used further in the analysis.

A comparison of the  $F - X(0,11) Q(3)$  line positions extracted from the skewed Gaussian and from the line shape model based on Li *et al.* [76] is shown in Fig. 2.8. The line positions show different trends that separate into low-intensity, with symmetric line profiles, and high-intensity subsets, with asymmetric ones. The line profile models are in agreement at low intensities as expected, but show a discrepancy at higher intensities as explained above (see Fig. 2.7). The extrapolated zero-intensity positions for the low-intensity measurements converge to within  $0.0001 \text{ cm}^{-1}$  for both line profile models.

When using only the high-intensity data to extrapolate the zero-intensity frequency, a shift of  $\sim 0.02 \text{ cm}^{-1}$  with respect to the low-intensity subset is found. The latter difference is a concern when only high-intensity data is available as in Ref. [32] for the  $F - X(3,12)$  band. The ac-Stark coefficients, however, are an order of magnitude lower for the  $F - X(3,12)$  band compared the present  $(0,11)$  band, thus any systematic offset is still expected to be within the uncertainty estimates in that study [32]. It is comforting to note that a second-order polynomial fit, also shown in Fig. 2.8 as dash-dotted curve, results in an extrapolated zero-field frequency that is within  $0.0002 \text{ cm}^{-1}$  of the low-intensity linear fits.

The ac-Stark shifts of the different  $F - X(0,11)$  transitions exhibit a nonlinear dependence on intensity, contrary to the expected behavior in Eq. (2.2). A correlation is also observed between the nonlinearity and the ac-Stark coefficient  $\alpha$ , where the onset of nonlinearity occurs at a higher intensity for transitions with smaller  $\alpha$ . The nonlinearity may indicate close proximity to a near-resonant state, which may signal the breakdown of the perturbative approximation in Eq. (2.1). Possibly, this requires contributions beyond the second-order correction [72] that lead to a higher-power dependence on

intensity. A similar behavior was observed by Liao and Bjorkholm in their study of the ac-Stark effect in two-photon excitation of sodium[77]. In that investigation, they observed the nonlinear dependence of the ac-Stark shift at some probe detuning that is sufficiently close to resonance with an intermediate state.

### 2.3.2 AC-Stark coefficients

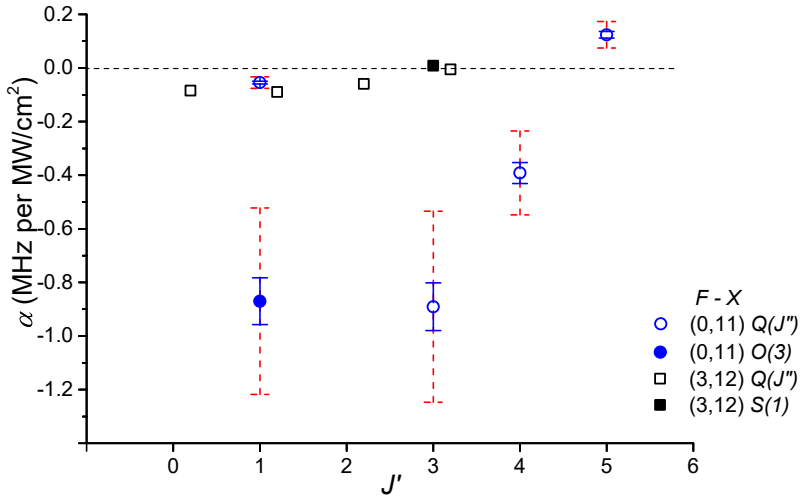


**Figure 2.9** ac-Stark coefficients plotted against the upper  $J'$ -quantum number for the different transitions of the  $F - X$  (0,11) band (blue circles). The  $\alpha$ -values of the  $F - X$  (3,12) transitions (black squares) from Ref. [67] are also plotted and displaced for clarity. The datapoint indicated by a filled circle is obtained from the  $F - X$  (0,11)  $O(3)$  transition, while the filled rectangle is from the  $F - X$  (3,12)  $S(1)$  transition.

The ac-Stark coefficient  $\alpha$ , as defined in Eq. (2.2), was obtained by Hanne-  
mann *et al.* for the  $\text{H}_2$   $EF^1\Sigma_g^+ - X^1\Sigma_g^+$  (0,0) band, where they reported +13(7)  
and +6(4) MHz per MW/cm<sup>2</sup>, respectively, for the  $Q(0)$  and  $Q(1)$  lines [34].  
Investigations on the  $E - X$  (0,1) band in Ref. [24], and more extensively in  
Ref. [78], also resulted in positive ac-Stark coefficients for  $Q(J = 0 - 3)$  tran-  
sitions that are about an order of magnitude lower than for the  $E - X$  (0,0)

band. Eyler and coworkers [75] found that the ac-Stark slopes vary considerably, typically at a few tens of MHz per ( $\text{MW}/\text{cm}^2$ ), for different transitions in the  $\text{H}_2 E - X$  system. The Rhodes group in Chicago has performed a number of excitation studies with high-power lasers on the  $EF - X$  system in hydrogen, where they also investigated optical Stark shifts (e.g. [73]). Following excitation of molecular hydrogen by 193 nm radiation, intense stimulated emission on both the Lyman and Werner bands is observed. Using excitations intensities of  $\sim 600 \text{ GW}/\text{cm}^2$ , they obtained shifts in the order of 2 MHz per  $\text{MW}/\text{cm}^2$  for the  $EF - X (2,0)$  band. While the work of Vrakking *et al.* [74] was primarily on the detection sensitivity of REMPI on  $\text{H}_2 EF - X$  system, they also obtained ac-Stark coefficients of  $\sim 15 \text{ MHz per MW}/\text{cm}^2$  similar to the value found in Ref. [34]. Vrakking *et al.* [74] also made reference to a private communication with Hessler on the ac-Stark effect (shift) amounting to 3-6 MHz per  $\text{MW}/\text{cm}^2$ , presumably obtained in the study by Glab and Hessler [79].

The ac-Stark coefficients  $\alpha$  obtained in this study for the  $F - X (0,11)$  transitions are plotted in Fig. 2.9. The error bars in the figure comprise two contributions, with the larger one dominated by the accuracy in the absolute determination of the probe intensity. The difficulties include estimating the effective laser beam cross-sections in interaction volume, that should take into account the overlap of the counterpropagating probe beams and also the overlap of the photodissociation and ionization beams. The smaller of the error bars are obtained from fits using relative intensities, shown here to emphasize that the differences in  $\alpha$ -coefficients are significant. Also included in Fig. 2.9 are the Stark coefficients for  $F - X (3,12)$  obtained in [67], that differ by about an order-of-magnitude with respect to the values obtained for  $F - X (0,11)$ . The sign of the  $F - X$   $\alpha$ -coefficients are mostly negative for both bands except for the  $F - X (0,11) Q(5)$  line.

The different signs in the ac-Stark coefficients, which are positive for the  $E - X$  transitions and mostly negative for the  $F - X$  transitions, seem to be a feature of the ac-Stark effect in  $\text{H}_2$ . For the  $E - X (0,0)$  transitions probed at around 202 nm and  $E - X (0,1)$  transitions probed at around 210 nm, all intermediates states are far off-resonant with respect to transitions from the  $E$  or  $X$  levels. Using Eq. (2.1), the ac-Stark shift is estimated based on the approximation of Rhodes and coworkers [80, 81] for the  $E - X (2,0)$  band. In those studies, they assumed that the intermediate states are predominantly the Rydberg series at principal quantum number  $n > 2$ , clustered at an av-

erage energy of  $E_m = 14.7$  eV. The present estimates of ac-Stark shifts via Eq. (2.1), using the probe frequency and intensity in Ref. [34], are in agreement to within an order of magnitude of the  $E - X$  (0,0) observations. A similar estimate for  $E - X$  (0,1) transitions are also within an order-of-magnitude agreement of the measurements in [24, 78]. The blue-detuned probe in the aforementioned  $E - X$  transitions explains the observed light shift direction as expected from Eq. (2.1).

**Table 2.2** Measured two-photon transition energies of  $F - X$  (0,11) band. All values in  $\text{cm}^{-1}$ .

Line	Experiment
Q(1)	66 438.2920 (15)
Q(3)	66 250.6874 (15)
Q(4)	66 105.8695 (15)
Q(5)	65 931.3315 (15)
O(3)	66 189.5591 (15)

In  $F - X$  excitation from  $X$ ,  $v = 11$  and  $v = 12$ , the fundamental probe wavelengths are around 300 nm. Rydberg  $np$  levels can be close to resonance at the probe wavelengths, a fact that we have exploited in the resonant ionization (using an additional laser source) for the REMPI detection. This could explain the difference in sign of  $\alpha$  between the  $E - X$  and  $F - X$  transitions. Furthermore, Fig. 2.9 displays a trend the  $F - X$  (0,11) transitions, where a small negative coefficient is observed for Q(1), increasing in magnitude at Q(3), decreasing in magnitude again and eventually becoming positive at Q(5). Interestingly, the  $F - X$  (0,11) O(3) transition displays a relatively large  $\alpha$  with respect to that of the Q(1) transition, despite having the same upper  $F$  level  $J' = 1$ . The Q(1) and O(3) fundamental probe energies differ only by some  $250 \text{ cm}^{-1}$ , but this results in significant change in  $\alpha$ . These phenomena hint towards a scenario where some near-resonant levels are accessed, so that the summation (and cancellation) of the contributions in Eq. (2.1) depend more sensitively on the detunings of the probe laser frequency with respect to  $\nu_{mm}$ . The variation in  $\alpha$ -magnitudes as well as the change from negative to positive sign could be explained by a change from red- to blue-detuning when traversing across a dominant near-resonance intermediate level. The latter behavior was expected in the NO investigation of Huo *et al.*, where the  $\alpha$ -coefficients for individual  $M$  sublevels varied from -4.1 to 53 MHz per

MW/cm<sup>2</sup> [71]. The order of magnitude difference between  $\alpha$ -values of the  $F-X$  (0,11) and (3,12) transitions may be due to less-favorable FCF overlaps of the near-resonant intermediate levels for the latter band. This is correlated with the similar value of the  $F-X$  (3,12)  $Q(3)$  and  $S(1)$  transition, displaying a different trend to that of the  $Q(1)$  and  $O(3)$   $\alpha$ -coefficients in the  $F-X$  (0,11) band. The nonlinear intensity-dependence of the transitions discussed in the previous subsection, may be consistently explained by the same argument on the importance of near-resonant intermediate levels. For a quantitative explanation of the  $F-X$  ac-Stark shift, a more extensive theoretical study is necessary to account for the dense intermediate Rydberg levels involved that should also include considerations of FCF overlaps and dipole coupling strengths at the appropriate internuclear distance.

## 2.4 Results and discussion

The resulting two-photon transition energies for the  $F^1\Sigma_g^+ - X^1\Sigma_g^+$  (0,11) lines are listed in Table 2.2. The results presented are principally based on high-resolution measurements using transitions with symmetric linewidths narrower than 1 GHz. This ensures that the ac-Stark shift extrapolation can be considered robust and reliable as discussed above.

Combination differences between appropriate transition pairs allow for the confirmation of transition assignments as well as consistency checks of the measurements, where most systematic uncertainty contributions cancel. The  $Q(1)$  and  $O(3)$  transitions share a common upper  $EF$  level, and the energy difference of 248.7329(21) cm<sup>-1</sup> gives the ground state splitting  $X, v'' = 11, J'' = 1 \rightarrow 3$ . This can be compared to the theoretical splitting derived from Komasa *et al.* [10] of 248.731(7) cm<sup>-1</sup>. In analogous fashion, the  $Q(3)$  and  $O(3)$  share the same lower  $X$  level, which enables the extraction of the  $EF, v' = 1, J' = 1 \rightarrow 3$  energy splitting of 61.1194(21) cm<sup>-1</sup>. This is in good agreement to the derived experimental splitting of 61.1191(10) cm<sup>-1</sup> from Bailly *et al.* [82].

To extract the ground electronic  $X^1\Sigma_g^+, v = 11, J$  level energies, from the  $EF-X$  transition energy measurements, we use the level energy values of the  $F(v' = 0)$  states determined by Bailly *et al.* [82]. The derived experimental level energies are listed in Table 2.3, where the uncertainty is limited by the present  $F-X$  determination except for the  $J = 4$ . The calculated values obtained by Komasa *et al.* [10] are also listed in Table 2.3. The experimental

**Table 2.3** Experimental and theoretical level energies of the  $X^1\Sigma_g^+, v = 11, J$  levels.

$J$	Experiment	Theory	Exp–Theo
1	32 937.7554(16)	32 937.7494(53)	0.0060(55)
3	33 186.4791(16)	33 186.4802(52)	-0.0011(54)
4	33 380.1025(33)	33 380.1015(52)	0.0006(62)
5	33 615.5371(18)	33 615.5293(51)	0.0078(54)

and theoretical values are in good agreement, except for  $J = 5$  that deviate by  $1.5\text{-}\sigma$ . The combined uncertainty of the difference is dominated by the theoretical uncertainty. However, improvements in the calculations of the nonrelativistic energies, limited by the accuracy of fundamental constants  $m_p/m_e$  and  $R_\infty$ , have recently been reported [4], and improved calculations of QED corrections up to the  $m\alpha^6$ -order is anticipated.

As has been pointed out previously in Ref. [32], the uncertainties in the calculations [10] are five times worse for the  $v = 8 - 11$  in comparison to the  $v = 0$  level energies. Along with the previous measurements on the  $X, v = 12$  levels in Ref. [32], the measurements presented here probe the highest-uncertainty region of the most advanced first-principle quantum chemical calculations.

## 2.5 Conclusion

$\text{H}_2$  transition energies of  $F^1\Sigma_g^+(v' = 0) - X^1\Sigma_g^+(v'' = 11)$  rovibrational states were determined at  $0.0015 \text{ cm}^{-1}$  absolute accuracies. Enhanced detection efficiency was achieved by resonant excitation to autoionizing  $7p\pi$  electronic Rydberg states, permitting excitation with low probe laser intensity that led to much narrower transitions due to reduced ac-Stark effects. The asymmetric line broadening, induced by the ac-Stark effect, at high probe intensities was found to be well-explained by taking into account the spatial and temporal intensity beam profile of the probe laser. The extracted ac-Stark coefficients for the different transitions  $F - X$ , as well as previously determined  $E - X$  transitions, are consistent with qualitative expectations. However, a quantitative explanation awaits detailed calculations of the ac-Stark effect that account for molecular structure, i.e. including a proper treatment of relevant intermediate states.

## Conclusion

Using the  $F$  level energies obtained by Bailly *et al.* [82], the level energies of  $X(v = 11, J = 1, 3 - 5)$  states are derived with accuracies better than  $0.002 \text{ cm}^{-1}$  except for  $J = 3$ , limited by  $F$  level energy accuracy. The derived experimental values are in excellent agreement with, thereby confirming, the results obtained from the most advanced and accurate molecular theory calculations. The experimental binding energies reported here are about thrice more accurate than the present theoretical values, and may provide further stimulus towards advancements in the already impressive state-of-the-art *ab initio* calculations.

This work is part of the research programme of the Foundation for Fundamental Research on Matter (FOM), which is part of the Netherlands Organisation for Scientific Research (NWO). P. W. received support from LASERLAB-EUROPE within the EC's Seventh Framework Programme (Grant No. 284464). W. U. received funding from the European Research Council (ERC) under the European Union's Horizon 2020 research and innovation program (Grant No. 670168).



---

## Precision spectroscopy of the $EF^1\Sigma_g^+ - X^1\Sigma_g^+$ system in $H_2$ at large internuclear separation: A combined study of photofragment imaging and autoionization towards labeling and detection

### Abstract

The rovibrational quantum levels of  $H_2$  with the wavefunction density at large internuclear separation,  $R \sim 4$  a.u., are subjected to Doppler-free two-photon laser spectroscopic measurements to determine their level energies to high accuracy. Such experiments verify the binding energies obtained from full *ab initio* calculations including quantum electrodynamical and relativistic contributions for this benchmark molecule. The two-photon excitation from  $X^1\Sigma_g^+(v^*, J)$  proceeds through the  $F^1\Sigma_g^+$  outer-well levels, which is further promoted to the auto-ionization continuum by step-wise laser excitation. The labeling of the vibrational quantum states, produced via photodissociation of  $H_2S$  molecules, is investigated with velocity map imaging of  $H_2^*(v)$  photofragments. Assignment of the precision measurements on  $EF - X$  transitions based on the *ab initio* knowledge of the  $X$  state [Komasa *et al.*, JCTP, 7, 3105-3115 (2011)] and the experimentally determined level structure of the  $EF$  state [Bailly *et al.*, Mol. Phys. 108, 827-846 (2010)] has a limited scope. In this study, the transitions involving higher rotational states ( $J = 4 - 7$ ) in the outer-well state  $F^1\Sigma_g^+(v = 0)$  are assigned using information from the

### 3 Precision spectroscopy of the $EF^1\Sigma_g^+ - X^1\Sigma_g^+$ system in $H_2$ at large $R$

autoionizing excitation in the measurement scheme. The autoionization spectrum obtained via laser excitation from the  $F^1\Sigma_g^+$  levels, bound at large internuclear separation ( $R \sim 4 - 5$  a.u.), to resonances in the ionization continuum in the energy range  $131,100 - 133,000$   $\text{cm}^{-1}$ . The energy range as well as the large internuclear separation present a challenge for multi-channel quantum defect theory (MQDT), and in particular, for inclusion of the doubly-excited electronic states within its framework. The present study delivers precise values for binding energies of  $X^1\Sigma_g^+(v = 11, J = 6, 7)$  levels. A tentative assignment has been made for the  $F - X(2, 14)$  band transitions involving the highest vibrational state,  $X(v = 14)$  of the  $H_2$  molecule.

### 3.1 Introduction

Precision spectroscopy on highly excited vibrational states in the  $X^1\Sigma_g^+$  electronic ground state of the hydrogen molecule is achieved through the preparation of these states via two-photon ultraviolet photolysis of hydrogen sulfide ( $\text{H}_2\text{S}$ ) molecules. This pathway was first demonstrated in the one-colour laser studies by Steadman and Baer [33]. In subsequent investigations, exploring this pathway in a more refined manner using three independently tunable lasers, it was found that the  $\text{H}_2(v^*)$  states prepared through photolysis could be further excited to  $F^1\Sigma_g^+$  outer-well states (see fig. 3.1) and subsequently be ionized in a controlled manner. In such a scheme accurate values of the binding energy of  $\text{H}_2$ ,  $X(v = 11, 12)$  levels for various  $J$  could be determined [32, 35]. In these spectroscopic studies, it was established that the excitation from  $\text{H}_2(v^*)$  only proceeds through  $F^1\Sigma_g^+$  outer well states, and that excitation via the  $E^1\Sigma_g^+$  inner-well does not occur. Hence it is only the wave function density at rather large internuclear separation ( $R \sim 4 - 5$  a.u.) that is probed in such a three-step excitation scheme.

The identification of  $F^1\Sigma_g^+ - X^1\Sigma_g^+$  two-photon transitions is based on the known energy separations between the  $F$  and  $X$  levels. Accurate knowledge of the  $X^1\Sigma_g^+(v, J)$  levels is obtained from the advanced *ab initio* calculations including phenomenon of quantum electrodynamics (QED) as well as relativistic corrections [8, 10, 83, 84], that were tested in a number of laser precision studies [23, 24, 34, 75]. The most accurate knowledge of the  $F^1\Sigma_g^+(v, J)$  level structure stems from the combination of laser-based spectroscopic studies [85, 86] and Fourier-transform emission studies [82]. The information on the quantum levels in the  $F$  outer-well is however limited and is particularly lacking for the higher rotational quantum numbers ( $J > 4$ ) of the  $F(v = 0)$  state. Strong perturbations at high  $J$  states between outer ( $F$ ) and inner ( $E$ ) well levels prohibiting the use of a straightforward extrapolation of rotational progressions [86]. As a consequence the dense line spectra of the  $F-X$  system are not easily assigned. The usual spectroscopic labeling approach based on the measurement of combination differences remains effective, and has been used in this investigations.

In the present study the three-step excitation scheme, already used previously in [35], is explored in further detail. The information from the preparatory photolysis step and that of the final resonant ionization step is extracted in an attempt to assist in the labeling of quantum states probed in the two-



## Experimental setup

photon studies [89, 90], and recently using synchrotron sources [60–62, 91]. Results from these studies are, in general, interpreted in the framework of multi-channel quantum defect theory (MQDT) that was first applied to  $\text{H}_2$  in the pioneering study by Herzberg and Jungen [63]. However, these studies were limited to rotational quantum numbers  $J \leq 4$  and small internuclear separations of  $R \sim 2$  a.u. Franck-Condon (FC) overlap from the ground state is significant only up to the first few vibrational states of the  $n\pi^1\Pi$  or  $n\pi\sigma^1\Sigma^+$  Rydberg manifolds converging to  $v^+ \leq 3$  ionic states. Ionization of the  $F^1\Sigma_g^+$  outer well states involves excitation from larger internuclear separation  $R \sim 4 - 5$  a.u. It requires excitation to the energy range above  $130\,000\text{ cm}^{-1}$  in the energy level scheme of the  $\text{H}_2$  molecule in fig. 3.1. The combination of incorporating high  $J$  states, large internuclear separation, and the high energy range would require extensions to the MQDT methods explored so far in the  $\text{H}_2$  molecule.

In this chapter, section 3.2 describes the experimental setup. Section 3.3 focusses on the high precision 2+1 REMPI studies on  $F-X$  transitions involving the resonant detection method based on the knowledge of autoionization resonances. An exact assignment procedure for the transitions involving  $J > 5$  levels in the  $F-X(0, 11)$  band, and a tentative one for the  $F-X(2, 14)$  band transitions from the  $X(v = 14)$  state are explained based on the two-photon Doppler-free measurements. The photofragment imaging studies on  $\text{H}_2\text{S}$  molecule and the identification of the vibrational quantum state of  $\text{H}_2^*(v)$  using the velocity map imaging (VMI) technique are presented in section 3.4. Finally section 3.5 attempts to understand the Rydberg level structure of  $\text{H}_2$  from its first singlet outer-well state by recording the autoionization spectra.

### 3.2 Experimental setup

The schematic of our experimental set up is as shown in fig. 3.2. In the initial step, we produce vibrationally hot hydrogen molecules  $\text{H}_2^*(v = 10 - 14)$  with a nonequilibrium distribution of population via two-photon photodissociation of  $\text{H}_2\text{S}$  molecule at 285-297 nm [33]. The dissociation laser (PDL I) produces frequency-doubled UV pulses at 291.5 nm with 4mJ energy, that are focussed using a 30 cm lens onto a skimmed  $\text{H}_2\text{S}$  molecular beam. In the second step, we prepare  $F(v = 0, J)$  using a two-photon resonant excitation scheme from a highly excited vibrational state, i.e.  $X(v = 11)$ . The  $F-X(0, 11)$  band exhibits a favorable FC factor of 0.17 [58]. A narrowband pulsed ( $\sim 30$  MHz)

### 3 Precision spectroscopy of the $EF^1\Sigma_g^+ - X^1\Sigma_g^+$ system in $H_2$ at large $R$

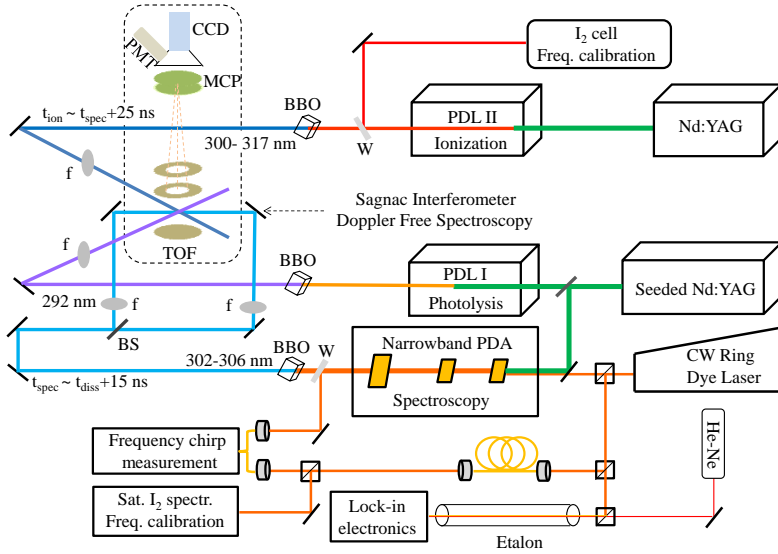


**Figure 3.2** Experimental set up. PDL I provides 292 nm pulses required for photodissociation of  $H_2S$  molecules. The nascent  $H_2^*(v)$  photoproducts are subjected to the  $F-X$  two-photon Doppler-free spectroscopy, using 302–306 nm pulses generated by an injection-seeded narrowband PDA laser. A third laser, PDL II (300–317 nm) is employed for studying the autoionization resonances from the  $F$  outer-well. Ions are extracted by the electrostatic lens and detected at the end of the TOF tube that is integrated with the velocity map imaging on a CCD detector (see the text for details about the frequency calibration elements).

dye amplifier (PDA) generates a frequency-doubled output at 300–308 nm, and pulses with 500  $\mu J$  energy are focussed with a 50 cm lens to excite the  $F-X$  (0, 11) band. A two-photon counter-propagating Sagnac interferometric alignment geometry [57] is employed during the two-photon spectroscopy as shown in figure 3.2. This circumvents the large Doppler-broadening resulting from a kinetically hot distribution of  $H_2^*$  molecules. Moreover, the signal strength is enhanced in the Doppler-free excitation with counter-propagating laser beams. An optical delay line of 15 ns is introduced between photodissociation and spectroscopy lasers for high precision measurements to avoid ac-Stark broadening. The frequency of the PDA is calibrated using the trans-

mission markers of a length stabilized etalon with respect to the hyperfine spectral components of the  $B - X$  system of  $I_2$  recorded through saturation spectroscopy.

A third laser (PDL II) delivering frequency-doubled pulses at 300 – 317 nm interacts with the molecules excited to the outer-well states  $F(v = 0, J)$ , to produce ion signal and to record autoionization structure in the energy range of 131,100 – 133,000  $\text{cm}^{-1}$ . The frequency of the PDL II is calibrated using the Doppler broadened lines through an  $I_2$  absorption cell kept at room temperature. The ionization laser is electronically delayed by 25 ns with respect to the spectroscopy laser and 1 mJ ionization pulse energy focused on the excitation volume using a 50 cm lens as shown in figure 3.2, again to avoid ac-Stark broadening of  $F - X$  transitions. Resonant ionization detection is achieved by extracting  $H_2^+$  ions using time-of-flight (TOF) plates, which are triggered 50 ns after the ionization laser. Finally, ions are detected by the microchannel plate (MCP) with phosphor placed at the end of the 40 cm long TOF tube and imaged by CCD camera for the VMI studies. The integrated ion signal is recorded by a PMT for the spectroscopy.

### 3.3 Doppler-free precision spectroscopy on $F - X$ transitions

This section discusses the methods for two-photon Doppler-free precision spectroscopy on  $F - X$  transitions and the importance of finding autoionization pathways to generate a sufficient signal strength, even when using limited laser intensities in the spectroscopy step. The difference between non-resonant [32] and resonant excitation is discussed. The latter method was employed previously for a measurement of  $Q(1)$ ,  $Q(3)$ ,  $Q(4)$  and  $Q(5)$  lines of the  $F - X(0, 11)$  band [35] (discussed in Chapter 2), and will be extended here to determine precision values for  $Q(6)$  and  $Q(7)$ . It is also discussed how the autoionization resonances can be employed for the assignment of transitions in the  $F - X$  electronic system. A provisional assignment has been made for  $F - X(2, 14)$  band transitions based on narrowband spectroscopic investigations.

#### 3.3.1 Resonant detection and improved ac-Stark analysis

In the case of a previous study on  $X(v = 12)$  state, the experimental uncertainty was limited by line broadening due to the ac-Stark effect [32]. This

### 3 Precision spectroscopy of the $EF^1\Sigma_g^+ - X^1\Sigma_g^+$ system in $H_2$ at large $R$

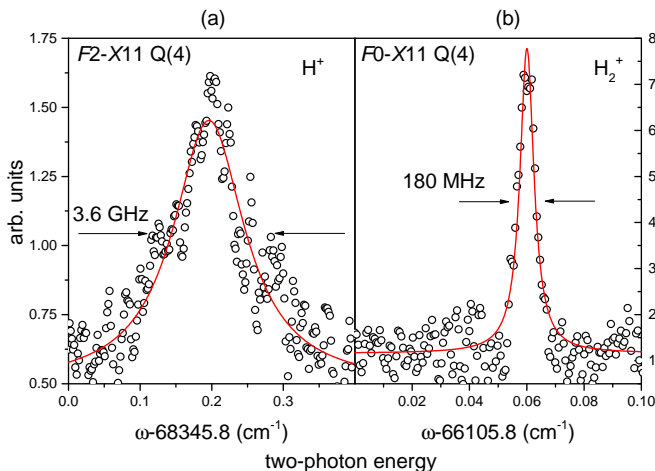
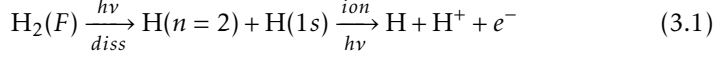
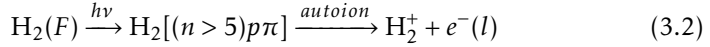


**Figure 3.3** Comparison between (a) nonresonant and (b) resonant ionization detection scheme for high precision REMPI studies on  $F - X$  two-photon transitions, using  $H^+$  and  $H_2^+$  signals respectively (see text for details).

can be attributed to two causes. One, the vibrationally excited states  $H_2^+(v, J)$  produced via photochemical routes are poorly populated. Two, the Frank-Condon overlap between the ion and molecular state wavefunctions from the outer-well, i.e.,  $H_2^+(X^+) - H_2(F)$  is negligible, i.e.  $\ll 0.001$  for the transitions up to  $v^+ = 3$  [92]. For these reasons, it turned out to be necessary to probe  $F - X$  transitions at intensities well above  $\text{GW}/\text{cm}^2$  leading to asymmetric ac-Stark broadening. This shortcoming was overcome while measuring the  $X(v = 11)$  level with the implementation of a resonant ionization detection scheme to observe symmetric and narrower line profiles which are limited by instrumental bandwidth [35]. These autoionization resonances were shown to be crucial to limit the ac-Stark broadening by reducing the probe intensities of the spectroscopic step by a factor of 20. Figure 3.3. shows a typical comparison between Doppler-free two-photon spectra of  $F - X$  transitions using non-resonant and resonant ionization detection schemes. In both cases the  $X(v = 11, J = 4)$  level is probed but the excitation proceeds through different vibrational levels,  $v = 0$  and  $2$ , of the intermediate  $F$  state. A typical chemical pathway for the non-resonant scheme is:



Here the population of the  $F$  outer well state is further promoted to a dissociative continuum of the  $\text{H}_2$  molecule, producing a  $\text{H}(n=2)$  fragment. The UV radiation present in the interaction region then readily ionizes this  $\text{H}(n=2)$  product into  $\text{H}^+$  ions. Both steps proceed non-resonantly. The resonant pathway proceeds via:



Despite a small difference in FC overlap ( $\sim 2\times$ ) [59] between the two bands in fig. 3.3, a significant reduction ( $\geq 20\times$ ) in the ac-Stark broadening is achieved by employing the resonant detection method. The non-resonant pathway (Eq. 3.1) requires a threshold probe intensity of  $9 \text{ GW/cm}^2$  whereas in the resonant pathway (Eq. 3.2) it requires only  $450 \text{ MW/cm}^2$  to achieve a three times better signal-to-noise ratio. The ac-Stark broadening is reduced by an order of magnitude for all transitions in the  $F - X(0,11)$  band and thus allows for a more rigorous ac-Stark analysis including spatial and temporal intensity effects [35].

### 3.3.2 Assignment of the transitions in $F - X(0,11)$ band

Excited state level energies, taken from Bailly *et al.* [82], serve as a reference for  $EF - X$  spectroscopy with uncertainties better than  $0.001 \text{ cm}^{-1}$  for both inner and outer wells. Especially for  $F(v=0)$  knowledge of the level energies is limited to  $J \leq 5$ . During our extensive survey scans in search of two-photon transitions arising from  $X(v=12-14)$  we have considered the possibility of excitations to the higher angular momentum states  $F0(J=6,7)$  starting from  $X(v=11)$ . For the unambiguous identification of transitions involving  $F0(J \geq 5)$  levels we have adapted the combination difference procedure at each stage of the multi-step spectroscopic scheme that is shown in figure 3.1.

We started with probing the  $O$ -branch transitions,  $O(6)$  and  $O(7)$ , using the *ab initio* level energies for the ground state  $X11(J=6,7)$  taken from Komasa *et al.* [10]. Subsequently, these  $O$ - transitions to  $F0(J=4,5)$  states are resonantly ionized with the help of the known autoionization resonances, which were verified in the earlier studies as shown in fig. 3.4 (a) [35, 60]. The  $F - X$  two-photon transition pairs in excitation stage  $Q(4), O(6)$  and  $Q(5), O(7)$

### 3 Precision spectroscopy of the $EF^1\Sigma_g^+ - X^1\Sigma_g^+$ system in $H_2$ at large $R$

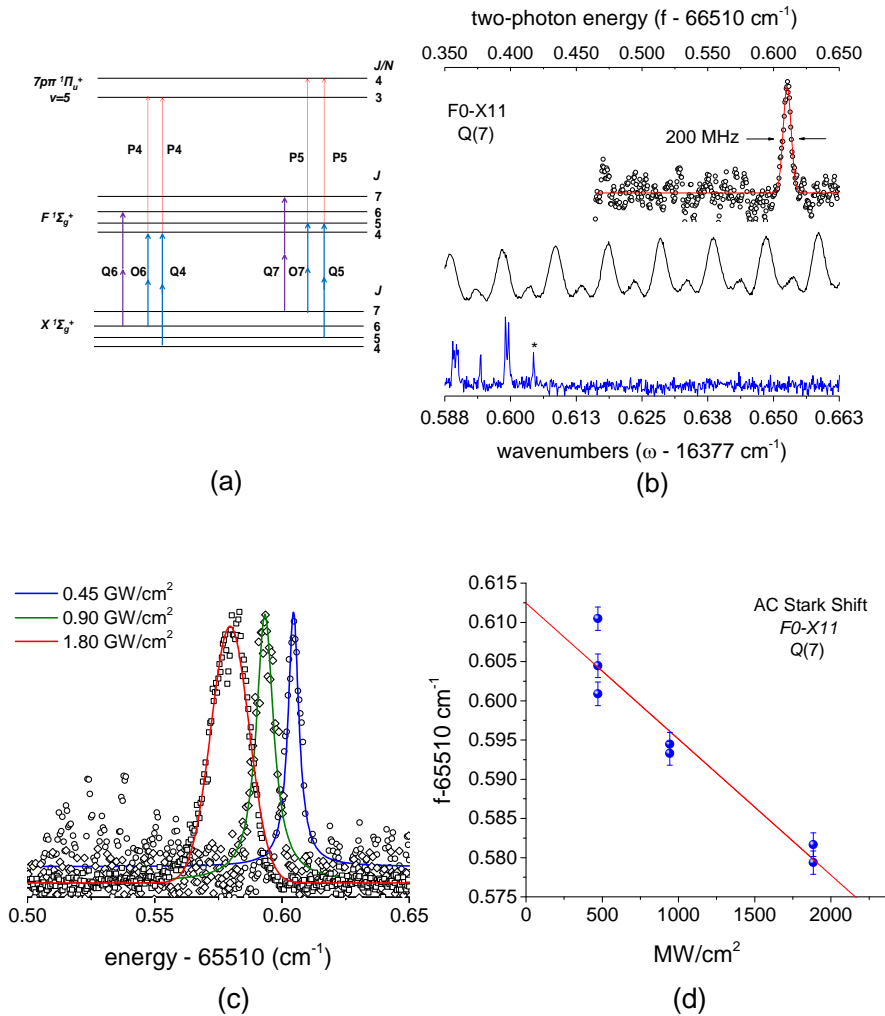


**Figure 3.4** (clockwise) (a) Level scheme for assigning  $J = 6$  and  $7$  of  $F(v = 0)$  (see text for details). (b) High precision Doppler-free spectrum of the  $Q(7)$  line calibrated using etalon markers with an FSR of 300.01 MHz and with respect to a reference ( $B-X$ )  $P(94)$  ( $12, 3$ )  $a_{15}$  hyperfine line of  $^{127}\text{I}_2$  at  $16377.60438 \text{ cm}^{-1}$ . (c) ac-Stark shift and broadening of the  $Q(7)$  line. (d) Linear extrapolation of ac-Stark shift to deduce the field free value for the  $Q(7)$  transition.

are ionized by one-photon electric dipole transitions  $P(4)$  and  $P(5)$  in the ionisation step, respectively. The  $P$ -branch transitions in the ionisation step connect to a known Rydberg electronic state  $7p\pi^1\Pi_u^+(v=5)$  [60], which readily autoionizes to  $H_2^+$ . Furthermore, the  $F-X$  transition pairs,  $Q(J)$  and  $O(J-2)$ , obey the ground state combination difference for the  $X11$  state. The energy difference  $Q(J) - O(J-2)$  agrees with the first principle calculations on the ground state [10] and thus provides a confirmation for the  $J \geq 5$  states in the survey scan range.

**Table 3.1** Results of high precision measurements on two transitions in the  $F-X(0,11)$  band which are assigned using combination differences and autoionising resonances. The experimental level energies are compared with the results from MQDT calculations for the  $F$  state from supplementary information of Dickenson *et al.* [86]. Values are given in  $\text{cm}^{-1}$ .

Line/ Transition energy <sup>a</sup>	$F(v=0)/$ Level energy <sup>b</sup>	Dickenson <i>et al.</i> [86]	Exp-Calc.
Q(6)/65731.2825(20)	J=6/99619.7840(57)	99621.16	-1.38
Q(7)/65510.6124(20)	J=7/99704.6413(56)	99706.04	-1.40

<sup>a</sup> Transition frequencies measured in this experiment

<sup>b</sup> Level energies are deduced using calculated energies of  $X(v=11, J)$  taken from Komasa *et al.* [10]

Once the presence of the hot rotational states is confirmed, Doppler-free REMPI studies are extended to  $Q(6)$  and  $Q(7)$  lines of the  $F - X(0,11)$  band to measure the  $J = 6, 7$  level energies of  $F0$ . The recorded two-photon spectrum is calibrated with transmission markers of a length stabilized confocal etalon and saturated  $B - X$  hyperfine spectral lines of  $I_2$  as shown in fig.3.4 (b). Systematic analysis to account for the ac-Stark effect on  $F - X$  two-photon transition is performed as illustrated in fig.3.4 (c) and (d), to deduce the field-free value for the transition energy from the extrapolation. Table 3.1, summarizes the assignment for the higher angular momentum levels of  $F(v=0, J)$  using this procedure. Since the knowledge of *ab initio* [93] and UV-FT [82] studies on the  $F0$  state is limited to  $J \leq 5$ , the level energies are compared with the MQDT calculations provided in the supplementary information of Dickenson *et al.* [86].

The previously explained empirical combination difference procedure can also be expected to extend to the ionization step. The photoionization of  $F0(J)$

### 3 Precision spectroscopy of the $EF^1\Sigma_g^+ - X^1\Sigma_g^+$ system in $H_2$ at large $R$

levels proceeds through the excitations to the three different autoionizing Rydberg channels with  $J - 1, J, J + 1$  extended into the continuum. Following the symmetry selection rules the  $P$ - and  $R$ - branch ionization channels connect to  $^1\Pi_u^+$  Rydberg states whereas the  $Q$ - branch channel involves  $^1\Pi_u^-$  states. This suggests there would be a partial overlap among autoionization spectra of adjacent  $F0(J)$  levels. For instance, we have observed few common resonances among the ionization spectra of  $Q(4)$  and  $Q(6)$  as well as  $Q(5)$  and  $Q(7)$  transitions of  $F - X(0, 11)$  band (presented in the later section 3.5). However, the accuracy of the combinational differences in the ionization step is limited for two reasons: (i) the natural width of the autoionization spectral lines is greater than  $2\text{ cm}^{-1}$ , and (ii) the current knowledge of Rydberg structure pertains only to  $J \leq 4$  for  $n > 2$ .

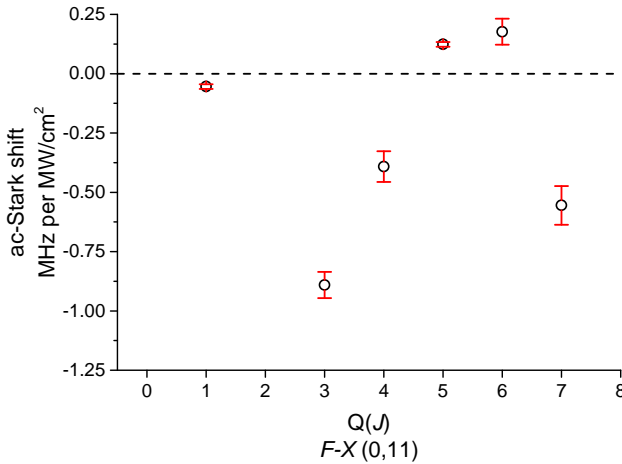


**Figure 3.5** ac-Stark shift coefficients for different  $Q$ -branch two-photon transitions of the  $F - X(0, 11)$  band. The coefficients for  $Q(J = 1, 3 - 5)$  are taken from Trivikram *et al.* [35].

Figure 3.5 indicates the rotational variation of ac-Stark coefficients ( $\alpha_{\text{stark}}$ ) for various  $Q$ -branch two-photon transitions of  $F - X(0, 11)$  band. Following the rotating-wave approximation and neglecting the Stark effect on the  $X$  state, it can be written as  $\Delta E_{\text{shift}} = \alpha_{\text{stark}} I$ , where  $I$  is the intensity (in

MW/cm<sup>2</sup>) and the Stark shift of two-photon transition (in cm<sup>-1</sup>) is given by

$$\Delta E_{\text{shift}} \propto \sum_m \frac{|\bar{\mu}_{mF} \cdot \bar{\epsilon}|^2}{E_{m_{v'J'}} - E_{F_{v''J''}} - h\omega} \quad (3.3)$$

Here  $\bar{\mu}$  is the transition dipole moment and  $\bar{\epsilon}$  is the electric field of the laser. Both the sign and magnitude of the coefficients result from the denominator of Eq. 3.3, which describes the detuning from all the allowed one-photon resonances ( $E_m - E_F$ ) connecting to the intermediate Rydberg levels as explained in the section 2.3 [35]. The rovibrational level energies of  $F$  and intermediate Rydberg states are given by  $E_{F_{vJ}}$  and  $E_{m_{vJ}}$ , respectively, and  $\omega$  is the frequency of the PDA laser. In addition, a rotational dependence due to the numerator of Eq. 3.3, was predicted theoretically for the double-minimum states like  $EF$  by Huo *et al.* [94]. Similar qualitative features like in fig 3.5 were envisaged for  $Q(J > 10)$  transitions to the inner-well state  $E(v = 0)$  and were attributed to the resonant tunneling in the double-well potential of  $EF$  state [94]. To explain the current trend, a better understanding of the entire excited quantum level structure is required which is beyond the scope of the present chapter.

### 3.3.3 Tentative assignments of transitions probing $X(v = 14)$

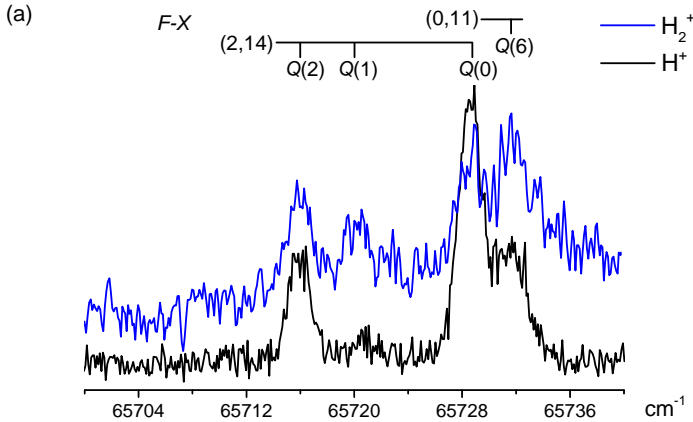
With more than an order improvement in the detection efficiency using the resonant ionization scheme, prospects have been spurred to investigate rovibrational states with wavefunction densities far beyond 4 a.u. One such interesting case is extending precision spectroscopic measurements to the highest vibrational level  $X(v = 14, J)$ , which has a binding energy less than 18 meV only. Due to their proximity to the dissociation limit, apart from the current precision studies, these loosely bound and far stretched molecular quantum states have significance in the fundamental reactive scattering studies at low temperatures [95] as well as in astrophysics and astrochemistry [96].

Though the preparation of  $v = 14, J$  levels via photodissociation of  $\text{H}_2\text{S}$  was reported in the work by Steadman and Baer [33], the assignment of transitions contradicts with the advanced studies on the  $X$  and  $EF$  states [10, 82]. For instance, reference [33] reported two-photon transitions from the  $X(v = 14, J = 4, 7)$  states. There exists only five bound rotational states associated with  $X14$  from the *ab initio* molecular theory of Komasa *et al.* and the  $J = 4$  level is weakly bounded ( $< 4 \mu\text{eV}$ ) in the non-adiabatic formalism

### 3 Precision spectroscopy of the $EF^1\Sigma_g^+ - X^1\Sigma_g^+$ system in $H_2$ at large $R$

only. The emission study of Dabrowski [97] also did not observe transitions with  $J > 4$ . Since the (4,14) band of  $EF - X$ , corresponding to (2,14) band of the  $F - X$  system, shows maximum wavefunction density overlap (FCF $\sim$ 0.38) [58], a two-colour survey scan similar to that of [32] is performed around 304.3 nm with a PDL II laser (refer fig 3.2). Figure 3.5(a) shows the recorded Doppler-limited REMPI spectra in the  $Q$ -branch region (65700–65730  $cm^{-1}$ ) of the  $F - X(2,14)$  band. The spectra are obtained independently using  $H^+$  as well as  $H_2^+$  ion signals by applying proper gating on the MCP. The resolution of these transitions is mainly limited by the Doppler width associated with recoiled photofragments  $H_2^*(v)$  (see the next section for details), the instrumental width ( $\sim 0.4$   $cm^{-1}$ ) for 2-photon transitions in UV) and the ac-Stark broadening as the probe intensities are in excess of  $\sim 15$   $GW/cm^2$ .

The spectral feature on the right is assigned as the  $Q(6)$  transition in the  $F - X(0,11)$  band as discussed above. The three other features on the left hand side are tentatively assigned as the  $Q(0)$ ,  $Q(1)$  and  $Q(2)$  two-photon transitions in the  $F - X(2,14)$  band. Two of these lines, exhibiting the best signal-to-noise ratio were subjected to a precision measurement with the narrowband PDA-system, employing the Sagnac-based counter-propagating geometry. Results from the high-precision studies, limited only by the bandwidth of the PDA laser (FWHM of 150 MHz on the linewidths) are displayed



[continued]

Doppler-free precision spectroscopy on  $F - X$  transitions

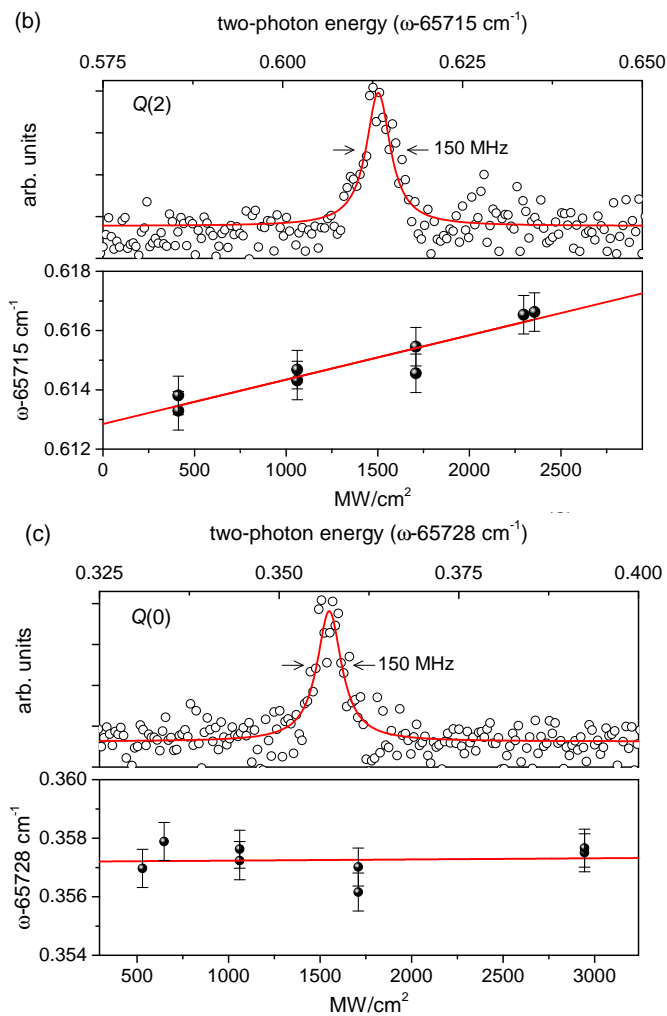


**Figure 3.5** (a) Broadband  $F - X$  REMPI survey scan performed with PDL II and under Doppler and ac-Stark-broadened conditions. The assignment of the  $F - X(2,14)$   $Q$ -lines is tentative. The upper panels of (b) and (c) show high resolution Doppler-free spectra of the peaks  $Q(0)$  and  $Q(2)$  lines of (a) and their corresponding ac-Stark analysis is illustrated in the lower panels of (b) and (c).

### 3 Precision spectroscopy of the $EF^1\Sigma_g^+ - X^1\Sigma_g^+$ system in $H_2$ at large $R$

in the upper panels of fig. 3.5(b,c). Also the ac-Stark effect on the transitions is investigated and transition frequencies are determined from their zero-intensity extrapolations as shown in lower panels of 3.5(b,c). From the reference etalon and saturated  $I_2$  spectroscopic based calibrations the absolute line positions of the  $Q(0)$  and  $Q(2)$  lines are thus determined to an accuracy of  $0.002\text{ cm}^{-1}$ . The transition frequency of the Doppler-broadened  $Q(1)$  transition derives from the calibration of the overview spectrum as displayed in fig. 3.5(a), resulting in an accuracy of  $0.3\text{ cm}^{-1}$ . The numerical values for the transition frequencies are listed in Table 3.2.

**Table 3.2** Measured transition frequencies of  $Q$ -branch lines in the two-photon  $F - X(2,14)$  band, and comparison with predicted values from Refs. [10, 82]. All the values are given in  $\text{cm}^{-1}$ .

Line <sup>a</sup>	Measured Line Position	Reference $F - X(2,14)$ <sup>b</sup>	Difference	Probe <sup>c</sup>	Comment
$Q(0)$	65728.3572(20)	65725.6788(26)	2.6784	NB	Doppler-free
$Q(1)$	65720.20(30)	65720.4139(17)	0.21	BB	Doppler, ac-Stark-limited
$Q(2)$	65715.6128(20)	65711.9063(15)	3.7065	NB	Doppler-free

<sup>a</sup> Peak positions are as marked in the survey scan, fig 3.6(a).

<sup>b</sup> Transition energies are deduced from the level energies of  $X(v = 14, J)$  taken from Komasa *et al.* [10] and those for  $F(v = 2, J)$  from Bailly *et al.* [82].

<sup>c</sup> NB - Narrowband studies with PDA laser, and BB - Broadband studies with PDL II laser (refer fig 3.2).

The assignment of the three lines to transitions in the  $F - X(2,14)$  band remains tentative, because the values are not in agreement with predictions from the *ab initio* calculations of the ground state,  $X$  [10] and the empirical values for the  $F$  levels from Bailly *et al.* [82]. Deviations of  $2.678\text{ cm}^{-1}$  and  $3.706\text{ cm}^{-1}$  are found for the accurately measured  $Q(0)$  and  $Q(2)$  lines, while the less accurately measured  $Q(1)$  line is found to be in agreement. For numerical details see also Table 3.2. The relative separation between the measured transitions  $Q(0)$  and  $Q(2)$  is found to differ by  $1.028\text{ cm}^{-1}$  from the predicted separation.

Using the complete set of rovibrational level energies for the  $X$  state from Komasa *et al.* [10], and all of those available for  $EF$  state from Bailly *et al.*

## $H_2^*(v)$ production via photolysis of $H_2S$ : Quantum-state specific kinetics

[82], an exhaustive search for Q, S and O transitions did not yield an alternative assignment. These possibilities show larger deviations and can be safely ruled out. It is known that to some extent the pairs of states,  $E_0, F_0$  and  $E_1, F_2$  are vibrationally degenerate [93, 98]. The change of electronic character between  $E_1$  and  $F_2$  states at  $J = 2$  and  $J = 3$  was experimentally noticed and is attributed to tunneling across the double well potential [98, 99]. However, the labeling does not match with the transitions involving the inner-well  $E$  levels also.

### 3.4 $H_2^*(v)$ production via photolysis of $H_2S$ : Quantum-state specific kinetics

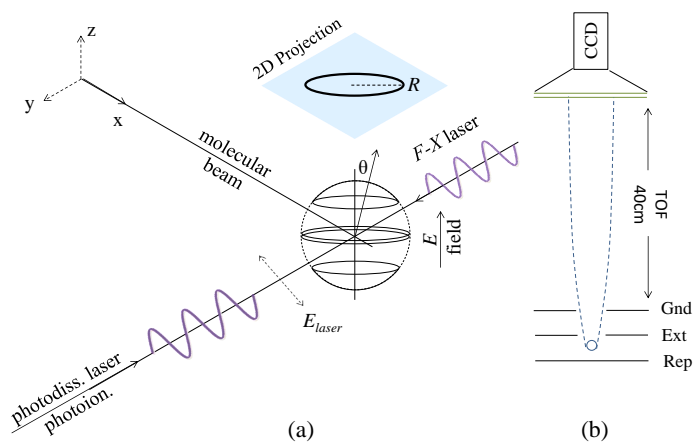
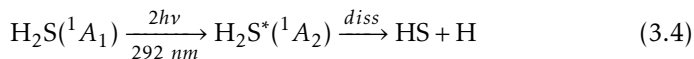


**Figure 3.6** (a) Experimental schematic for photofragment imaging studies on  $H_2S$ . The three-dimensional distribution of photofragments from the interaction volume are projected onto a two-dimensional surface. (b) Ion optics set up that focusses the  $H_2^*(v)$  onto the position sensitive detector after being ionised by spectroscopy and ionization lasers. Rep - Repeller, Ext - Extractor, Gnd - Ground and TOF- Time of flight tube.

A photofragment imaging method provides the crucial information about the quantum-state specific kinetics of the nascent  $H_2^*(v)$  produced from the

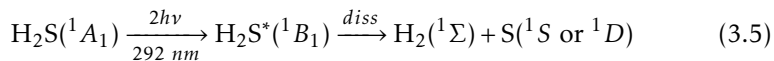
photodissociation of  $H_2S$ . The ion images depict the two-dimensional projections of the three-dimensional recoil of photoproducts [100] as shown in figure 3.6. In our velocity map imaging (VMI) set up, similar to the one developed by Eppink and Parker [87], both photodissociation (for  $H_2S$ ) and photoionization or probe (for  $H_2^*(v)$ ) lasers are focussed perpendicular to the direction of the molecular beam. The laser electric field polarization direction is kept parallel to the plane of imaging. Ions are focussed onto a position sensitive device (an MCP with phosphor screen coupled to a CCD camera) via extraction by an electrode grid whose field direction is normal to the image plane. The radial position on the two-dimensional intensity profile provides a direct measurement of the translational energy of the photofragments. Being heavier, the photoproducts like  $H_2S^+$ ,  $HS^+$  and  $S^+$  acquire negligible translational recoil momentum and are projected onto the origin in the image plane. The much lighter photoproducts  $H_2^+$  and  $H^+$  ( $m_S/m_H = 32$ ) emanate with higher recoil velocity and their Newton spheres are projected as concentric rings onto the 2-D image plane to represent the quantum-state specific energetics.

Two-photon photodissociation of  $H_2S$  at 292 nm ( $\sim 8.5$  eV) is mediated through the excitations to its Rydberg states, labelled as  $(2b_1)^1(3b_2)^1$  or  $^1A_2$  and  $(2b_1)^1(6a_1)^1$  or  $^1B_1$ , from the ground state,  $(2b_1)^2$  or  $^1A_1$  [101]. Being the members of  $n'p'b_2$  and  $n'p'a_1$  (a hybrid orbital with more-dominant 's' character) Rydberg series, the dissociation dynamics of these electronic states with  $^1A_2$  and  $^1B_1$  symmetries were spectroscopically studied in references [101, 102]. Both  $4pb_2/3b_2$  and  $4pa_1/6a_1$  molecular orbitals exhibit nodes along the S–H bonds and therefore lead to dissociation either directly or after following the excitation of a few vibrational states in these electronic states of  $H_2S$  [103]. However, the  $^1A_2$  state dissociates into  $HS+H$  and the antibonding nature of the H–H interaction in the  $3b_2$  orbital most likely produces separate H atoms upon photodissociation (chemical reaction 3.4) [101, 103].



Conversely, there is a nonnegligible bonding overlap between the spatial distribution of electrons between two H atoms, in case of the Rydberg  $6a_1$  orbital [103]. Thus, the other state with  $^1B_1$  symmetry dissociates directly into  $H_2+S$  (chemical reaction 3.5).

$H_2^*(v)$  production via photolysis of  $H_2S$ : Quantum-state specific kinetics



Also in case of the  $H_2O$  molecule, Mulliken [104] envisaged a possible dissociation pathway into  $O(^1D)+H_2(^1\Sigma_g^+)$ , and an explanation via a similar kind of transition ( $1b_1 \rightarrow 4a_1$ ) was given by Herzberg [105]. Following the Frank-Condon principle, the interatomic distance should remain unchanged during the photodissociation. Since the interatomic separation between H-atoms in the  $^1B_1$  state is  $1.95 \text{ \AA}$ , the nascent photoproduct  $H_2$  should be formed in highly excited vibrational quanta i.e.  $v = 10 - 14$ . These states were first experimentally observed by Steadman and Bear [33]. Recently, Niu et al. [32] reinvestigated hot vibrational states of  $H_2$  by employing non-resonant  $H^+$  ion detection upon REMPI excitation.

The  $H_2S$  molecule has  $C_{2v}$  symmetry and for a transition between  $^1A_1$  to  $^1B_1$  states i.e. from the ( $2b_1$ ) to the ( $6a_1$ ) orbital, the transition dipole moment is perpendicular to the plane of the molecule. This was confirmed in the earlier UV studies by measuring the anisotropy factor ( $\beta$ ) for the photofragments to be in between  $-0.5$  [106] to  $-1$  [107]. For these perpendicular transi-

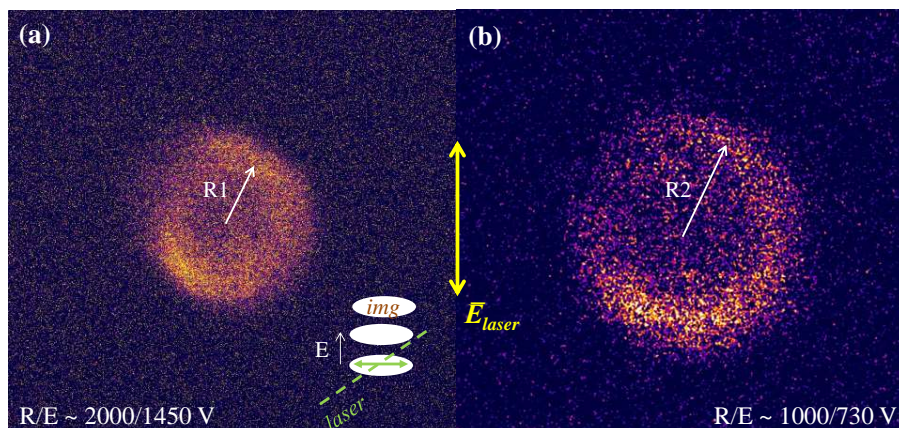


**Figure 3.7** Two-dimensional projections of recoiled  $H_2^*$  molecules at two different voltage combinations on ion optics, in their  $X^1\Sigma_g^+(v = 11, J = 5)$  quantum state. The laser polarisation of the the photolysis laser is kept parallel to the plane of imaging as shown in the inset.

tions the photofragment distribution may be described as an equatorial belt and a  $\sin^2\theta$  intensity distribution is produced, unlike the  $\cos^2\theta$  distribution for parallel transitions. This was further demonstrated from the two-dimensional imaging of H atoms recoiled from the photodissociation of  $H_2S$  at 243 nm ( $H_2S^* \rightarrow H+SH$ ;  $H/SH \xrightarrow{h\nu} H^+$ ) and the observations pertained to the first excitation continuum only [108].

Our studies are focussed on dissociative states above  $65000\text{ cm}^{-1}$  using two-photon excitation at 291.75 nm similar to that in references [33, 109]. In this study, a second spectroscopy step exciting the  $F - X$  transition, and a subsequent third ionization step, define a specific  $H_2(v^*, J)$  quantum state to be probed in the VMI-detection scheme for analyzing the dissociation. Apart from quantum-state specific kinetics, imaging  $H_2^+$  ions provides an additional advantage of zero background from other dissociative pathways, which is not the case for imaging  $H^+$ .

The raw 2-D projection of velocity distributions of recoiled  $H_2^+(v)$  for its  $X^1\Sigma_g^+(v = 11, J = 5)$  state are depicted in figure 3.7. The images are recorded at two different combinations of voltages applied on an electrostatic lens. The radius  $R$  of the  $H_2^+$  ion distribution in the image is related to the repeller voltage ( $V_R$ ) and the kinetic energy ( $T$ ) of  $H_2^+(v)$  photofragments by the relation,  $R \propto f_m \sqrt{T/(qV_R)}$ . The magnification factor  $f_m$  is estimated to be 1.3. The excited  $(4pa_1)^1B_1$  state of  $H_2S$  dissociates and leaves about 5.6 eV available for the internal and translation energy of the photoproducts ( $H_2+S$ ) [33, 106]. Following the Franck-Condon dissociation, the internal energy distribution for  $H_2^+(v, J)$  in its electronic ground state ( $X^1\Sigma_g^+$ ) is in between 3.85 eV to 4.45 eV. The internal energy of the S atom can be distributed among its three low-lying atomic states,  $^3P$ ,  $^1S$  and  $^1D$ , whose energies are 0 eV, 1.14 eV, and 2.75 eV, respectively. Though it is energetically feasible, the dissociation pathway  $H_2S(^1B_1) \rightarrow H_2(^1\Sigma_g^+) + S(^3P)$  is disallowed by the spin conservation rule,  $\Delta S = 0$  (singlets correlate with singlets) [33, 105, 109]. The formation of  $S^*$  ( $^1D$ ) in conjunction with  $H_2^+(v)$  violates energy conservation. The favorable dissociation channel is that with production of the S atom in its  $^1S$  state, lying  $9239\text{ cm}^{-1}$  above the ground state ( $^3P$ ). Due to heavier mass ( $m_S/m_{H_2} = 16$ ) the recoil momentum of the  $S^*$  atom is negligible compared to that of  $H_2^+(v)$ . From the radius of the recorded image, the vibrational quantum state of  $H_2^+(v)$  can be assessed. The radius of the recorded image is estimated to be  $\sim 5.1\text{ mm}$  (each pixel of CCD corresponds to 35 microns). The velocity of the photoproduct can be obtained by the relation,  $R = f_m ut$ , where

## $\text{H}_2^*(v)$ production via photolysis of $\text{H}_2\text{S}$ : Quantum-state specific kinetics

$u$  is the velocity of the photofragment that is projected in the image plane, and  $t$  is the travel time to the detector. The corresponding recoil energy associated with 2-D projections in figure 3.7 is about  $\sim 0.31$  eV. That means an amount of  $\sim 4.14$  eV is contained in the internal energy of  $\text{H}_2^*(v)$ , closely coinciding with the level energy of  $X(v = 11, J = 5)$ .

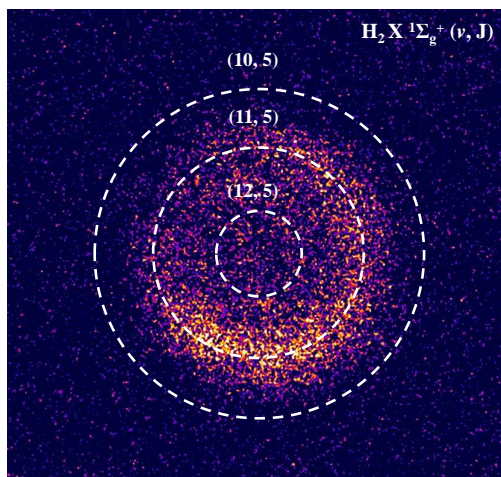


**Figure 3.8** Velocity map image of  $\text{H}_2\text{S}$  two-photon photolysis at  $\lambda = 291.75$  nm, probing the  $X(v = 11, J = 5)$  state of  $\text{H}_2$ . Rings indicate expected positions of adjacent vibrational products.

Under similar experimental conditions, the molecules prepared in  $v = 10$  and 12 states should acquire recoil velocities of 4750 m/s and 1250 m/s respectively for  $J = 5$ . The expected velocity projections for the  $\text{H}_2(v)^*$  molecule in adjacent vibrational state  $v = 10$  or 12 along with  $v = 11$  are indicated in figure 3.8. Given the quality of the acquired image, it is only possible to identify vibrational quantum state. To obtain sharper images for extracting also the rotational quantum number, improvements to the existing ion optics have to be made.

The velocity map imaging method explained complements the  $E, F - X$  Doppler-free REMPI precision measurements discussed in the previous section. In future studies, it can be implemented in the  $F - X$  system as discussed in the section 3.3.3. and to retrieve crucial information about the ground vibrational quantum state. Another possible application of combin-

ing the imaging with high precision spectroscopy on a resonance at 64, 890  $\text{cm}^{-1}$  observed in another two-colour broadband survey scan (not shown here) on the  $F - X$  system. This resonance here can be ascribed to two possible transitions either the  $Q(4)$  line of the  $F - X(0,12)$  band or the  $Q(6)$  line of the  $F - X(1,13)$  band, situated  $0.7 \text{ cm}^{-1}$  apart from each other. These two transitions can be resolved if their KER is projected onto a 2D image with improved ion optics. Interestingly, the velocity associated  $H_2$  molecules with  $X(v = 13, J = 6)$  state would be  $\sim 15 \text{ m/s}$  only. Preparing such slowly moving molecules in laboratory frame would improve the experimental accuracy of high precision spectroscopic measurements of  $H_2$ .

### 3.5 Autoionization from outer-well levels $F^1\Sigma_g^+(v = 0, J = 4 - 7)$

The current study employs the  $H_2$  super-excited states in the energy region  $6,675 - 8,525 \text{ cm}^{-1}$  above the ionization threshold for the resonant excitation and detection of  $F(v = 0, J)$  outer well states in order to produce signal in the spectroscopic study of  $F - X$  transitions. Earlier synchrotron investigations on these superexcited states suggested that for the excitations beyond the ionization potential (I.P.) and  $n \geq 5$ , the autoionization completely dominates over the other two competing decay processes, fluorescence and dissociation [64]. Autoionization spectra are recorded by scanning a frequency-doubled output of pulsed dye laser (PDL II), after the photolysis (PDL I) and spectroscopy (PDA) lasers have been excited a certain  $F(v = 0, J)$  intermediate level. Spectra are calibrated using standard Doppler broadened  $I_2$  absorption lines in the spectral region of  $15,775 - 16,675 \text{ cm}^{-1}$ . Our frequency calibration in the doubled UV regime is accurate to  $0.05 \text{ cm}^{-1}$ . The photoionization beam interacts with  $H_2$  molecules in the  $F0$  state flying equatorially in all directions with a recoil momentum of  $\sim 0.3 \text{ eV}$ . It results in Doppler broadening in the order of 10 GHz which is smaller than the natural linewidth of autoionising resonances, generally about few wavenumbers broad [110]. Figures 3.9 to 3.12 show the observed autoionization spectra in the energy region of  $131,100 - 133,000 \text{ cm}^{-1}$  recorded from  $F(v = 0, J)$  levels.

The autoionization spectra of diatomic molecules, displaying Rydberg-continuum state interactions, has been successfully explained with the MQDT formalism [110]. Briefly, MQDT is essentially a generalized form of scattering theory that is extended to include bound states of a molecule (closed channels) along with different continua (open channels) associated either with ion

Autoionization from outer-well levels  $F^1\Sigma_g^+(v=0, J=4-7)$

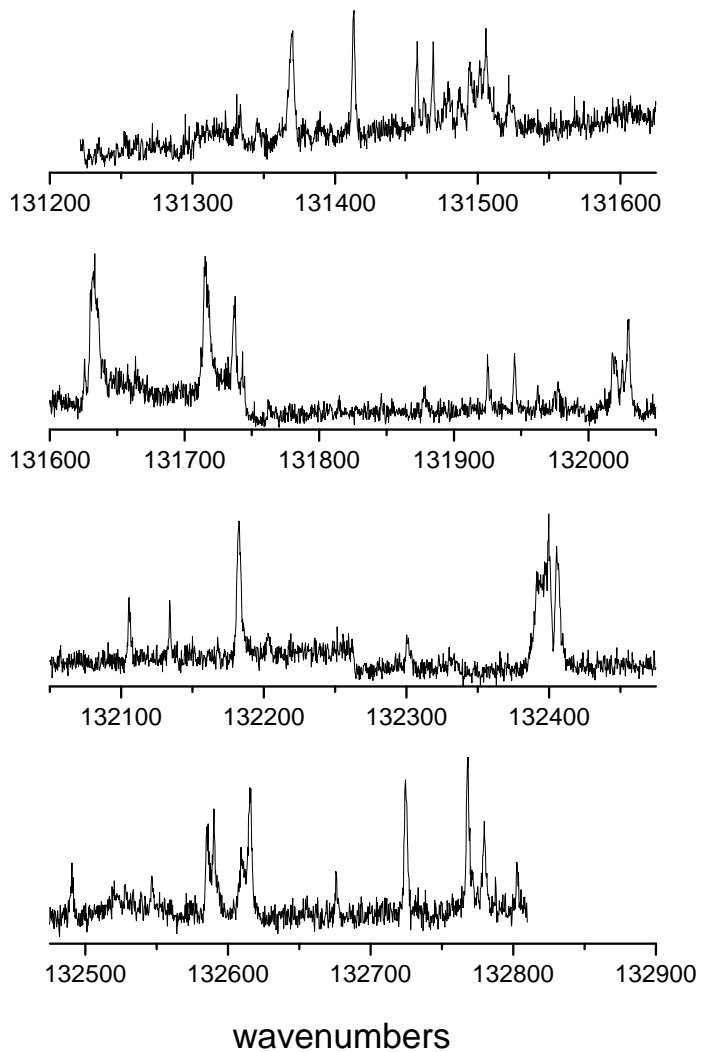


**Figure 3.9** Autoionization spectra recorded from  $F^1\Sigma_g^+(v=0, J=4)$  state.

3 Precision spectroscopy of the  $EF^1\Sigma_g^+ - X^1\Sigma_g^+$  system in  $H_2$  at large  $R$

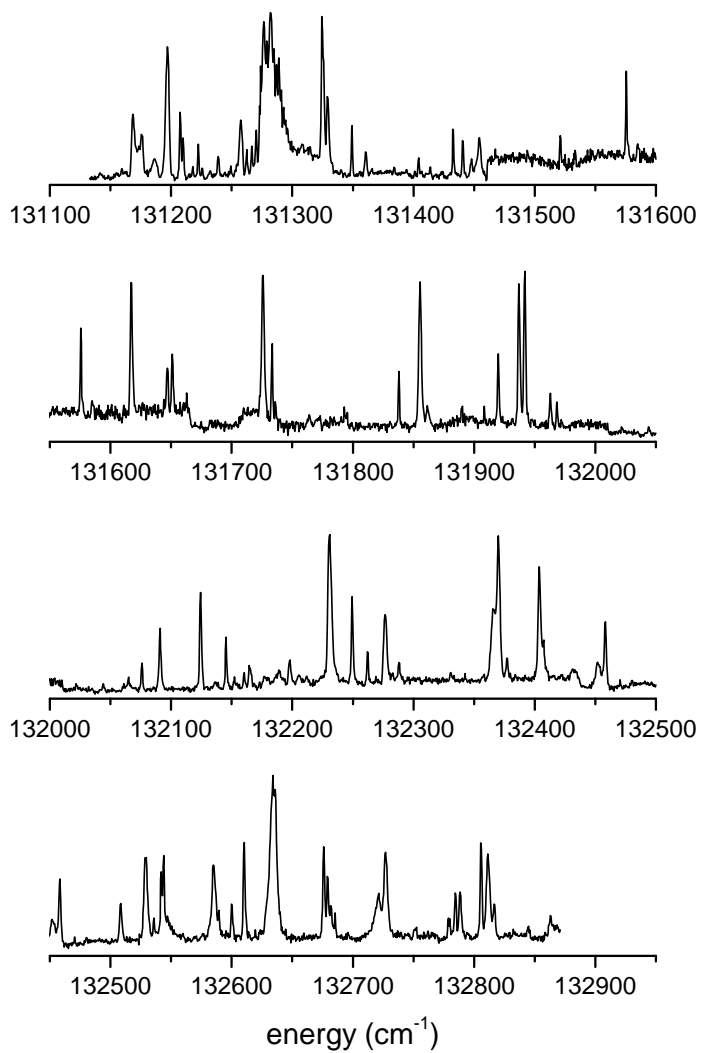


**Figure 3.10** Autoionization spectra recorded from  $F^1\Sigma_g^+$  ( $v = 0, J = 5$ ) state.

Autoionization from outer-well levels  $F^1\Sigma_g^+$  ( $v=0, J=4-7$ )

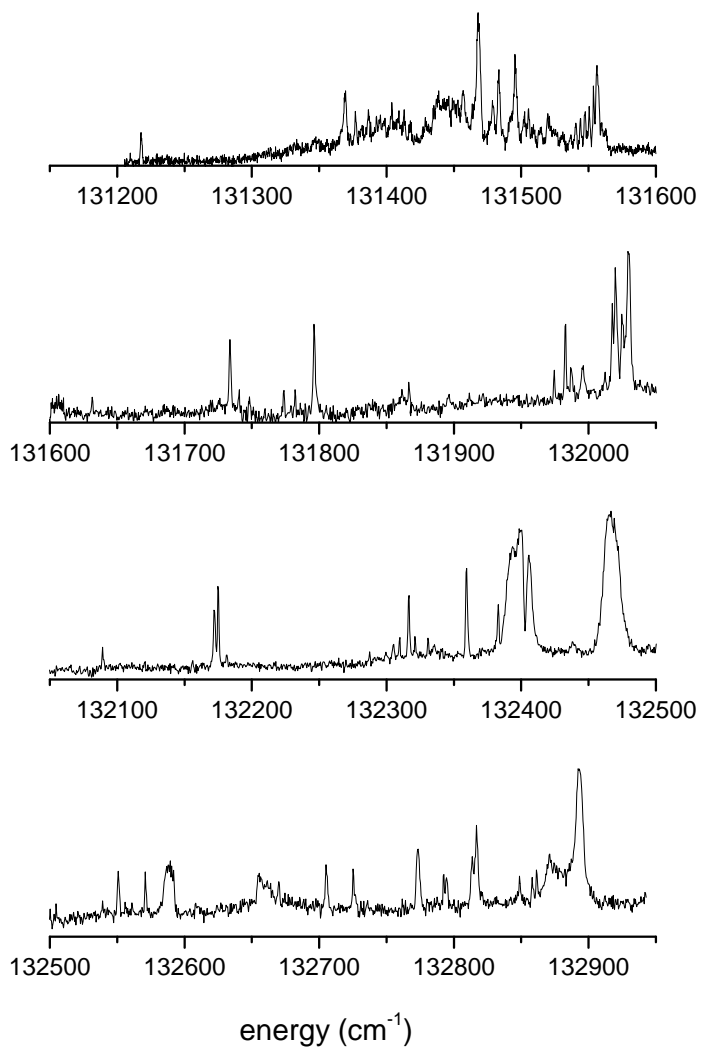


**Figure 3.11** Autoionization spectra recorded from  $F^1\Sigma_g^+$  ( $v=0, J=6$ ) state.

3 Precision spectroscopy of the  $EF^1\Sigma_g^+ - X^1\Sigma_g^+$  system in  $H_2$  at large  $R$

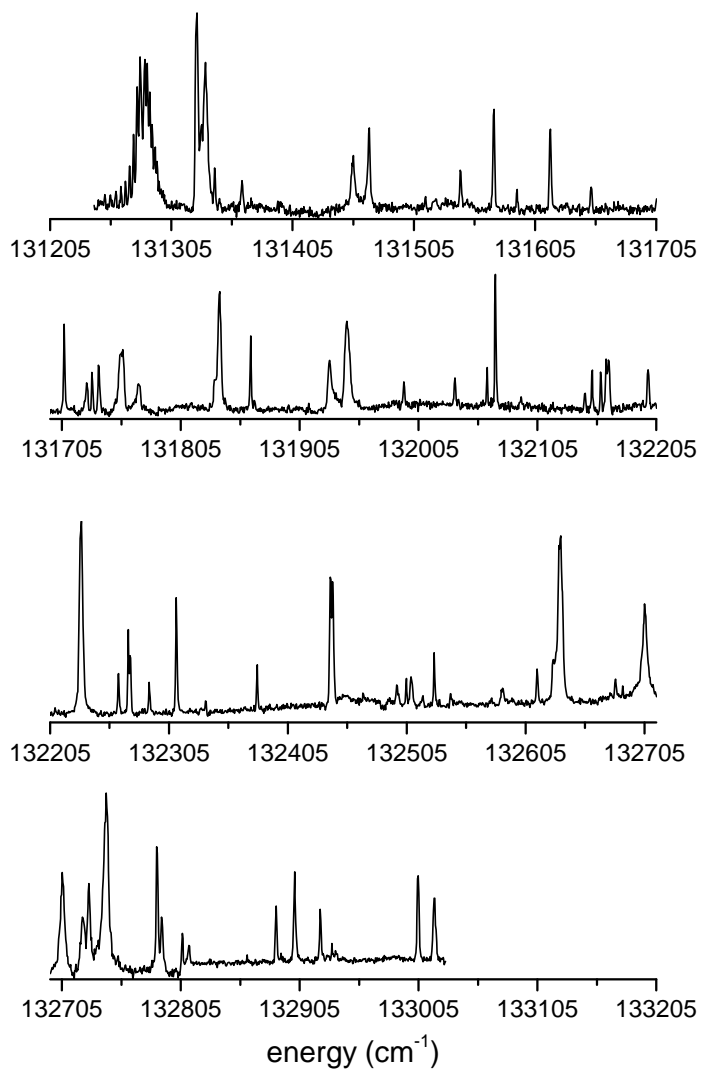
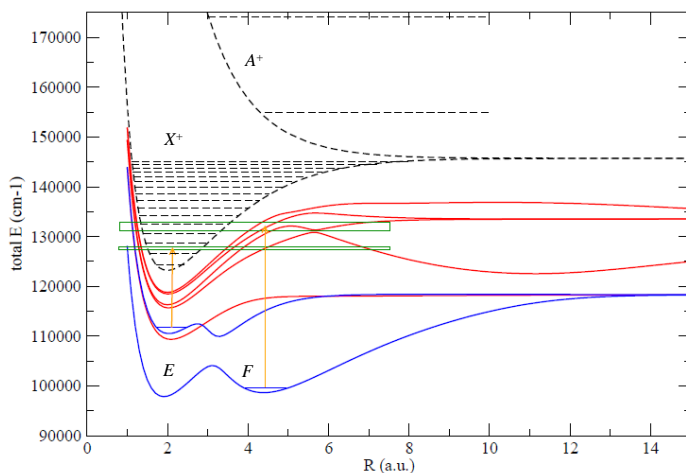


Figure 3.12 Autoionization spectra recorded from  $F^1\Sigma_g^+$  ( $v = 0, J = 7$ ) state

Autoionization from outer-well levels  $F^1\Sigma_g^+$  ( $v=0, J=4-7$ )



**Figure 3.13** Potential curves for the Rydberg states of the  $H_2$  molecule and the ion states that are relevant for the current studies in the region of  $1311000$ - $133000\text{ cm}^{-1}$  (figure reproduced with permission from Ch. Jungen).

core or dissociation of the molecule. Though a similar energy region was covered in the recent VUV studies and explained by MQDT [60–62], the present spectroscopic interrogations are distinct from previous studies on Rydberg states of  $H_2$  [60–63, 88–90] for the following reasons:

(i) Unlike the photoionization spectra of the ground  $(1s\sigma)^2X$  state and inner-well states like  $(1s\sigma 2s\sigma)E$ , the spectra displayed in fig 3.9 to 3.12 probe the autoionization from an outer-well state  $F(v=0)$  where the wave function density is situated around  $\sim 4.4$  a.u. At this relatively large internuclear separation, the potential curve of  $F$  state is not parallel to that of  $X^+$  state of the ion,  $H_2^+$  as shown in fig 3.13. In such a case, to interpret the spectra in the framework of MQDT, it would require to develop  $R$ -dependent quantum defects along with their energy dependent form [110, 111].

(ii) The current study probes the autoionization spectrum of a doubly excited electronic state  $(2p\sigma)^2 F^1\Sigma_g^+$  of  $H_2$ . Following the MQDT representation of states, the  $F$  state has intrinsically more character of the excited electronic state of the ion core,  $A^+(2p\sigma_u)$ . The theory requires an extension to inter-

### 3 Precision spectroscopy of the $EF^1\Sigma_g^+ - X^1\Sigma_g^+$ system in $H_2$ at large $R$

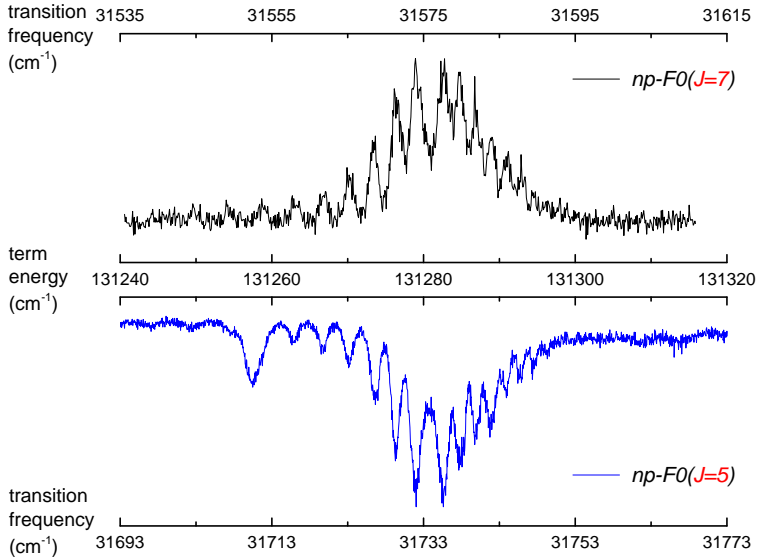


**Figure 3.14** Complex resonances observed in the same energy region from the excitation of two *ortho*- states,  $F(v = 0, J = 5$  and  $7)$ .

pret simultaneously both the de-excitation of  $A^+$  character to  $(1s\sigma)X^+$  as well as excitation outer well  $(2p\sigma)F$  electron to  $np$  Rydberg manifold, via a one-photon electric dipole transition.

(iii) In the regions above  $131,000 \text{ cm}^{-1}$  and as  $R \rightarrow 5 \text{ a.u.}$  the  $np$  Rydberg structure of  $H_2$  gets complicated by interactions with higher order partial waves ( $f$  and  $h$ ), and thus producing avoided crossings as shown in *ab initio* potential curves of fig 3.13 [60, 62, 112].

(iv) Finally, the present observations are made for higher angular momentum levels  $J = 4 - 7$  of  $H_2$ . This was not possible in the earlier VUV studies [60–62] probing the ground state  $X(v = 0)$  at room temperature, with population limited to  $J \leq 4$ . The study of Glass-Maujean *et al.* [113] extends to  $J = 6$  of Rydberg states in  $D_2$ , but the probing was limited to  $R \leq 2 \text{ a.u.}$  Future MQDT-analysis may incorporate these considerations to interpret the experimentally observed autoionisation spectra, i.e. figures 3.9 to 3.13.

Despite the lack of the theoretical interpretation, a few remarks can be made from the observed spectra. There are few overlapping regions in the

Autoionization from outer-well levels  $F^1\Sigma_g^+(v=0, J=4-7)$

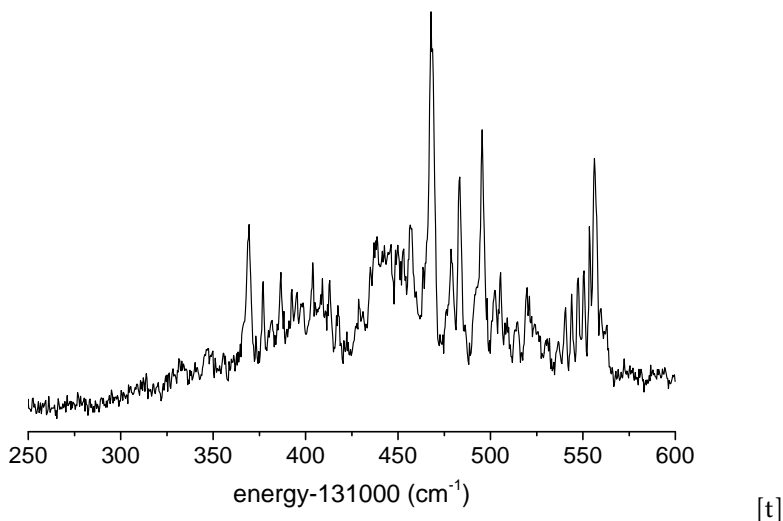


Figure 3.15 Complex resonances observed from a *para*- state,  $F(v=0, J=6)$

autoionization spectra of two-*ortho* ( $J=5,7$ ) levels (fig. 3.10, 3.12) and those of two-*para* ( $J=4,6$ ) levels (fig. 3.9, 3.11). Each  $F(v=0, J)$  level is photoionized via three different autoionizing Rydberg series converging onto  $X^+(v^+, J^+ = J+1, J, J-1)$  state of the ion. This is evident from a few isolated spectral lines and also in the case of ‘complex’ resonances. For example, the resonance shown in figure 3.14 represents a Rydberg series possibly arising from *R*-branch transitions from  $J=5$  and *P*-transitions from  $J=7$ , sharing the same Rydberg structure. These complex resonances occur when the perturbing Rydberg configurations or series along with different continua, sometimes including dissociation, are coherently excited [114, 115]. Similar resonance profiles were observed in earlier studies of Dehmer and Chupka [88], and Glass-Maujean *et al.* [60, 61]. These profiles represent the typical nature of the non-adiabatic coupling between the electron excitation, i.e. increment in  $n$  of Rydberg series, associated with the corresponding change (decrease) in the nuclear (core) vibrational quanta or vice versa [110]. Similarly, another more complicated spectral feature observed from a *para*  $J=6$  level as shown

in fig 3.15 strongly requires extensions to MQDT to understand the Rydberg continuum interactions in  $H_2$  from internuclear separation beyond 4 a.u.

### 3.6 Conclusion

This chapter revisits the  $EF - X$  system in the  $H_2$  molecule by probing the wavefunction densities at  $R \geq 4$  a.u. Doppler-free REMPI measurements are extended to vibrationally as well as rotationally hot molecular levels  $X^1\Sigma_g^+(v = 11, J = 6, 7)$ , produced via photolysis of  $H_2S$ . The importance of resonant ionization detection using autoionization resonances towards detection, assignment and improving ac-Stark analysis of the  $F - X$  transitions is discussed in detail. A tentative assignment for the transitions from the highest vibrational state,  $X(v = 14)$  has been made based on precision spectroscopic studies measured with an accuracy of 60 MHz. The velocity map imaging method is implemented for imaging the  $H_2^*(v = 11)$  molecules to understand the quantum state specific translational kinetics of  $H_2S$  photofragments. Finally, the study provides the autoionization spectra for the higher angular momentum levels  $J = 4 - 7$  aiming to investigate the Rydberg-continuum interactions from a doubly excited outer-well state  $F$  for the first time.

---

## CARS spectroscopy of the ( $v = 0 \rightarrow 1$ ) band in $T_2$

### Abstract

Molecular hydrogen is a benchmark system for bound state quantum calculation and tests of quantum electrodynamical effects. While spectroscopic measurements on the stable species have progressively improved over the years, high-resolution studies on the radioactive isotopologues  $T_2$ , HT and DT have been limited. Here we present an accurate determination of  $T_2$   $Q(J = 0 - 5)$  transition energies in the fundamental vibrational band of the ground electronic state, by means of high-resolution Coherent Anti-Stokes Raman Spectroscopy. With the present experimental uncertainty of  $0.02 \text{ cm}^{-1}$ , which is a fivefold improvement over previous measurements, agreement with the latest theoretical calculations is demonstrated.

## 4.1 Introduction

Molecular hydrogen and its isotopologues are benchmark systems where the most refined quantum chemical theories can be applied. Its energy level structure can be calculated to the highest accuracy of any neutral molecule, which include the Born-Oppenheimer (BO) contribution, nonrelativistic BO corrections as well as relativistic and radiative (quantum electrodynamic or QED) contributions [8, 10]. Adiabatic and nonadiabatic effects are prominent in molecular hydrogen due to the lightness of the nuclei, and thus analogous studies on the different isotopologues provide a handle for a better understanding of these contributions to the level energies.

The ground state level energies and transitions in H<sub>2</sub>, HD and D<sub>2</sub> have been determined at ever increasing accuracies, with the recent accurate studies employing cavity-enhanced techniques ( e.g. [27, 116–119] ) or pulsed molecular beam spectroscopies [23, 24]. The dissociation energy  $D_0$ , a benchmark quantity in quantum molecular calculations, have also been determined to a high accuracy [22, 120, 121] by combining the results of several precision spectroscopies. The comparison of the results from measurements and calculations enable precision tests of QED, and even test of new physics beyond the Standard Model [28].

While numerous precision spectroscopic studies on the stable molecular hydrogen isotopologues have been performed, the tritium-bearing species HT, DT and T<sub>2</sub> are not as well studied because of the limited access to radioactive tritium. The comprehensive classical spectroscopy of Dieke [122] on all isotopologues of molecular hydrogen included tritium-containing species. Laser Raman spectroscopic studies were carried out on the pure rotational (0-0) and fundamental vibrational (1-0) bands by Edwards, Long and Mansour [123] for T<sub>2</sub> and later for HT and DT [124]. Veirs and Rosenblatt [125] also performed Raman spectroscopy on all molecular hydrogen species, however, they reported discrepancies with Ref. [123, 124] that exceeded the claimed uncertainties of those previous determinations. Chuang and Zare [126] performed high-resolution measurements on the (1-0), (4-0) and (5-0) bands of HT using photoacoustic techniques. They pointed out discrepancies when comparing to the *ab initio* calculations by Schwartz and LeRoy [127] that may stem from the treatment of nonadiabatic corrections.

The molecular structure of the tritiated hydrogen isotopologues in the electronic ground state is also relevant in experiments which aim at the de-

## Experiment

termination of the mass of the neutrino, like the Karlsruhe Tritium Neutrino experiment (KATRIN) [128]. The mass is deduced from high-resolution electron spectroscopy of the decay electrons from the molecular beta-decay of tritium,  $T_2 \rightarrow {}^3\text{HeT}^+ + e^- + \bar{\nu}_e$ . After the decay, the helium-tritium ion remains in an excited electronic, vibrational and/or rotational state [129]. This internal excitation energy reduces the kinetic energy carried away by the electron, which acts as the central kinematic observable in the neutrino mass measurements. The probability of excitation of these states is currently only accessible via theory [130, 131]. These calculations crucially depend on the energy levels of the initial states of  $T_2$  and final states of  ${}^3\text{HeT}^+$ .

In this contribution, we present our determination of the Q-branch transitions of the  $T_2$  fundamental band ( $v = 0 \rightarrow 1$ ) in the ground electronic state. We employed Coherent Anti-Stokes Raman spectroscopy (CARS) [132] using narrowband pulsed lasers on a low-pressure gas cell containing tritium. Comparison with previous experimental determinations demonstrate agreement with Ref. [125], while comparison with calculations in Ref. [52] indicate that relativistic and QED contributions are smaller than the present measurement accuracy.

## 4.2 Experiment

For the high resolution CARS measurements a new tritium compatible cell was developed based on the concept of the standard Raman cells at the Tritium Laboratory Karlsruhe (TLK) [133, 134]. Tritium-compatibility is guaranteed by employing well-proven materials only, such as stainless steel or certain fused silica windows with metal-to-window sealings. It should be noted that rubber- or plastic-based materials cannot be used due to deterioration by radiochemical reactions induced by the beta-emitter. The inner volume of the cell should be as small as possible to reduce the activity of the tritium gas sample at a certain pressure. On the other hand the length of the cell needs to be long enough, so that the energy density of the laser pulses at the window surface does not exceed the damage threshold. In our design a good compromise was found at a length of 80 mm, which resulted in a total inner cell volume of  $4 \text{ cm}^3$ . Tritium gas was prepared at high purity by performing displacement gas chromatography and gettering on uranium beds at the TLK [135] and filled into the cell at about 2.5 mba. This corresponds to an activity of less than 1 GBq which is the legal limit for handling tritium

#### 4 CARS spectroscopy of the ( $v = 0 \rightarrow 1$ ) band in $T_2$

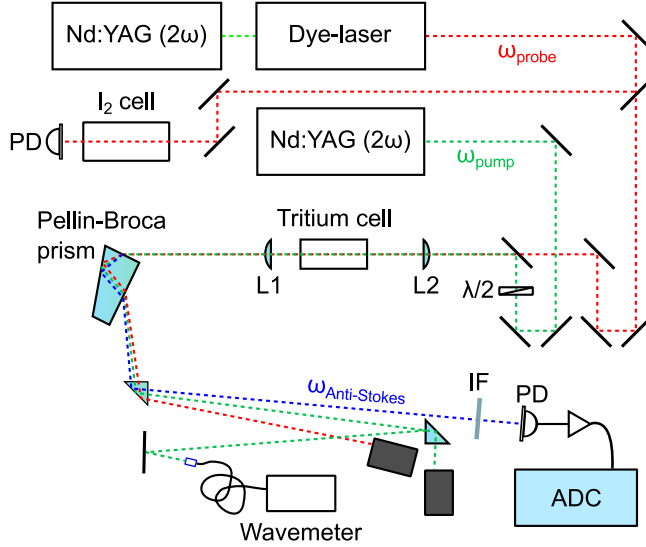


**Figure 4.1** Schematic diagram of CARS setup.  $\lambda/2$ : half-wave plate; L1, L2: lenses; IF: interference filter; PD: photodiode.

outside of a licensed lab. The composition of the sample was measured by Raman spectroscopy [136]:  $T_2$ : 93.4%, DT: 4.9%, HT: 1.4%,  $H_2$ : 0.2% and  $D_2$ : 0.1%. Subsequently, the cell was decontaminated to allow transporting to the CARS setup at LaserLab Amsterdam.

A schematic diagram of the setup is shown in Fig. 4.1. The frequency-doubled output, at 532 nm, of an injection-seeded Nd:YAG pulsed laser (Spectra Physics 250-10 PRO, 10-Hz repetition rate) was used as the pump radiation  $\omega_{\text{pump}}$ . The tunable probe beam  $\omega_{\text{probe}}$ , at  $\sim 612$  nm, is the output of a pulsed dye laser (Lioptec LiopStar) running on a mixture of Rhodamine B and Rhodamine 640 that is pumped by another Nd:YAG pulsed laser. The pump and probe beams are spatially combined and subsequently focused by a lens L2, focal length  $f = 30$  cm, into the tritium cell and collimated by another lens L1, focal length  $f = 10$  cm, after the cell. The probe, pump and anti-Stokes signal  $\omega_{\text{anti-Stokes}} = 2\omega_{\text{pump}} - \omega_{\text{probe}}$  beams are then dispersed by a Pellin-Broca prism, where the signal beam ( $\sim 470$  nm) passes through an optical interference filter (bandwidth 10 nm) before collection onto a pho-

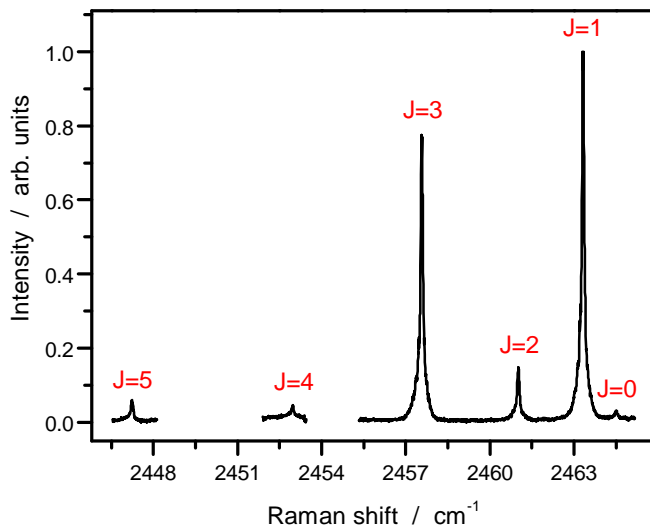


**Figure 4.2** High-resolution spectrum of Q-branch in the fundamental band of  $T_2$ . The lines shown were recorded at pump/probe pulse energies of 5 mJ, except for  $J = 4$  which was recorded at 7.5 mJ.

todetector. The temporal overlap of the pump and probe pulses is optimized by changing the trigger timings of the Nd:YAG lasers.

During the measurement, the wavelength of  $\omega_{\text{pump}}$  is measured continuously (around  $18789.0302(10) \text{ cm}^{-1}$ ) using a wavemeter (High Finesse Angstrom WSU-30). The probe radiation  $\omega_{\text{probe}}$  wavenumber is scanned, while simultaneously a portion of  $\omega_{\text{probe}}$  is diverted into an  $I_2$  absorption cell, where the Doppler-broadened absorption lines of the latter are used as calibration reference [137]. The iodine calibration lines are shown together with a selected Raman line in Fig. 4.3. The wavenumber calibration of  $\omega_{\text{pump}}$  is estimated to be better than  $0.002 \text{ cm}^{-1}$ , while the calibration accuracy of  $\omega_{\text{probe}}$  is estimated at  $0.01 \text{ cm}^{-1}$ .

### 4.3 Results and discussion

The observed  $Q(0) - Q(5)$  transitions ( $v = 0 \rightarrow 1, \Delta J = 0$ ), plotted against the Raman shift ( $\omega_{\text{anti-Stokes}}$ ), are shown in Fig. 4.2. Good signal-to-noise ratio is obtained even for the weakest lines for 7.5 mJ pulse energy for both the

pump and probe beams, where the linewidths are observed to be  $\sim 0.15 \text{ cm}^{-1}$ . The relative intensities of the CARS signal follow the expected behaviour of  $I_{\text{CARS}} \propto N^2$  with  $N$  being the number density by considering Placzek-Teller Raman line strength coefficients and a room temperature partition function [138].

The Doppler width of the T<sub>2</sub> Q transitions at room temperature is  $0.014 \text{ cm}^{-1}$ . In order to estimate the effect of ac-Stark broadening, the Q(1) transition was recorded at lower pulse energies of 1 mJ for both pump and probe beams, see Fig. 4.3. Even at these reduced pulse energies, the linewidth is observed to be  $\sim 0.1 \text{ cm}^{-1}$ , which we attribute to be mainly limited by the probe laser ( $\omega_{\text{probe}}$ ) instrument bandwidth. This is confirmed by the fitted linewidths of the I<sub>2</sub> calibration resonances of  $\sim 0.08 \text{ cm}^{-1}$ , used for calibrating  $\omega_{\text{probe}}$ , while the expected I<sub>2</sub> Doppler width is  $\sim 0.03 \text{ cm}^{-1}$ . The instrument linewidth of the pump laser  $\omega_{\text{pump}}$  is estimated to be  $\sim 0.005 \text{ cm}^{-1}$ , and thus has a minor contribution to the T<sub>2</sub> linewidths.

The ac-Stark effect shifts the  $v = 0$  and  $v = 1$  energy levels due to effects of the polarizability derivative and by a smaller contribution of the polarizability anisotropy [139, 140]. Both these properties are different in ground and excited states and the resulting ac-Stark coefficient for H<sub>2</sub> are found:  $\Delta\alpha = 20 \text{ MHz per GW/cm}^2$  for the polarizability derivative and  $\Delta\gamma = 9 \text{ MHz per GW/cm}^2$  for the polarizability anisotropy. Since this property is different in the ground- and excited state, a shift of the resulting Raman lines appears. Dyer and Bischel [141] showed that the experimentally determined ac-Stark shifts are in perfect agreement with *ab initio* calculated polarizabilities and that the ac-Stark effect for hydrogen always leads to a red-shift of the Raman line. Using the formulas of Dyer and Bischel with polarizability values for T<sub>2</sub> by Schwartz and Le Roy [127], one obtains a shift which is 40% smaller than that of H<sub>2</sub>. When calculating the expected shift for a CARS signal with typical pulses (pump/probe pulse energy  $E = 10 \text{ mJ}$ , pulse duration  $\tau = 8 \text{ ns}$ , beam diameter in focus  $d_{\text{focus}} = 35 \text{ }\mu\text{m}$ ) we should expect a shift of about  $0.1 \text{ cm}^{-1}$ . A shift like this should have been visible in Fig. 4.3. The effect on our spectrum is less a shift, but more a broadening towards the red (lower wavenumber) side of the CARS resonance. This observation may be ascribed to a difference in our CARS experiment as compared to the dedicated setup by Dyer and Bischel with a well-controlled auxiliary laser for quantifying the ac-Stark effect. In our approach temporal and spatial integration over the power densities has to be considered for the quantitative assessment of

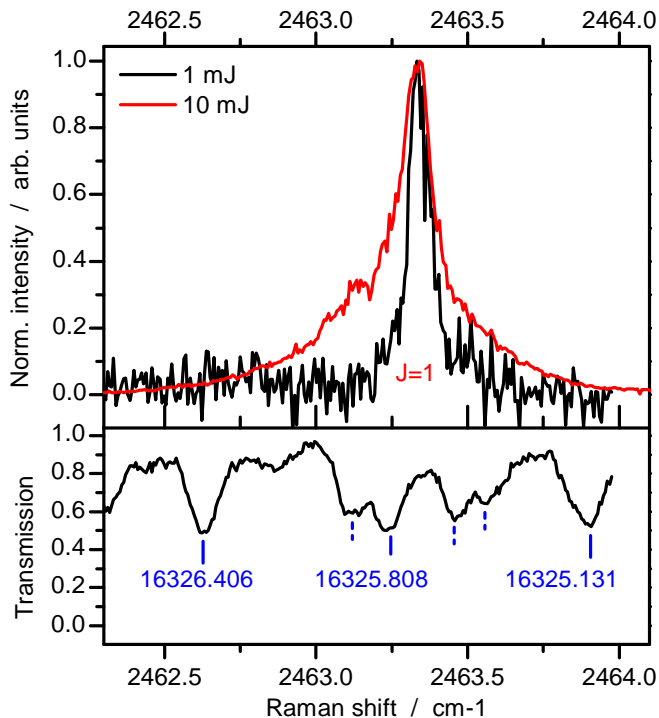


**Figure 4.3** Top:  $Q(1)$  transition recorded at 1 and 10 mJ for the pump and probe beams. Bottom: Transmission through  $I_2$  calibration cell. Blue lines indicate  $I_2$  absorption lines which have been included in the calibration of the tuneable probe laser (in  $\text{cm}^{-1}$ ). Note, that the wavenumber axis of the iodine spectrum is given by the wavenumber of the pump ( $18789.0302(10) \text{ cm}^{-1}$ ) - Raman shift.

the ac-Stark phenomenon, leading to the observed red-side broadening as demonstrated by Li, Yang and Johnson [76]. As we measured the line profiles for energies for 1 to 10 mJ while accounting for the asymmetric broadening, we did not observe a shift above the uncertainty of the probe laser calibration of  $0.01 \text{ cm}^{-1}$ .

May et al. [142] developed a model for the collisional shift in  $H_2$  as a function of pressure. They measured the linear shift coefficient of the Q-branch to be about  $\sim 0.003 \text{ cm}^{-1}/\text{amagat}$  at room temperature (See also Rahn et al. [143]). They predicted that the shift is proportional to the fundamental

vibrational transition  $\omega_e$  and thus to the inverse square root of the reduced mass ( $\propto \mu^{-1/2}$ ) - a behavior which has been verified by Looi et al. [144] when comparing shifts in  $D_2$  and  $H_2$ . Therefore, the linear shift coefficient in  $T_2$  is expected to be about 1.7 smaller as compared to that of  $H_2$ . At a pressure of 2.5 mbar, we estimate the collision shift to be negligible ( $< 1 \times 10^{-5} \text{ cm}^{-1}$ ).

The accuracy of the present line position determination is then limited by the line fitting uncertainty and by the Doppler-broadened  $I_2$  calibration reference. We provide a conservative estimate of  $0.02 \text{ cm}^{-1}$  for the transitions measured. Multiple measurements of the  $Q(1)$  transition demonstrate reproducibility of the line positions to within  $0.01 \text{ cm}^{-1}$  at the highest pulse energy of 10 mJ, at lower pulse energies the reproducibility increases.

The fitted line positions of the  $Q$  transitions are listed in Table 4.1. The transition values from the previous determination of Veirs and Rosenblatt [125], as well as the calculations of Schwartz and LeRoy [127] and by Pachucki and Komasa [52] are also included in the table. There is good agreement with the previous experimental values of Ref. [125], with the present results representing a fivefold improvement. The calculation of Schwartz and LeRoy [127] include early estimates of the relativistic and radiative corrections to the potentials, where they estimate a  $0.01 \text{ cm}^{-1}$  contribution to the level energies. They also evaluate the nonadiabatic corrections by an isotopic scaling procedure and estimate a total uncertainty of  $0.015 \text{ cm}^{-1}$  for the level energies of low rotational  $J$  states. The calculations of Pachucki and Komasa [52] only dealt with nonrelativistic contributions including nonadiabatic corrections for which they assign an uncertainty of  $10^{-7} \text{ cm}^{-1}$ , which is effectively exact for our purpose. Although Ref. [52] does not include relativistic and radiative (QED) contributions, good agreement is found with the present results. This suggests that relativistic and QED corrections are below the present experimental uncertainty of  $0.02 \text{ cm}^{-1}$ . Since the corresponding relativistic and QED corrections for  $Q$  transitions is  $\sim 0.002 \text{ cm}^{-1}$  in  $D_2$  [10], the present agreement with Ref. [52] is reasonable as it is expected that the analogous corrections are less for  $T_2$ . It is worth noting that the calculation by Schwartz and Le Roy [127] agrees to within  $0.004 \text{ cm}^{-1}$  when compared to Ref. [52].

The previous measurements of Edwards, Long and Mansour [123] deviate by  $-0.2 \text{ cm}^{-1}$  in comparison to the present results on average, despite their claimed accuracy of  $0.005 \text{ cm}^{-1}$ . As the same disagreement persists when comparing Ref. [123] with the experimental results of Veirs and Rosen-

## Conclusion

**Table 4.1** Transition energies of the Q-branch in the fundamental band ( $v = 0 \rightarrow 1$ ) of  $T_2$  extracted from measurement with lowest possible pump/probe pulse energies at sufficient high signal-to-noise ratio ( $J = 0, 1, 2, 3, 5$ : 5 mJ;  $J = 4$ : 7.5 mJ). The present results are compared to the previous experimental determination in Ref. [125] as well as calculations in Ref. [52, 127]. See text for the discussion of uncertainties in the *ab initio* calculations. The energies are given in  $\text{cm}^{-1}$ .

$J$	this work	Ref. [125]	Ref. [127]	Ref. [52]
0	2464.50 (2)		2464.498 (10)	2464.502
1	2463.33 (2)		2463.343 (10)	2463.346
2	2461.01 (2)	2461.0 (1)	2461.034 (10)	2461.037
3	2457.57 (2)	2457.5 (1)	2457.575 (10)	2457.579
4	2452.97 (2)	2452.0 (1)	2452.976 (10)	2452.980
5	2447.23 (2)	2447.3 (1)	2447.245 (10)	2447.249

blatt [125], we believe that determinations of Edwards, Long and Mansour [123] may have unrecognized systematic errors.

## 4.4 Conclusion

We have determined the transition energies of the Q(0)–Q(5) lines in the fundamental band ( $v = 0 \rightarrow 1$ ) of the ground electronic state of molecular tritium by employing CARS spectroscopy. The present results are in good agreement with Veirs and Rosenblatt [125] and represent a five-fold improvement over their previous experimental determination. Agreement with the most accurate nonrelativistic calculation [52] implies that relativistic and radiative effects for these transitions are below the present accuracy of  $0.02 \text{ cm}^{-1}$ , but may manifest in planned measurements using a narrowband probe laser source. Our present results on  $T_2$ , with the addition of spectroscopies on tritiated species HT and DT, expand our ongoing program on testing the most accurate quantum chemical theory.

We thank Tobias Falke, David Hillesheimer, Stefan Welte and Jürgen Wendel of the Tritium Laboratory Karlsruhe for the welding of the cell, preparation of the tritium gas, the filling of the cell and the legal support for the cell transport. WU thanks the European Research Council for an ERC-Advanced grant (No 670168). The research leading to these results has received funding

#### 4 CARS spectroscopy of the ( $v = 0 \rightarrow 1$ ) band in T<sub>2</sub>

from LASERLAB-EUROPE (grant agreement no. 654148, European Union's Horizon 2020 research and innovation programme).

---

## Relativistic and QED effects in the fundamental vibration of $T_2$

### Abstract

The hydrogen molecule has become a test ground for quantum electrodynamical calculations in molecules. Expanding beyond studies on stable hydrogenic species to the heavier radioactive tritium-bearing molecules, we report on a measurement of the fundamental  $T_2$  vibrational splitting ( $v = 0 \rightarrow 1$ ) for  $J = 0-5$  rotational levels. Precision frequency metrology is performed with high-resolution coherent anti-Stokes Raman spectroscopy at an experimental uncertainty of 10–12 MHz, where sub-Doppler saturation features are exploited for the strongest transition. The achieved accuracy corresponds to a fifty-fold improvement over a previous measurement, and allows for the extraction of relativistic and QED contributions to  $T_2$  transition energies.

## 5.1 Introduction

Molecular hydrogen is a quintessential system in the development of quantum chemistry and has emerged as a benchmark for testing relativistic quantum electrodynamics (QED) in simple bound systems. The accurate measurement of the dissociation energy of the H<sub>2</sub> molecule [22], the measurement of its fundamental vibrational splitting [24], as well as the accurate frequency calibration of very weak quadrupole overtone transitions [27, 145, 146] have been accompanied by ever increasing first principles calculations [4, 8, 10]. The comparisons between accurate theoretical and experimental values have spurred interpretations in fundamental physics, such as contributions from hypothetical fifth forces in the binding of the molecule [29] as well as constraining the compactification lengths of extra dimensions [56]. The various contributions to the binding energies in the hydrogen molecule, in particular the adiabatic and nonadiabatic corrections [52] to the Born-Oppenheimer energies, and to a more subtle extent the relativistic and QED contributions [84], depend on the masses of the nuclei. The mass-dependency of the corrections are accentuated in the lightest hydrogenic molecular system, and spectroscopic precision tests were extended to other hydrogen isotopologues. Measurements of the dissociation energy [120] and the quadrupole infrared spectrum [116, 118] were extended to the D<sub>2</sub> isotopologue, while the mixed HD stable isotopomer was targeted in studies of the dissociation limit [121] and the near infrared spectrum [117]. For performing comparisons with QED calculations the latter were performed for HD as well to high accuracy [147].

In contrast, there is a paucity of high-accuracy investigations on the radioactive tritium-bearing species of molecular hydrogen, such that relativistic and QED effects are entirely untested for the tritiated isotopologues. Tritium, containing two neutrons in addition to the charge-carrying proton, is unstable with a half-life of about 12 years and undergoes beta decay as the nucleus transmutes from <sup>3</sup>H to <sup>3</sup>He. Handling tritium in a typical spectroscopy laboratory is heavily restricted to dilute amounts, thus ruling out the use of molecular beam techniques, while cavity-enhanced techniques face severe difficulty in material degradation with tritium exposure. Examples of the few gas-phase experiments on T-bearing hydrogen molecules include spontaneous Raman spectroscopy on T<sub>2</sub> [123, 125] and optoacoustic spectroscopy of the fundamental and overtone bands in HT [126], performed with sample pressures of a few hundred mbars. Here, we perform precision

## Experimental setup

tests on  $T_2$ , the heaviest molecular hydrogen species, by employing Coherent Anti-Stokes Raman Spectroscopy (CARS). CARS offers excellent sensitivity and has been previously applied to  $H_2$  at 100 mbar [148], while a related Raman technique has been applied to  $D_2$  at 2-mbar pressures [149]. We have recently demonstrated the feasibility of precision measurements in a gas cell containing  $T_2$  at 2.5 mbars [36]. In this letter, we present results with a fifty-fold increase in precision, obtained by the use of a narrowband Stokes laser source and improved absolute frequency calibrations. The application of ns-pulsed narrowband laser sources on the low-pressure  $T_2$  sample has enabled the observation of narrow sub-Doppler saturation features in the CARS spectra, which is exploited to obtain higher precision for the strongest transition. Significant enhancement in the detection efficiency also allowed for the use of much lower laser intensities, leading to a more accurate treatment of AC-Stark effects.

## 5.2 Experimental setup

A schematic representation of the experimental setup is shown in Fig. 5.1. Two nearly Fourier-transform (FT) limited laser pulses for the pump ( $\omega_p$ ,  $\lambda = 532$  nm) and Stokes ( $\omega_s$ ,  $\lambda = 612$  nm) beams are temporally and spatially overlapped and focused with a  $f = 20$ -cm lens (L1) in the tritium gas cell. The nonlinear frequency mixing (scheme represented in the lower left corner of Fig. 5.1) produces an anti-Stokes coherent beam at  $\omega_{AS} = 2\omega_p - \omega_s$  corresponding to  $\lambda = 470$  nm, which is collimated (L2:  $f = 10$  cm) and dispersed using prisms, passed through an optical filter (IF) and finally detected using a photomultiplier tube (PMT). The pump beam (pulse width: 8 ns; FT-limit: 55 MHz) is the output of an injection-seeded and frequency-doubled Nd:YAG laser, while the Stokes radiation (pulse width: 6 ns; FT-limit: 74 MHz) is produced using a narrowband pulsed dye amplifier (PDA) system [150], which is seeded by a continuous-wave (cw) ring dye laser and pumped by a different injection-seeded Nd:YAG laser. The  $4\text{-cm}^3$  gas cell contains 2.5 mbar of mixed molecular hydrogen isotopologues with 93%  $T_2$ , prepared at the Tritium Laboratory Karlsruhe and transported to LaserLaB Amsterdam [36].

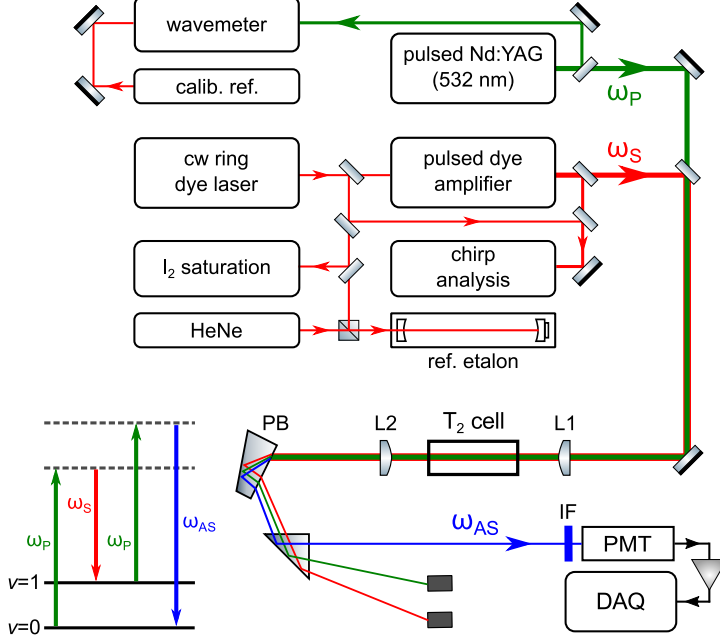


**Figure 5.1** (Color online.) Schematic of the high-resolution CARS setup. Narrow-band pump ( $\omega_p$ ) and Stokes ( $\omega_s$ ) laser beams are collinearly aligned in a sample cell containing 2.5 mbar of  $T_2$ . The generated anti-Stokes ( $\omega_{AS}$ ) radiation is spatially dispersed using prisms, passed through an optical interference filter (IF), detected using a photomultiplier tube (PMT) and recorded (DAQ). A diagram for the CARS frequency-mixing process is shown on the lower left.

### 5.3 Frequency calibration of CARS spectra

High-resolution CARS spectra are recorded for six  $Q(J)$  rotational lines (for  $J = 0 - 5$ ) of the  $X^1\Sigma_g^+$  fundamental ( $v = 0 \rightarrow 1$ ) vibrational band. A typical recording of the  $Q(0)$  Raman transition, which is the weakest among the detected lines, is shown in Fig. 5.2. The cw-seed frequency for the  $\omega_s$  radiation is calibrated in scanning mode using transmission markers of a HeNe-stabilized etalon (free spectral range  $\nu_{FSR} = 150.33(1)$  MHz) in combination with a reference spectrum provided from saturation  $I_2$  spectroscopy [65]. A temporal and spatial cw-pulse frequency offset may be induced by intensity-dependent frequency chirp effects in the pulsed-dye amplification [150–152],

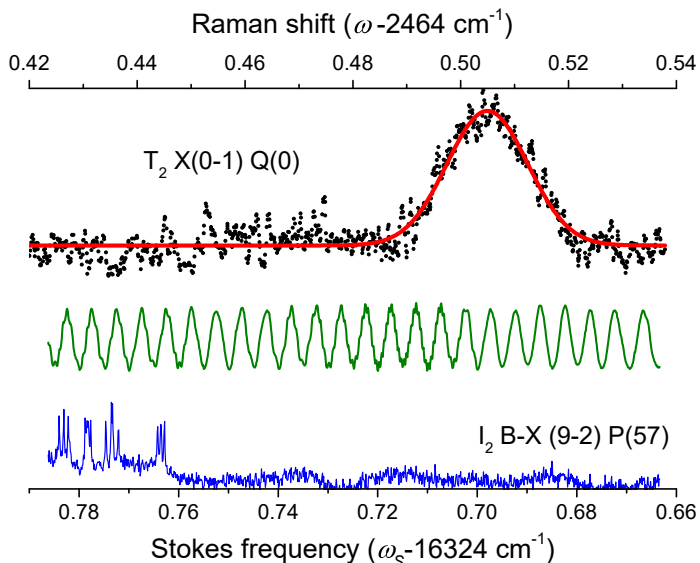


**Figure 5.2** (Color online.) Spectral recording of the Q(0) line of the  $X^1\Sigma_g^+(0-1)$  Raman band, probed at peak intensities of  $9 \text{ GW/cm}^2$  for both lasers, and plotted with respect to the Stokes frequency  $\omega_S$  (lower frequency axis) and the Raman shift  $\omega$  (upper axis). The solid red line through the  $T_2$  data points is a Gaussian fit, while the transmission of the stabilized etalon and saturated  $I_2$  spectrum are plotted below the spectrum for the relative and absolute frequency calibrations for  $\omega_S$ , respectively.

which is measured and corrected for in the data analysis [34]. The frequency of the  $\omega_p$  pulse is monitored online using a high-resolution wavemeter (High Finesse Ångstrom WSU-30) that is periodically calibrated against several absolute frequency standards in our laboratory, including calibrations against a Cs standard via an optical frequency comb laser. The Raman shift  $\omega$  is deduced from the simultaneous frequency calibration of both incident lasers at frequencies  $\omega_p$  and  $\omega_S$ , respectively.

#### 5.4 AC-Stark effect

The spectral lines are typically broadened by the AC-Stark effect as shown in Fig. 5.3, depending on the pulse intensities of the incident pump  $I_p$  and

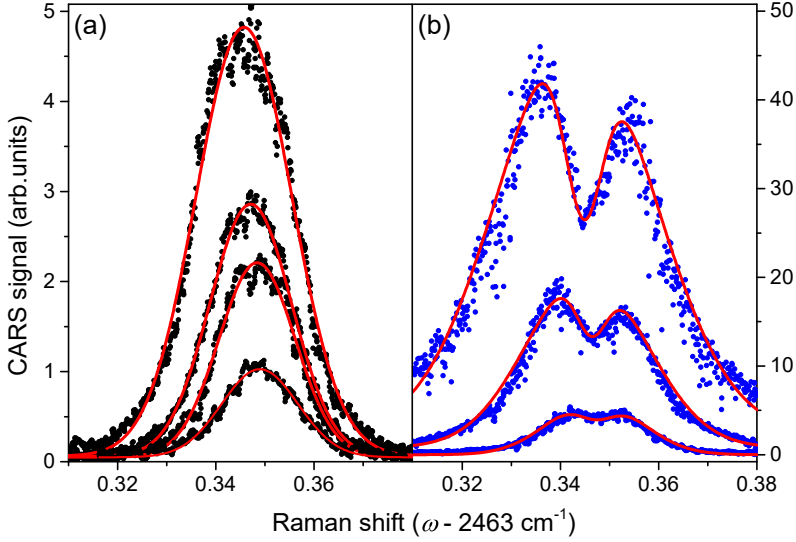


**Figure 5.3** (Color online.) Recorded CARS spectra of the Q(1) line profiles at various  $\omega_P$  and  $\omega_S$  laser intensities illustrating the AC-Stark effect. (a) At low intensities, symmetric profiles are observed that approach towards the instrument- and Doppler-limited bandwidth, with the lowest intensity in (a) at  $(I_P + I_S) = 6 \text{ GW/cm}^2$ . (b) At sufficiently high intensities, sub-Doppler saturation dips are observed, with the highest intensity in (b) at  $(I_P + I_S) = 125 \text{ GW/cm}^2$ . The amplitude scale is identical for both panels (a) and (b).

Stokes  $I_S$  laser beams, respectively. The smallest peak in Fig. 5.3 (a) was recorded with intensities of  $I_P = 6$  and  $I_S = 1.5 \text{ GW/cm}^2$ , and has a full-width half-maximum (FWHM) of 420 MHz. This approaches the expected linewidth limit from the convolution of the Doppler width (370 MHz) with the instrumental bandwidths of both laser beams (75 MHz). At sufficiently high pulse intensities ( $> 30 \text{ GW/cm}^2$ ), sub-Doppler CARS saturation dips [148, 149] are observed as shown in panel (b) of Fig. 5.3. These saturation profiles

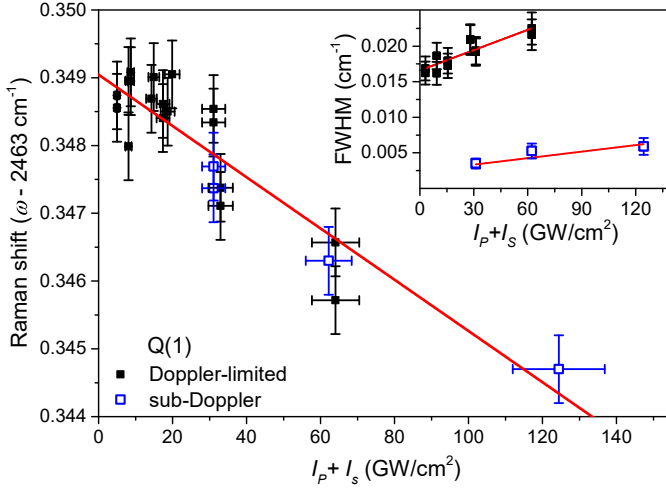


**Figure 5.4** (Color online.) Extrapolation to the field-free Raman shift for the Q(1) line measured at different intensities. The solid black squares are obtained from Doppler-broadened spectra while the unfilled blue squares are obtained from the sub-Doppler features in saturated CAR9 spectra. The red line is a fit of the combined data sets. The inset shows the FWHM linewidths, where the sub-Doppler features (solid black squares) are up to four times narrower than those for the Doppler-limited spectra (unfilled blue squares).

were fitted with the composite function,

$$y_{\text{sat}}(\omega) = A_0 + A_{\text{Dopp}} \exp \left\{ - \left( \frac{\omega - \omega_{\text{Dopp}}}{\Delta\omega_{\text{Dopp}}} \right)^2 \right\} - A_{\text{sub}} \exp \left\{ - \left( \frac{\omega - \omega_{\text{sub}}}{\Delta\omega_{\text{sub}}} \right)^2 \right\},$$

to obtain the line positions  $\omega_{(\cdot)}$ , linewidths  $\Delta\omega_{(\cdot)}$ , and amplitudes  $A_{(\cdot)}$  indicated by subscripts (Dopp) and (sub) for the Doppler-broadened profile and sub-Doppler features, respectively. The lowest intensity scan in Fig. 5.3 (b) shows a resolved sub-Doppler dip with a FWHM linewidth that is four times smaller than the Doppler-limited width and approaches the instrument bandwidth.

The AC-Stark shift for the Q(1) transition is plotted in Fig. 5.4 as a function of total intensity,  $I_p + I_s$ , of both pump and Stokes beams, respectively. Due to the similar polarizabilities at  $\lambda_p = 532$  nm and  $\lambda_s = 612$  nm for both the  $v = 0$  and  $v = 1$  levels for molecular hydrogen [141], a treatment of the AC-Stark dependence on total intensity was performed. The AC-Stark analysis includes the line centers of the Doppler-limited (unsaturated) profiles and sub-Doppler saturation dips, and the true field-free Raman line positions are obtained by extrapolating to zero total intensity. The Q(1) linewidths are plotted in the inset of Fig. 5.4 for the Doppler-limited profiles and the saturated sub-Doppler dips, showing the potential of improved line center determinations for the narrow saturation features. Due to the lower signal to noise ratio for the other Q( $J$ ) lines, sub-Doppler studies were only performed for the Q(1) transition. Collisional shifts in molecular hydrogen have been investigated in CARS studies [143] and are at the level of  $\leq 0.1$  MHz at pressures of 2.5 mbar and can be safely ignored for T<sub>2</sub>. The uncertainty contributions, summarized in Table 5.1, lead to a final uncertainty of 12 MHz or  $4 \times 10^{-4}$  cm<sup>-1</sup> for Q( $J = 0, 2 - 5$ ) lines. The slightly smaller uncertainty of 10 MHz for Q(1) reflects the use of sub-Doppler features in the AC Stark analysis, and better statistics due to more measurements performed on this line for the systematic shift assessment. The *statistics* entry in Table 5.1 indicates the reproducibility of measurements performed on different days.

**Table 5.1** Systematic and statistical contributions to the frequency uncertainties in the fundamental vibrational Raman shifts in T<sub>2</sub>. Values are given in MHz.

Contribution	Q( $J \neq 1$ )	Q(1)
Pump ( $\omega_p$ ) calibration	6	6
Stokes ( $\omega_s$ ) cw calibration	2	2
Stokes cw-pulse chirp correction	5	5
AC-Stark analysis	7	4
Collisional shift	< 1	< 1
Statistics	7	5
Combined ( $1\sigma$ )	12	10

## 5.5 Results and discussion

The  $Q(J)$  transition energies for  $J = 0-5$  are listed in the second column of Table 5.2. The present results are in agreement with our preliminary study [36], but represent a fifty-times improvement in accuracy. The measurements here are also two hundred fifty times more precise than all other previous investigations in  $T_2$ , e.g. in Ref. [125]. The  $Q(J)$  results of the present study are in agreement with the calculations in Ref. [127] with partial treatment of relativistic and radiative effects, with a claimed accuracy of  $0.02 \text{ cm}^{-1}$ . Calculations of the rotationless vibrational splitting  $Q(0)$ , which includes relativistic corrections [153] and leading-order QED estimates [18] are also consistent with the present determination to within  $0.01 \text{ cm}^{-1}$ .

**Table 5.2** Fundamental vibrational splittings of the  $Q(J)$  transitions in  $T_2$  obtained in this study are listed in the second column. Listed in the last column are the relativistic and QED energy contributions,  $E_{\text{rel+QED}}$ , to the transition energies extracted from this experiment and nonrelativistic energy  $E_{\text{nonrel}}$  calculations in Ref. [52], given in the third column. Values are given in  $\text{cm}^{-1}$ , with uncertainties in between parentheses.

line	this exp	$E_{\text{nonrel}}$ [52]	$E_{\text{rel+QED}}$
Q(0)	2 464.5052 (4)	2 464.5021	-0.0031 (4)
Q(1)	2 463.3494 (3)	2 463.3463	-0.0031 (3)
Q(2)	2 461.0388 (4)	2 461.0372	-0.0016 (4)
Q(3)	2 457.5803 (4)	2 457.5795	-0.0008 (4)
Q(4)	2 452.9817 (4)	2 452.9803	-0.0014 (4)
Q(5)	2 447.2510 (4)	2 447.2492	-0.0017 (4)

The nonrelativistic energies,  $E_{\text{nonrel}}$ , of the quantum levels in the ground electronic state are now calculated to an accuracy at the level of  $10^{-7} \text{ cm}^{-1}$  (or kHz-level) for  $H_2$ ,  $D_2$ , and  $T_2$  [4, 52]. Current efforts in first-principle calculations target higher-order relativistic and QED contributions  $E_{\text{rel+QED}}$ , including recoil corrections [4, 8, 10], and have recently been extended to the  $m\alpha^6$ -order [83]. The evaluation of mass-dependent relativistic nuclear recoil corrections currently dominate the systematic uncertainty of the *ab initio* energies [84]. However, the  $E_{\text{rel+QED}}$  contributions to the level energies of  $T_2$  have not been calculated to date. Our measurement accuracy allows for the extraction of  $E_{\text{rel+QED}}$  contributions for  $T_2$ , given in Table 5.2, with

## 5 Relativistic and QED effects in the fundamental vibration of T<sub>2</sub>

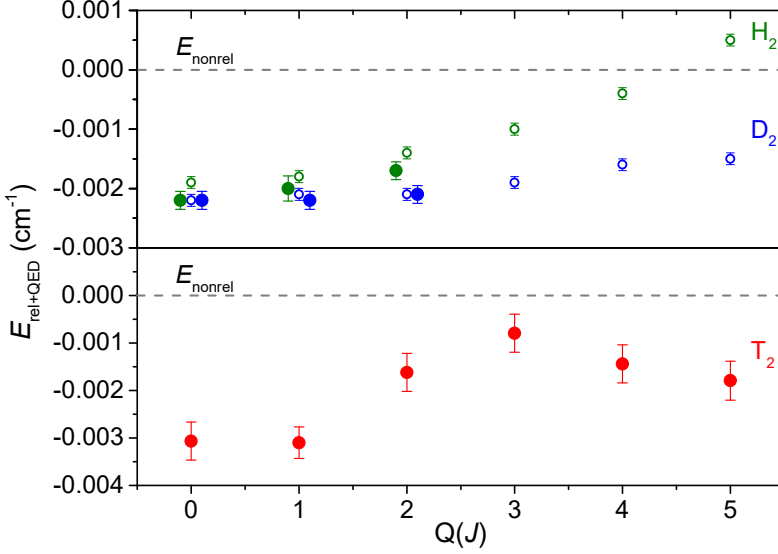


**Figure 5.5** (Color online.) Relativistic and QED contributions to T<sub>2</sub>, ( $v = 0 \rightarrow 1$ ),  $Q(J)$  transition energies, extracted from the present measurements and nonrelativistic calculations in Ref. [52], are shown in the lower panel. The analogous experimentally-derived  $E_{\text{rel+QED}}$  contributions for H<sub>2</sub> and D<sub>2</sub> from Ref. [24, 78] are shown in the upper panel, indicated by solid circles and slightly shifted horizontally for clarity. For H<sub>2</sub> and D<sub>2</sub> these can be compared to the full *ab initio* calculations [10], indicated by unfilled circles in the upper panel.

the use of nonrelativistic level energies  $E_{\text{nonrel}}$  from Ref. [52], which may be considered exact for this derivation.

The extracted  $E_{\text{rel+QED}}$  contributions for T<sub>2</sub> are plotted in the lower panel of Fig. 5.5. The analogous contributions of H<sub>2</sub> and D<sub>2</sub> using the  $Q(J = 0 - 2)$  transitions from molecular beam measurements in Refs. [24, 78] are plotted in the upper panel. These experimentally-derived H<sub>2</sub> and D<sub>2</sub>  $E_{\text{rel+QED}}$  contributions can be compared to the direct *ab initio* calculations [10], but corresponding *ab initio* calculations for T<sub>2</sub> are yet to be carried out. The relativistic and QED contributions to the T<sub>2</sub> transitions measured can be larger than those for H<sub>2</sub> and D<sub>2</sub>, presumably due to the suppression of mass-dependent higher-order terms that scale with the inverse of the reduced mass [8, 10].

## 5.6 Summary and outlook

In summary, we have determined  $Q(J = 0 - 5)$  transition energies of the fundamental band of  $T_2$  with a 50-fold improvement in precision over our preliminary study [36] and a 250-times accuracy improvement over all other previous investigations. The extracted relativistic and QED energy contributions for  $T_2$  pose a challenge to high-accuracy calculations that has yet to be pursued. Access to the tritium-bearing isotopologues ( $T_2$ , HT, DT) doubles the number of the benchmark hydrogen molecule specimens, and greatly expands opportunities for fundamental tests. Studies using the heavier tritiated species may be useful in disentangling correlations between various mass-dependent effects that currently limit the calculation uncertainty in molecular hydrogen [84]. Furthermore, comparisons of experimental and theoretical determinations of transition energies in molecular hydrogen can be used to constrain hypothetical fifth forces [29], where the heavier  $T_2$  may inherently lead to nine times enhanced sensitivity relative to  $H_2$ .

Future progress in the spectroscopy of molecular tritium holds the promise of a determination of the triton charge radius which is poorly known at present [154]. This would be of great relevance towards the resolution of the proton size puzzle [25, 51], where analogous measurements of the deuteron size [155] have been performed to shed light on the issue. Advancing our understanding of QED through spectroscopy of tritium-bearing molecular hydrogen may pave the way towards precision studies of nuclear structure.

We would like to acknowledge Meissa Diouf, Adonis Flores and Cunfeng Cheng for assistance during the measurements, and Rob Kortekaas for technical support. We thank Tobias Falke, David Hillesheimer, Stefan Welte and Jürgen Wendel of TLK for the preparation and handling of the tritium cell. WU thanks the European Research Council for an ERC-Advanced grant (No 670168). The research leading to these results has received funding from LASERLAB-EUROPE (grant agreement no. 654148, European Union's Horizon 2020 research and innovation programme).



---

## Perturbations in the $A^1\Pi, v = 0$ state of $^{12}\text{C}^{18}\text{O}$ investigated via complementary spectroscopic techniques

### Abstract

The  $A^1\Pi(v = 0)$  level of  $^{12}\text{C}^{18}\text{O}$  has been reinvestigated using three different high-resolution spectroscopic methods: (i)  $2 + 1'$  resonance enhanced multiphoton ionization of the  $A^1\Pi - X^1\Sigma^+(0, 0)$  band using narrowband lasers in a Doppler-free geometry; (ii) Fourier-transform emission spectroscopy in the visible range probing the  $B^1\Sigma^+ - A^1\Pi(0, 0)$  band in a discharge; (iii) Fourier-transform absorption spectroscopy in the vacuum-ultraviolet range measuring the  $A^1\Pi - X^1\Sigma^+(0, 0)$  and  $B^1\Sigma^+ - X^1\Sigma^+(0, 0)$  bands at multiple temperatures ranging from 90 to 900 K. An effective-Hamiltonian analysis of  $A^1\Pi, v = 0$  levels was performed up to  $J = 44$  which quantitatively addresses perturbations by the  $e^3\Sigma^-(v = 1)$ ,  $d^3\Delta(v = 4)$ ,  $a^3\Sigma^+(v = 9)$ ,  $D^1\Delta(v = 0)$ , and  $I^1\Sigma^-(v = 0, 1)$  levels.

## 6.1 Introduction

Spectroscopy of the carbon monoxide molecule and, in particular, its pronounced 4<sup>th</sup>-positive or  $A^1\Pi - X^1\Sigma^+$  system has been investigated repeatedly since the 1920s, beginning with Birge [156] and Herzberg [157]. It is a benchmark system for analyzing perturbations in diatomic molecules. A comprehensive theoretical framework for such analysis of perturbations in the  $A^1\Pi$  state was developed by Field *et al.* [158, 159]. The  $A^1\Pi$  state of the specific  $^{12}\text{C}^{18}\text{O}$  isotopomer has been investigated via emission spectroscopy of the  $B^1\Sigma^+ \rightarrow A^1\Pi$  Ångström bands [160, 161], the  $C^1\Sigma^+ \rightarrow A^1\Pi$  Herzberg bands [162], and the  $E^1\Pi \rightarrow A^1\Pi$  Keça - Rytel system [163, 164], and in absorption via the  $A^1\Pi \leftarrow X^1\Sigma^+$  system using vacuum-ultraviolet (VUV) absorption [165–167]. These experiments reveal multiple non-Born-Oppenheimer interactions of the  $A^1\Pi$  state with several other states, which do not themselves readily appear in experimental spectra:  $d^3\Delta$ ,  $e^3\Sigma^-$ ,  $a^3\Sigma^+$ ,  $D^1\Delta$ , and  $I^1\Sigma^-$ . Previously, Beaty *et al.* [167] used their high-resolution  $A^1\Pi \rightarrow X^1\Sigma^+$  emission spectra to model the interaction of the  $A^1\Pi(v = 0 - 9)$  levels with these states and deduced deperturbed molecular constants. VUV-laser excitation studies on the  $A^1\Pi \rightarrow X^1\Sigma^+$  system for  $^{12}\text{C}^{18}\text{O}$  have been performed as well [168, 169].

Other spectroscopic studies involving  $^{12}\text{C}^{18}\text{O}$  have focused on the  $B^1\Sigma^+ - X^1\Sigma^+$  system [170], on transition oscillator strengths [171, 172], and on the measurement of lifetimes [173, 174]. The spectroscopy of the  $^{12}\text{C}^{18}\text{O}$  ground state has been studied to high accuracy in microwave [e.g., 175, 176] and far infrared (FIR) experiments [e.g., 177]. A comprehensive analysis was made by Coxon and Hajigeorgiou [178] leading to a very accurate model for the ground-state in CO isotopologues expressed in terms of molecular parameters.

The present investigation is one of a series analyzing perturbations in low- $v$  levels of the  $A^1\Pi$  state in detail for various isotopologues. These studies have provided a highly accurate description of the level energies and the corresponding perturbations of the  $A^1\Pi$  state in the  $^{12}\text{C}^{16}\text{O}$  main isotopologue [39, 67, 179, 180], and in the  $^{13}\text{C}^{16}\text{O}$  [40],  $^{12}\text{C}^{17}\text{O}$  [181], and  $^{13}\text{C}^{17}\text{O}$  [41] isotopologues. One goal of this work is to quantify the electronic isotope shifts in the  $A^1\Pi$  state and determine whether it shows anomalous behaviour in common with observations of the  $a^3\Pi$  state [38, 182]. The new spectroscopic

## Introduction

measurements of  $A^1\Pi(v=0)$  state presented here are necessary to obtain the precision required to probe this effect.

The general methodology of this work is similar to our recent studies of other CO isotopologues [40, 41, 181]. Three spectroscopic techniques are employed: Doppler-free two-photon laser spectroscopy of the  $A^1\Pi - X^1\Sigma^+(0,0)$  band, Fourier-transform emission spectroscopy in the visible range on the  $B^1\Sigma^+ - A^1\Pi(0,0)$  band, and Fourier-transform absorption spectroscopy in the VUV range on the  $A^1\Pi - X^1\Sigma^+(0,0)$  and  $B^1\Sigma^+ - X^1\Sigma^+(0,0)$  bands. The first technique provides transition frequencies with ultrahigh accuracy and the latter two provide high-resolution broadband measurements. These independent measurements of the level energy separations for all combinations of  $X^1\Sigma^+(v=0)$ ,  $A^1\Pi(v=0)$ , and  $B^1\Sigma^+(v=0)$  levels provide a check on the absolute frequency uncertainties estimated for each experiment.

Based on this variety of complementary spectroscopic experiments, accurate level energies are determined for the rotational levels of  $A^1\Pi(v=0)$  and  $B^1\Sigma^+(v=0)$  and some levels in the perturbing  $d^3\Delta(v=4)$ ,  $e^3\Sigma^-(v=1)$ , and  $a'^3\Sigma^+(v=9)$  states. None of the latter states support allowed transitions in our spectra due to spin and orbital angular momentum selection rules, but appear due to their spin-orbit and rotational-electronic ( $L$ -uncoupling) interactions with  $A^1\Pi(v=0)$ . An effective Hamiltonian is used to model the level structures and to determine deperturbed molecular constants for each of the states. Mutual interactions, as well as interactions with some more remote levels are included in the Hamiltonian matrix, leading to an accurate reproduction of the measured level energies to within experimental accuracy.

Hereafter, we abbreviate vibrational levels and transitions, for example,  $A^1\Pi(v=0)$  and  $B^1\Sigma^+ - X^1\Sigma^+(v'=0, v''=0)$  to  $A(0)$  and  $B-A(0,0)$ . Rotational branches for transitions involving triplet states are labelled in the tables, presented in this paper, as, e.g.,  $Q_{21fe}$ , indicating a  $\Delta J = 0$  transition with an upper-state  $f$ -symmetry  $F_2$  level and lower-state  $e$ -symmetry  $F_1$  level. The important cases are the  $d^3\Delta$  and  $e^3\Sigma^-$  states for which the  $F_1$ ,  $F_2$ , and  $F_3$  rotational stacks correspond to Hund's case (a) levels with  $J = N - 1$ ,  $N$ , and  $N + 1$ , respectively. There exist  $e$ - and  $f$ -symmetry versions of all  $F_i$  levels of  $d^3\Delta$  whereas  $e^3\Sigma^-$  is restricted to the pairs  $(F_1, e)$ ,  $(F_2, f)$ , and  $(F_3, e)$ .

## 6.2 $2 + 1'$ REMPI laser spectroscopy

### 6.2.1 Experimental details

A narrowband tunable pulsed dye amplifier laser system at LaserLaB Amsterdam [183] was used in a molecular beam study. Doppler-free spectra of the A-X(0,0) band of  $^{12}\text{C}^{18}\text{O}$  were recorded using counter-propagating laser beams of ultraviolet (UV) radiation perpendicularly crossing a molecular beam of  $^{18}\text{O}$  isotopically-enriched carbon monoxide (Sigma Aldrich, 99.9%  $^{12}\text{C}$  and 95%  $^{18}\text{O}$ ). The excited molecules were ionized by a second pulse-time-delayed laser at 202 nm, forming a  $2 + 1'$  resonance enhanced multiphoton ionisation (REMPI) process. Signal detection was established by monitoring 30 amu ions in a time-of-flight mass spectrometer. An accurate frequency calibration was performed by simultaneously measuring a saturated absorption spectrum of molecular iodine with reference to pre-calibrated  $\text{I}_2$  resonances [65] and a stabilized etalon, as was done in previous experiments with other CO isotopologues [67, 180]. The measured transition frequencies of the two-photon resonances were corrected for frequency chirp effects in the pulsed dye amplifier [67, 183, 184] and extrapolated to zero intensity to correct for AC Stark effects [39]. These procedures yielded two-photon transition frequencies with an accuracy of  $0.001 \text{ cm}^{-1}$ , which corresponds to 30 MHz. This error estimate is composed of contributions from frequency chirp, absolute frequency calibration, and the AC-Stark extrapolation, in order of importance.

### 6.2.2 Results

Figure 6.1 shows a recording of the R(2) two-photon transition in the A-X(0,0) band of  $^{12}\text{C}^{18}\text{O}$ . The  $\text{I}_2$  saturation spectrum used for absolute calibration and the transmission intensity from the stabilized etalon are also shown. The latter exhibits a low finesse at the wavelength of the fundamental,  $\lambda = 617 \text{ nm}$ , but after fitting a sine function through the markers this does not contribute significantly to the calibration uncertainty. In the  $^{12}\text{C}^{18}\text{O}$  molecular beam expansion only the lowest  $J$ -values can be probed due to rotational cooling. Accurate transition frequencies were measured for 10 lines in the two-photon spectrum and their results are listed in Table 6.1.

After the laser spectroscopic measurements on  $^{12}\text{C}^{18}\text{O}$ , a separate measurement was performed to correct for the chirp phenomenon [67]. Typi-

## 2 + 1' REMPI laser spectroscopy

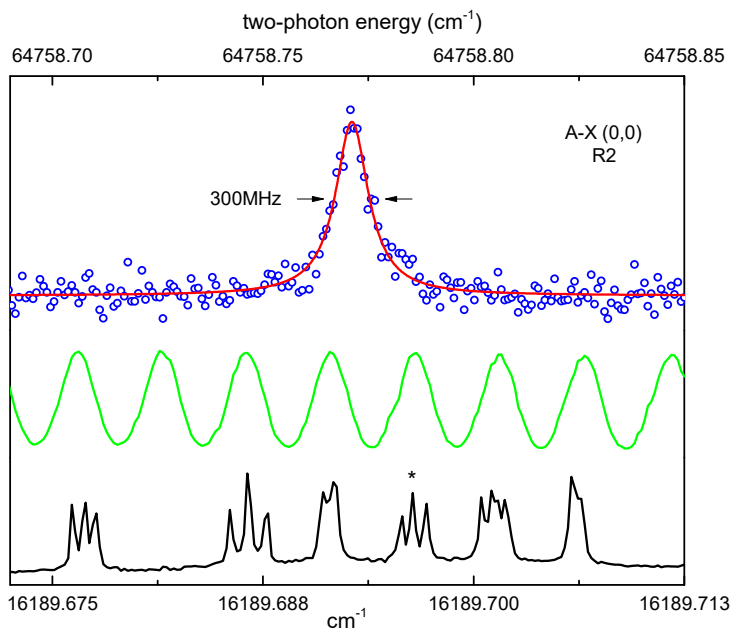


**Figure 6.1** Recording of the R(2) two-photon transition in the  $A^1\Pi - X^1\Sigma^+(0,0)$  band of  $^{12}\text{C}^{18}\text{O}$  measured by 2 + 1' REMPI (red points and fitted black curve). The lower blue and black lines represent etalon markers and the saturated absorption spectrum of  $\text{I}_2$  used for frequency interpolation and calibration. The asterisk indicates the a13 (7,7) hyperfine component of the B-X (10,3) R(81) iodine line at  $16189.69559 \text{ cm}^{-1}$  [65] that was used for calibration.

cal values for the chirp-induced shift were  $-18(5)$  MHz at the fundamental frequency. Even after quantitative assessment of this contribution to the systematic frequency shift it remains the major source of uncertainty in the error budget for frequencies listed in Table 6.1.

The transition frequencies of all lines were measured under various intensities of the laser field, providing information for making AC-Stark plots. These are shown in Fig. 6.2 for four lines plotted  $\hat{\nu}$  against an absolute scale of laser intensity in the focal region. The uncertainty of the absolute intensity value may be as large as 25%, the relative intensities are accurate within 10%, allowing for an extrapolation to zero intensity to obtain an AC-Stark-

**Table 6.1** Rotational transition frequencies,<sup>1</sup>  $\nu_{obs}$ , the deviations between observed values and calculated values from a fit to the entire data set involving all laser, FT-emission and FT-absorption lines  $\Delta_{obs.-calc.}$ , and AC-Stark slope coefficient<sup>2</sup>,  $C_{AC}$ , of  $A^1\Pi - X^1\Sigma^+(0,0)$  in  $^{12}\text{C}^{18}\text{O}$  as measured in the  $2 + 1'$  REMPI laser experiment.

Line	$\nu_{obs}$	$\Delta_{obs.-calc.}$	$C_{AC}$
P(2)	64 743.6807 (10)	-0.0022	0.45
P(3)	64 738.7324 (10)	0.0001	0.33
P(4)	64 733.1271 (10)	-0.0007	0.44
Q(1)	64 750.9905 (20)	0.0006	
Q(2)	64 749.6591 (10)	-0.0021	0.37
Q(3)	64 747.6367 (20)	-0.0016	
R(1)	64 757.0383 (10)	-0.0031	0.34
R(2)	64 758.7614 (10)	0.0019	0.43
S(0)	64 760.6457 (10)	-0.0011	0.40
S(1)	64 765.9457 (10)	-0.0016	0.43

<sup>1</sup> Units of  $\text{cm}^{-1}$  and  $1\sigma$  uncertainties given in parentheses in units of the least-significant digit)

<sup>2</sup> Units of  $\text{MHz}/(\text{MW}/\text{cm}^2)$ .

free transition frequency. The values listed in Table 6.1 include such an extrapolation. An AC-Stark slope parameter  $C_{AC}$  was also determined for most lines, representing the proportionality between the laser intensity in units of  $\text{MW}/\text{cm}^2$  and the AC-Stark induced line shift. For the Q(1) and Q(3) lines only indicative values for the slopes were measured. On average a value of  $C_{AC} = 0.41(10)$  is found for the two-photon lines in the A-X(0,0) band of  $^{12}\text{C}^{18}\text{O}$ . This value falls within a factor of two of that found in an early high-power study of the AC-Stark effect in CO [72]. Results on dynamic polarizabilities may provide information on the structure and internal dynamics in molecules, but will not be discussed further in this paper, which focuses on high resolution spectra and perturbations in the excited state.

## 6.3 Fourier-transform emission in the visible range (VIS-FT)

### 6.3.1 Experimental details

Visible (VIS) wavelength emission spectra of  $^{12}\text{C}^{18}\text{O}$  were recorded at the University of Rzeszów using an air-cooled, carbon hollow-cathode (HC) lamp operated at 780 V, 54 mA dc. The lamp was filled with a static mixture of

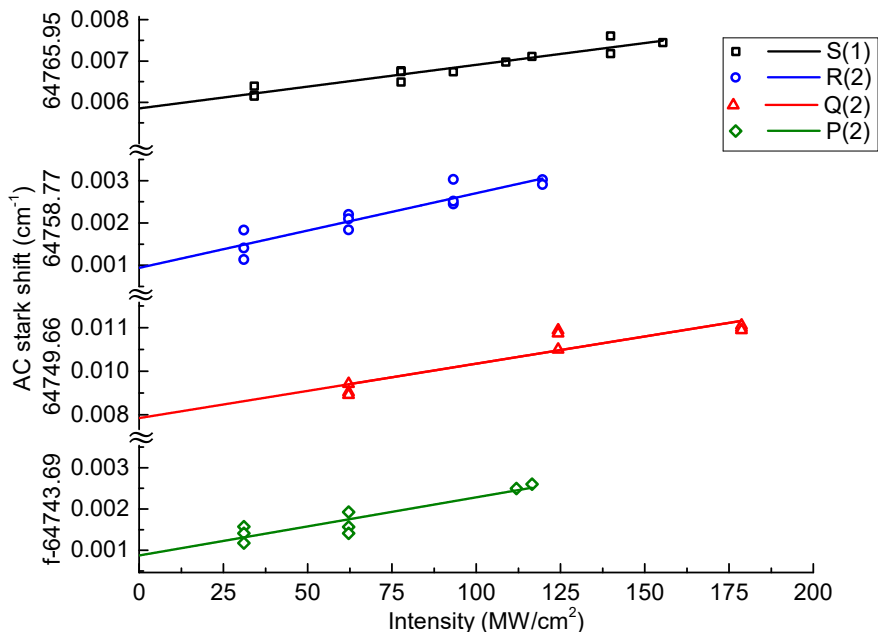


**Figure 6.2** AC-Stark-plots for four transitions measured by two-photon Doppler-free spectroscopy in the  $A^1\Pi - X^1\Sigma^+(0,0)$  band of  $^{12}\text{C}^{18}\text{O}$ .

$^{18}\text{O}_2$  and  $^{16}\text{O}_2$  (Sigma-Aldrich, 98.1%  $^{18}\text{O}_2$ ) at a pressure of 3 mbar. During the discharge process, the  $\text{O}_2$  molecules react with the  $^{12}\text{C}$  atoms ejected from the carbon filler placed inside the cathode, thus forming  $^{12}\text{C}^{18}\text{O}$  and  $^{12}\text{C}^{16}\text{O}$  molecules in the gas phase, in sufficient amounts to achieve a signal-to-noise ratio (SNR) of 70 : 1 for the  $^{12}\text{C}^{18}\text{O}$  spectrum. For the current experiment, we used an improved version of the HC lamp with respect to previous investigations [185, 186]. A higher temperature dc-plasma (up to 900 K) was obtained at the center of the cathode and allowed for observations of B–A(0,0) rotational transitions with  $J$  as high as high 40. The associated line-broadening increased by only  $0.02\text{ cm}^{-1}$  relative to previous studies [187, 188], in which a dc-plasma temperature of about 650 K was used.

The discharge glow was focused by a plano-convex quartz lens onto the entrance aperture (1.0 mm diameter) of a 1.71 m Fourier-transform (FT) spec-

trometer [40, 41]. A recent modification of this spectrometer significantly reduced the reflection of the HeNe laser beam, used for calibration and control of the position of a movable retroreflecting mirror, from optical elements in the interferometer and detector compartments, and noticeably improved its sensitivity in the VIS and UV regions. A visible-wavelength quartz beam-splitter and a photomultiplier tube running in integration mode were used to record the  $^{12}\text{C}^{18}\text{O}$  B–A(0,0) spectrum between 22100 and 22900  $\text{cm}^{-1}$ . The spectrometer was operated under vacuum conditions (pressure below 0.003 mbar). Emission spectra were accumulated over 128 scans to obtain the desired SNR with a spectral resolution of 0.018  $\text{cm}^{-1}$ . Under these settings the observed widths of  $^{12}\text{C}^{18}\text{O}$  lines did not depend on the spectrometer resolution, but were limited by the Doppler broadening, yielding linewidths of 0.1  $\text{cm}^{-1}$ . The molecular gas composition used to obtain the spectrum was  $^{12}\text{C}^{18}\text{O}; ^{12}\text{C}^{16}\text{O} = 1 : 0.1$ .

The spectrum was frequency calibrated using the 633 nm line of an internal frequency-stabilized HeNe laser. The central positions of emission lines were measured by fitting Voigt lineshape functions to the experimental spectrum using a least-squares fitting procedure. The estimated absolute calibration uncertainty ( $1\sigma$ ) is 0.003  $\text{cm}^{-1}$ . The fitting uncertainty of the line frequency measurements is estimated to be 0.003  $\text{cm}^{-1}$  for single medium-strength lines and 0.01 – 0.02  $\text{cm}^{-1}$  for weak and/or blended ones.

### 6.3.2 Results

An overview of the wavelength region studied in VIS-emission (437 – 452 nm), together with rotational assignments and a simulated spectrum, is shown in Fig. 6.3. In this spectrum some  $^{12}\text{C}^{18}\text{O}$  B–A (0,0) lines are blended with  $^{12}\text{C}^{16}\text{O}$  B–A (0,0) as well as with lines from B–A (1,1) bands of  $^{12}\text{C}^{18}\text{O}$  and  $^{12}\text{C}^{16}\text{O}$ . This contamination was taken into consideration during the analysis of the spectral lines in the  $^{12}\text{C}^{18}\text{O}$  B–A (0,0) band. In total, we assigned and analysed 168 molecular emission lines of  $^{12}\text{C}^{18}\text{O}$ , among which 119 belong to B–A (0,0) band, and 49 to the so called “extra lines” associated with the  $B^1\Sigma^+ - e^3\Sigma^-(0,1)$ ,  $B^1\Sigma^+ - d^3\Delta(0,4)$  and  $B^1\Sigma^+ - a'^3\Sigma^+(0,9)$  transitions terminating on perturber states and gaining intensity from mixing with the  $A^1\Pi$  state. Wavenumbers of the  $^{12}\text{C}^{18}\text{O}$  B–A (0,0) band are listed in Table 6.2 and transition frequencies of the extra lines are presented in Table 6.3.

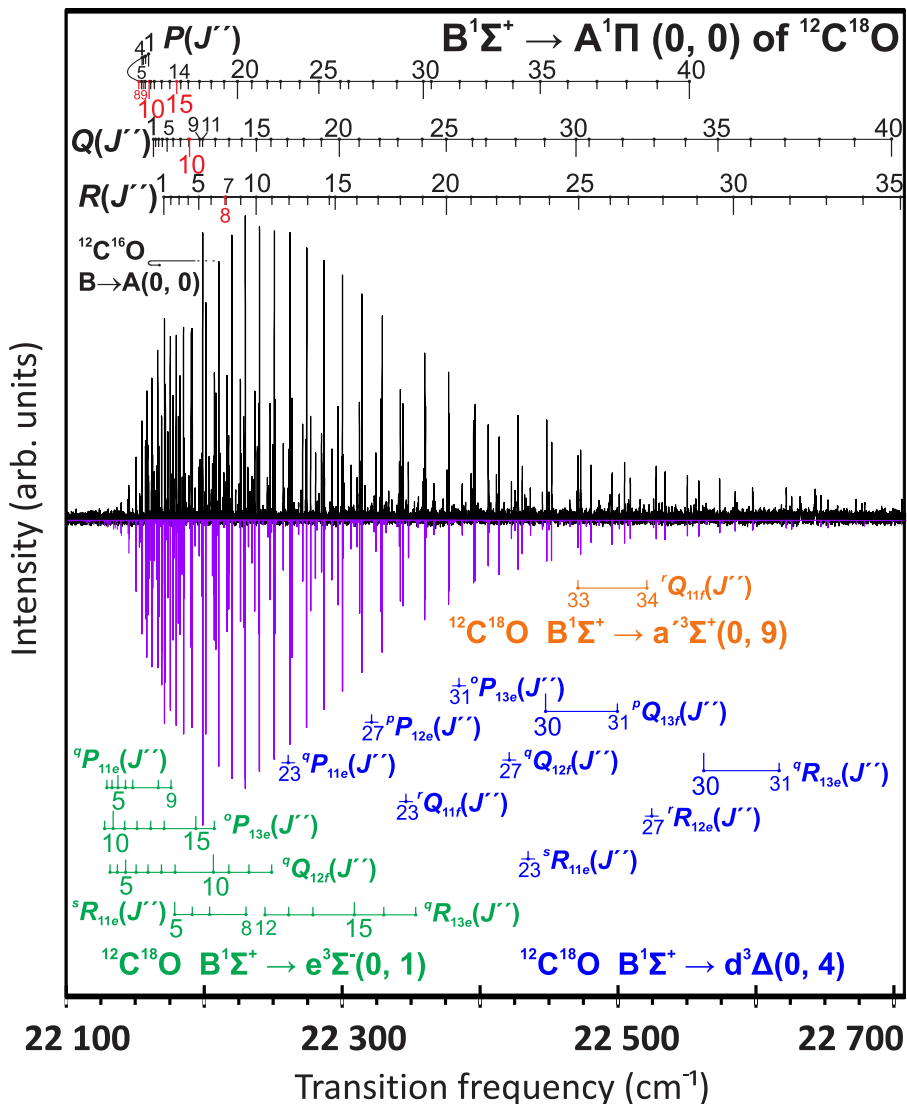


**Figure 6.3** High resolution emission spectrum with rotational assignments of the  $^{12}\text{C}^{18}\text{O}$   $B^1\Sigma^+ - A^1\Pi(0,0)$ ,  $B^1\Sigma^+ - e^3\Sigma^-(0,1)$ ,  $B^1\Sigma^+ - d^3\Delta(0,4)$ , and  $B^1\Sigma^+ - a^3\Sigma^+(0,9)$  bands recorded with the VIS-FT spectrometer. Upper trace: experimental spectrum; Lower trace: simulation of  $^{12}\text{C}^{18}\text{O}$   $B^1\Sigma^+ - A^1\Pi(0,0)$  obtained with the Pgopher software [189]. Lines indicated by red labels represent  $J$ -values with the strongest perturbations.

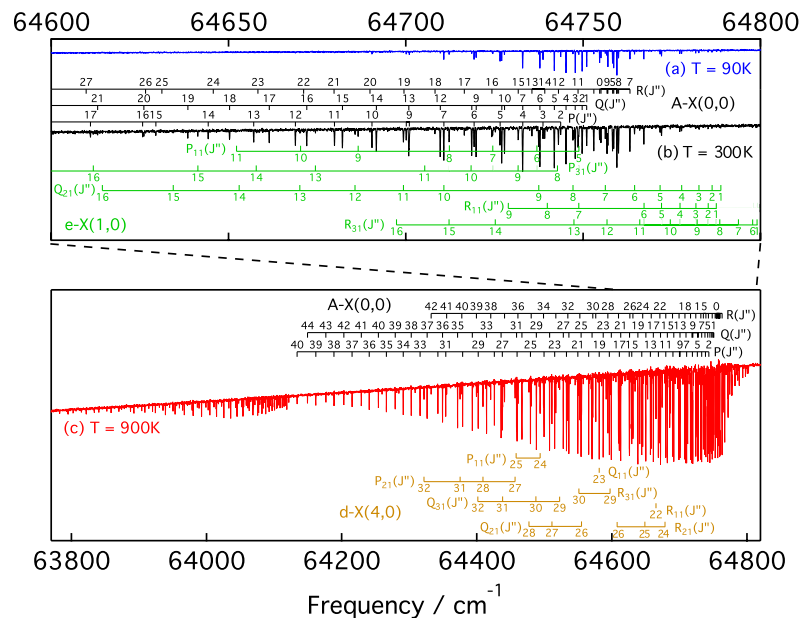


**Figure 6.4** Spectra of the A-X(0,0) band, and perturbing  $e^3\Sigma^- - X^1\Sigma^+(1,0)$  and  $d^3\Delta - X^1\Sigma^+(4,0)$  bands, recorded with the VUV-FT spectrometer at the SOLEIL synchrotron for three different sample temperatures,  $T = 90\text{ K}$ ,  $T = 300\text{ K}$  and  $T = 900\text{ K}$ , as indicated.

**Table 6.2** Transition frequencies of the  $^{12}\text{C}^{18}\text{O } B^1\Sigma^+ - A^1\Pi (0,0)$  band obtained in the VIS-FTS experiment.<sup>1</sup>

$J''$	$P$	$Q$	$R$	$J''$	$P$	$Q$	$R$
1	22 173.18 <i>wb</i>	22 165.76 <i>wb</i>	22 162.06 <i>b</i>	21	22 396.035	22 314.806	22 236.953
2	22 178.31 <i>wb</i>	22 167.13 <i>b</i>	22 159.76 <i>b</i>	22	22 414.657	22 329.714	22 248.22 <i>b</i>
3	22 184.191	22 169.21 <i>b</i>	22 158.220	23	22 431.519 *	22 342.853	22 257.736
4	22 190.86 <i>wb</i>	22 172.02 <i>b</i>	22 157.48 <i>b</i>	24	22 452.843	22 360.530 *	22 271.729
5	22 198.473	22 175.56 <i>b</i>	22 157.66 <i>b</i>	25	22 473.905	22 377.918	22 285.467 *
6	22 207.358	22 179.91 <i>b</i>	22 159.13 <i>b</i>	26	22 496.898	22 397.234	22 301.132
7	22 218.343	22 185.14 <i>b</i>	22 162.70 <i>b</i>	27	22 510.07 <i>b</i>	22 406.756	22 307.006
8	22 217.920	22 191.41 <i>b</i>	22 154.869	28	22 535.354 *	22 428.37 <i>b</i>	22 324.962
9	22 228.927	22 199.06 <i>b</i>	22 158.466	29	22 559.85 <i>wb</i>	22 449.219 *	22 342.145
10	22 240.030	22 191.563	22 162.16 <i>b</i>	30	22 586.31 <i>wb</i>	22 472.041	22 361.33 <i>b*</i>
11	22 251.629 *	22 201.330	22 166.36 <i>b</i>	31	22 599.42 <i>wb</i>	22 481.500	22 367.17 <i>wb</i>
12	22 264.02 <i>b</i>	22 210.788 *	22 171.34 <i>b</i>	32	22 627.33 <i>wb</i>	22 505.824	22 387.81 <i>wb</i>
13	22 277.546 *	22 220.305	22 177.458 *	33	22 653.81 <i>wb*</i>	22 528.868	22 407.04 <i>b</i>
14	22 293.024	22 230.131 *	22 185.559	34	22 680.43 <i>wb</i>	22 551.528 *	22 426.36 <i>w</i>
15	22 297.486	22 240.411	22 182.639 *	35	22 707.45 <i>wb</i>	22 574.959	22 446.14 <i>wb</i>
16	22 313.068	22 251.238	22 190.84 <i>b</i>	36	22 734.54 <i>wb</i>	22 598.91 <i>wb</i>	22 465.98 <i>wb</i>
17	22 328.66 <i>b</i>	22 262.659	22 199.06 <i>b</i>	37	22 762.99 <i>wb</i>	22 623.47 <i>wb</i>	22 487.27 <i>wb</i>
18	22 344.626	22 274.700	22 207.634	38	22 791.78 <i>wb</i>	22 648.67 <i>wb</i>	22 508.86 <i>bs</i>
19	22 361.130	22 287.389	22 216.770	39	22 821.20 <i>wb</i>	22 674.20 <i>wb</i>	22 531.06 <i>wb</i>
20	22 378.243	22 300.745	22 226.521	40		22 700.89 <i>wb</i>	22 553.92 <i>wb</i>

[1] In units of  $\text{cm}^{-1}$ . Lines marked with *w* and/or *b* are weak and/or blended. For lines marked by an asterisk (\*) a small perturbation in the  $B^1\Sigma^+(v=0)$  excited state was found. The instrumental resolution was  $0.018 \text{ cm}^{-1}$ . The estimated absolute calibration uncertainty ( $1\sigma$ ) is  $0.003 \text{ cm}^{-1}$ . The absolute accuracy of the line frequency measurements are estimated to be  $0.003 - 0.02 \text{ cm}^{-1}$  depending on line strength and blending.



**Table 6.3** (continued from last page) Spin-forbidden lines appearing in the VIS-FT absorption spectra.<sup>1</sup>

$J''$	${}^sR_{11ee}$	${}^rQ_{11ef}$	${}^qP_{11ee}$	${}^rR_{12ee}$	${}^qQ_{12ef}$	${}^pP_{12ee}$	${}^qR_{13ee}$	${}^pQ_{13ef}$	${}^oP_{13ee}$
	$\mathbf{B}^1\Sigma^+ - d^3\Delta (0,4)$								
23	22 437.37 $wb^*$	22 348.657	22 263.57 $wb$						
...									
27				22 526.95 $wb$	22 423.60	22 323.88 $wb$			
...									
30							22 565.14 $wb$	22 450.816	
31							22 619.97 $wb$	22 502.03 $w$	22 387.69 $b$
	$\mathbf{B}^1\Sigma^+ - a^3\Sigma^+ (0,9)$								
33		22 523.68 $wb$							
34		22 473.76 $wb^*$							

<sup>1</sup> All transition frequencies are in  $\text{cm}^{-1}$ . Lines marked with  $w$  and/or  $b$  are weak and/or blended. Lines marked with an asterisk (\*) indicate a small perturbation in the  $\mathbf{B}^1\Sigma^+(v=0)$  excited state. The branch-label subscripts  $e$  and  $f$  indicate the upper-state/lower-state symmetry and superscripts  $o, p, q, r$  and  $s$  denote change in the total angular momentum excluding spin.

## 6.4 Fourier-transform absorption in the vacuum ultraviolet (VUV-FT)

The Fourier-transform (FT) vacuum ultraviolet (VUV) spectrometer on the DESIRS beamline at the SOLEIL synchrotron was used to record spectra of the  $A-X(0,0)$  and  $B-X(0,0)$  bands of  $^{12}\text{C}^{18}\text{O}$ . Its operation and performance have already been described in detail [190, 191] as well as its application for the measurement of CO spectra [179, 180, 192].

### 6.4.1 $A^1\Pi \leftarrow X^1\Sigma^+(0,0)$

Figure 6.4 shows three absorption spectra of  $A-X(0,0)$  recorded with successively greater sample temperatures and column densities. The quasi-static CO gas was outflowing from a windowless cell under three different temperature regimes: liquid-nitrogen cooled (90 K), room temperature (300 K) and a heated cell (900 K) [193]. Doppler-broadening of the observed spectral lines increases at higher temperatures and limits the accuracy of line-center measurements. The advantage of high-temperature spectra is that more rotational states can be probed, in the present study up to  $J = 41$ . Analysis of the combined spectra permitted precise frequency measurements for strong  $A-X(0,0)$  lines and much-weaker forbidden transitions. Lines arising from the  $A-X(1,1)$  hot band are also evident in Fig. 6.4(c) between  $63\,800$  and  $64\,130\text{ cm}^{-1}$ .

The integrated cross sections of all lines were optimised to best fit the 900 K spectrum after application of the Beer-Lambert law to their Doppler broadened summation. This required consideration of the sinc-shaped instrumental broadening of the VUV-FT instrument, with a full-width half-maximum of  $0.27\text{ cm}^{-1}$  (a higher spectral resolution,  $0.07\text{ cm}^{-1}$ , was adopted while recording 90 and 300 K spectra). To improve the fitting of blended lines, the spectra were analysed while assuming combination differences of  $P$ - and  $R$ -branch transitions fixed to known ground state term values [178]. Also, no perturbations of  $A(0)$  have dipole-allowed transitions to the ground state and we assumed no intensity-interference effects afflicting  $A-X(0,0)$   $P$ - and  $R$ -branch lines with common  $J'$ , which might otherwise arise from the mixing of parallel and perpendicular transition moments [194]. Under this assumption, the relative strengths of  $P(J' + 1)$  and  $R(J' - 1)$  lines are then

given by the ratio of their Hönl-London factors and a Boltzmann distribution of ground state  $J''$  level populations [1, 195].

Linearity of the FT frequency scale is intrinsically reliable, being dictated by the macroscopic interferometrically-controlled stepping of a mirror in the wave-front-division interferometer. An absolute frequency calibration of the A–X(0,0) spectrum was obtained by comparison with our two-photon absorption laser-based measurements of low- $J$   $A^1\Pi - X^1\Sigma^+$  lines, described in Sec. 6.2. This required consideration of the parity of excited levels probed in one- and two-photon absorption because of significant  $\Lambda$ -doubling of the  $A^1\Pi$  state. The estimated accuracy of this absolute calibration is  $0.0015\text{ cm}^{-1}$ . The final list includes 126 rotational transitions of A–X(0,0), and 73 spin-forbidden lines associated with the  $e^3\Sigma^- - X^1\Sigma^+(1,0)$  and  $d^3\Delta - X^1\Sigma^+(4,0)$  bands. All measured frequencies are listed in Tables 6.4 and 6.5.

In the zero-order model, only the A–X(0,0) band provides any oscillator strength and has a  $J'/J''$ -independent band  $f$ -value when dividing by the Hönl-London factors for a  $^1\Pi - ^1\Sigma^+$  transition [1, 195]. After level mixing is considered, some transitions to d(4) and e(1) levels borrow intensity by mixing with nearby A(0) levels.

The integrated cross sections of A–X(0,0) lines were converted into band  $f$ -values by factorising their ground state populations and Hönl-London transition factors and are shown in Fig. 6.5. Band  $f$ -values will be  $J'$  independent in the absence of perturbations, whereas A–X(0,0) shows locally reduced  $f$ -values due to intensity borrowing by levels of  $d^3\Delta - X^1\Sigma^+(4,0)$  and  $e^3\Sigma^- - X^1\Sigma^+(1,0)$ . The integrated cross sections of extra lines of  $d^3\Delta - X^1\Sigma^+(4,0)$  and  $e^3\Sigma^- - X^1\Sigma^+(1,0)$  were converted into band  $f$ -values assuming Hönl-London factors for a  $^1\Pi - ^1\Sigma^+$  transition and are also shown in Fig. 6.5. The summation of transitions to all interacting levels is  $J'$  independent and represents the unperturbed A–X(0,0) band  $f$ -value. For  $P/R$  branch transitions connected to  $e$ -symmetry excited levels  $J' = 7$  and 14 the admixture of A(0) into the  $F_3$  component of e(1) is nearly 50%, indicated by the equal sharing of intensity. The  $f$ -symmetry  $J' = 10$  levels of A(0) and e(1) are similarly affected.

**Table 6.4** Transition frequencies of  $A^1\Pi - X^1\Sigma^+(0,0)$  from the VUV-FT experiment.<sup>1</sup>

$J''$	R	Q	P	$J''$	R	Q	P
0	64754.654(5)	–	–	23	64658.293(3)	64587.172(2)	64515.367(2)
1	64756.983(4)	64751.007(4)	–	24	64645.698(3)	64570.634(2)	64499.653(3)
2	64758.614(4)	64749.716(3)	64743.668(5)	25	64631.218(3)	64554.432(2)	64479.510(3)
3	64759.504(3)	64747.779(3)	64738.674(4)	26	64626.582(4)	64536.348(3)	64459.674(3)
4	64759.522(3)	64745.156(2)	64732.982(4)	27	64609.894(4)	64528.103(3)	64437.960(3)
5	64758.297(3)	64741.852(2)	64726.550(3)	28	64594.030(4)	64507.805(3)	64426.097(4)
6	64755.022(3)	64737.805(3)	64719.248(3)	29	64576.222(5)	64488.336(9)	64402.190(4)
7	64763.192(2)	64732.927(2)	64710.704(3)	30	64571.798(6)	64466.916(4)	64379.114(4)
8	64759.989(2)	64727.040(2)	64700.111(3)	31	64552.592(6)	64458.893(5)	64354.101(5)
9	64756.728(2)	64719.811(2)	64700.966(2)	32	64534.856(7)	64436.069(5)	64342.481(6)
10	64753.016(2)	64727.812(2)	64690.450(2)	33	64517.067(8)	64414.553(6)	64316.088(6)
11	64748.569(2)	64718.578(2)	64679.879(2)	34	64498.82(1)	64393.453(6)	64291.172(7)
12	64743.025(2)	64709.693(2)	64668.859(2)	35	64480.61(1)	64371.654(7)	64266.214(8)
13	64735.565(2)	64700.814(3)	64657.107(2)	36	64461.00(1)	64349.358(9)	64240.81(1)
14	64739.169(2)	64691.676(2)	64644.262(2)	37	64441.13(2)	64326.51(1)	64215.44(1)
15	64731.703(2)	64682.119(2)	64629.504(2)	38	64420.67(2)	64303.04(1)	64188.69(1)
16	64724.267(2)	64672.061(2)	64625.814(2)	39	64399.58(3)	64279.27(2)	64161.69(2)
17	64716.488(2)	64661.463(2)	64611.058(2)	40	64377.84(5)	64254.42(2)	64134.11(2)
18	64708.217(2)	64650.289(2)	64596.337(2)	41	–	64229.12(2)	–
19	64699.376(2)	64638.514(2)	64581.277(2)	42	64332.51(6)	64203.22(4)	–
20	64689.910(2)	64626.117(2)	64565.730(2)	43	–	64176.64(4)	–
21	64679.649(2)	64613.065(2)	64549.619(2)	44	–	64149.42(4)	–
22	64671.189(3)	64599.202(2)	64532.887(2)				

[1] In units of  $\text{cm}^{-1}$  and with  $1\sigma$  fitting uncertainties given in parentheses in units of the least-significant digit that are additional to a  $0.0015 \text{ cm}^{-1}$  systematic uncertainty.

**Table 6.5** Spin-forbidden lines arising in the VUV-FT absorption spectra.<sup>1</sup>

$J''$	${}^sR_{11ee}$	${}^rQ_{11fe}$	${}^qP_{11ee}$	${}^rR_{12ee}$	${}^qQ_{12fe}$	${}^pP_{12ee}$	${}^qR_{13ee}$	${}^pQ_{13fe}$	${}^oP_{13ee}$
					$e^3\Sigma^- - X^1\Sigma^+ (1,0)$				
1	64 787.53(9)				64 788.8(1)		64 799.0(2)		
2	64 785.26(7)				64 786.29(3)		64 801.30(6)		
3	64 781.72(2)				64 782.65(2)		64 802.2(2)		
4	64 777.24(1)				64 777.76(1)		64 802.0(3)		
5	64 772.109(5)		64 748.79(1)		64 771.70(1)		64 800.49(3)		
6	64 767.109(3)		64 736.97(1)		64 764.491(7)		64 797.76(2)		
7	64 748.755(6)		64 724.516(5)		64 756.242(6)		64 793.83(2)		64 752.90(3)
8	64 739.87(1)		64 712.199(3)		64 747.134(5)		64 788.60(3)		64 742.85(2)
9	64 729.11(2)		64 686.529(6)		64 737.477(4)		64 782.16(2)		64 731.60(2)
10			64 670.33(1)		64 710.706(3)		64 774.57(1)		64 719.06(3)
11			64 652.26(2)		64 699.299(6)		64 765.974(6)		64 705.31(2)
12					64 685.667(5)		64 756.651(6)		64 690.41(1)
13					64 670.15(2)		64 747.407(3)		64 674.512(6)
14					64 653.01(1)		64 725.223(4)		64 657.888(6)
15					64 634.40(2)		64 712.24(1)		64 641.346(3)
16					64 614.45(1)		64 697.36(2)		64 611.868(4)
17					64 593.08(1)				64 591.59(1)
18									64 569.43(2)

<sup>1</sup> In units of  $\text{cm}^{-1}$  and with  $1\sigma$  fitting uncertainties given in parentheses in units of the least-significant digit that are additional to a  $0.02 \text{ cm}^{-1}$  systematic uncertainty.

**Table 6.5** (continued from last page) Spin-forbidden lines arising in the VUV-FT absorption spectra.<sup>1</sup>

$J''$	${}^sR_{11ee}$	${}^rQ_{11fe}$	${}^qP_{11ee}$	${}^rR_{12ee}$	${}^qQ_{12fe}$	${}^pP_{12ee}$	${}^qR_{13ee}$	${}^pQ_{13fe}$	${}^oP_{13ee}$
$d^3\Delta - X^1\Sigma^+ (4,0)$									
22	64 665.341(5)								
23		64 581.366(7)							
24			64 493.805(5)	64 678.48(4)					
25			64 458.25(1)	64 649.95(1)					
26				64 609.73(1)	64 555.177(8)				
27					64 511.257(7)	64 456.70(1)			
28					64 477.29(3)	64 409.24(1)			
29							64 597.40(1)	64 522.68(3)	
30							64 551.25(2)	64 488.13(3)	
31								64 438.39(1)	64 375.28(1)
32								64 401.58(1)	64 321.94(2)

<sup>1</sup> In units of  $\text{cm}^{-1}$  and with  $1\sigma$  fitting uncertainties given in parentheses in units of the least-significant digit that are additional to a  $0.02 \text{ cm}^{-1}$  systematic uncertainty.

**Table 6.6** Transition frequencies of  $B^1\Sigma^+ - X^1\Sigma^+(0,0)$  in  $^{12}\text{C}^{18}\text{O}$  from the VUV-FT experiment.<sup>1</sup>

$J''$	$R$	$P$	$J''$	$R$	$P$
0	86 920.396(2)	–	26	87 033.287(2)	86 837.519(2)
1	86 924.156(2)	86 913.022(4)	27	87 038.218(2)	86 835.136(2)
2	86 927.966(2)	86 909.411(2)	28	87 043.198(2)*	86 832.803(2)
3	86 931.826(2)	86 905.847(2)	29	87 048.207(2)	86 830.514(2)
4	86 935.730(2)	86 902.334(2)	30	87 053.252(2)	86 828.282(2)*
5	86 939.680(2)	86 898.872(2)	31	87 058.339(2)	86 826.086(2)
6	86 943.681(2)	86 895.456(2)	32	87 063.460(2)	86 823.936(2)
7	86 947.730(2)	86 892.087(2)	33	87 068.600(2)*	86 821.835(2)
8	86 951.826(2)	86 888.771(2)	34	87 073.829(2)	86 819.776(2)
9	86 955.967(2)	86 885.504(2)	35	87 079.060(2)	86 817.746(2)*
10	86 960.155(2)	86 882.287(2)	36	87 084.338(3)	86 815.814(2)
11	86 964.382(2)*	86 879.117(2)	37	87 089.643(3)	86 813.894(2)
12	86 968.674(2)	86 875.998(2)	38	87 094.978(4)	86 812.029(3)
13	86 973.010(2)*	86 872.920(2)*	39	87 100.346(4)	86 810.202(3)
14	86 977.379(2)	86 869.911(2)	40	87 105.745(5)	86 808.416(4)
15	86 981.795(2)	86 866.949(2)*	41	87 111.187(6)	86 806.672(4)
16	86 986.259(2)	86 864.024(2)	42	87 116.669(7)	86 804.970(5)
17	86 990.770(2)	86 861.150(2)	43	87 122.135(9)	86 803.322(6)
18	86 995.319(2)	86 858.329(2)	44	87 127.67(1)	86 801.726(7)
19	86 999.916(2)	86 855.559(2)	45	87 133.20(1)	86 800.125(9)
20	87 004.557(2)	86 852.833(2)	46	87 138.79(2)	86 798.61(1)
21	87 009.238(2)	86 850.158(2)	47	87 144.44(2)	86 797.09(1)
22	87 013.966(2)	86 847.534(2)	48	87 150.03(3)	86 795.65(2)
23	87 018.739(2)*	86 844.956(2)	49	87 155.66(3)	–
24	87 023.542(2)	86 842.431(2)	50	87 161.39(4)	–
25	87 028.393(2)	86 839.956(2)*			

[1] In units of  $\text{cm}^{-1}$  and with  $1\sigma$  fitting uncertainties given in parentheses in units of the least-significant digit that are additional to a  $0.02 \text{ cm}^{-1}$  systematic uncertainty. Lines undergoing small perturbations in the  $B^1\Sigma^+$  state are indicated with (\*).

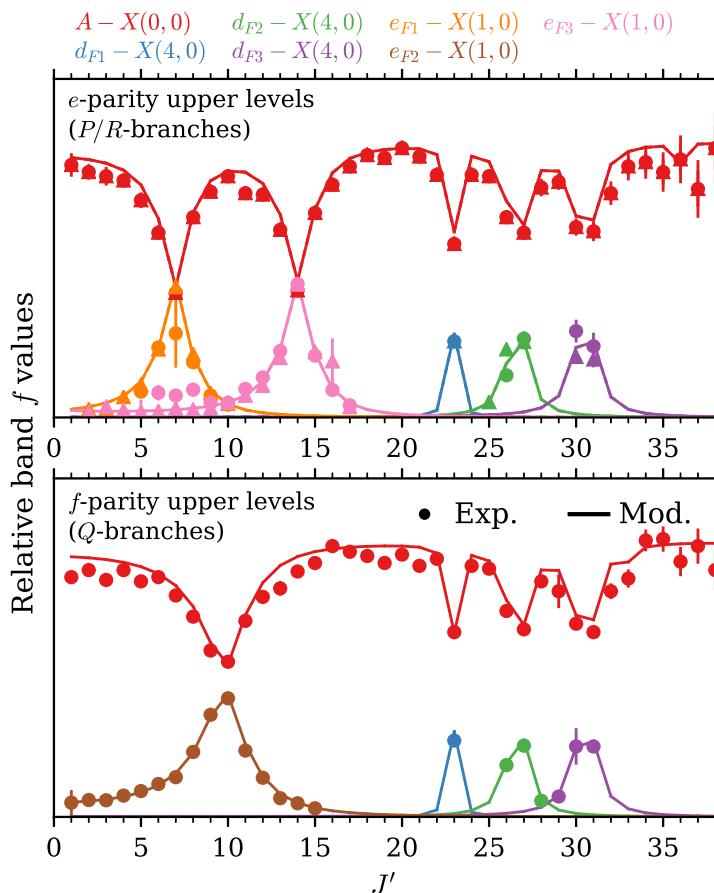


**Figure 6.5** Intensity sharing between  $A^1\Pi - X^1\Sigma^+(0,0)$  and overlapping bands. Band  $f$ -value for all transitions were calculated assuming the Hönl-London factors for a  $^1\Pi - ^1\Sigma^+$  transition. Points / error bars: experimental data (circles:  $P/Q$  branches, triangles:  $R$  branch). Lines: Results of the deperturbation model.

#### 6.4.2 $B^1\Sigma^+ \leftarrow X^1\Sigma^+(0,0)$

A spectrum of the  $B-X(0,0)$  absorption band near 115 nm is shown in Fig. 6.6, recorded with the FT-VUV instrument set at a spectral resolution of  $0.11 \text{ cm}^{-1}$ . A list of experimental transition energies is given in Table 6.6. Transition energies measured from this spectrum were combined with the VIS-FT spec-

## Fourier-transform absorption in the vacuum ultraviolet (VUV-FT)

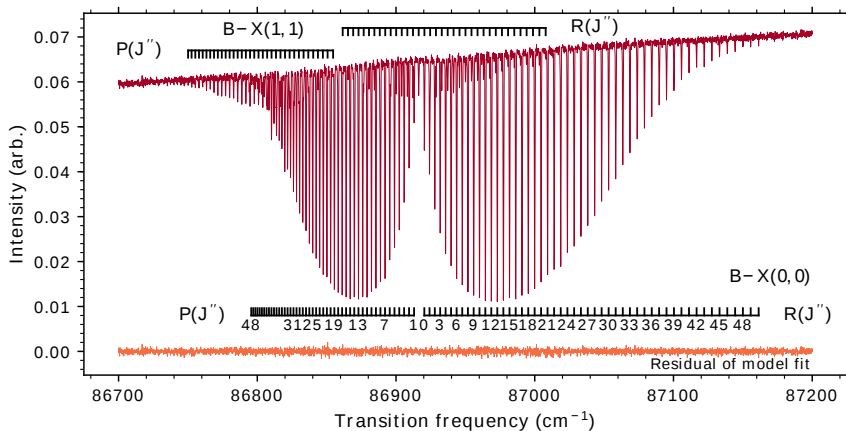


**Figure 6.6** Photoabsorption spectrum of  $B^1\Sigma^+ - X^1\Sigma^+(0,0)$  band with a sample temperature of  $1000 \pm 100$  K. The  $B-X(1,1)$  band also appears due to the higher temperature. The overall intensity slope is due to the continuum profile of the synchrotron beam. Also shown is the residual difference of the experimental spectrum and its modelled profile. Residuals are plotted on the same scale as the spectrum.

trum of  $A-X(0,0)$  to arrive at absolute term values for  $A(0)$ , which can be compared with those derived from the REMPI laser experiment. Additionally, the direct measurement of small perturbations in the  $B(0)$  energy levels, indicated with (\*) in Table 6.6, prevented these from being misinterpreted in  $B-A(0,0)$  spectra as arising from  $A(0)$ . The nature of levels interacting with  $B(0)$  interactions is beyond the scope of the current work and will be subsequently studied.

An absolute frequency calibration of the spectrum containing  $B-X(0,0)$  was made with respect to NIST data for several lines of atomic Kr, Xe, and H contaminating the spectrum. These lines were induced by absorption upstream in the synchrotron beam line at the location of the gas filter used for discriminating the harmonics produced by the undulator [191]. Since these lines are Doppler broadened under static gas conditions there should be no shift of their centre frequencies. Lines of  $^{12}\text{C}^{18}\text{O}$  itself, previously measured in several high-resolution laser-based experiments [173, 174, 196] concerning  $B-X(0,0)$  and other well-known transitions  $E^1\Pi - X^1\Sigma^+(1,0)$  and

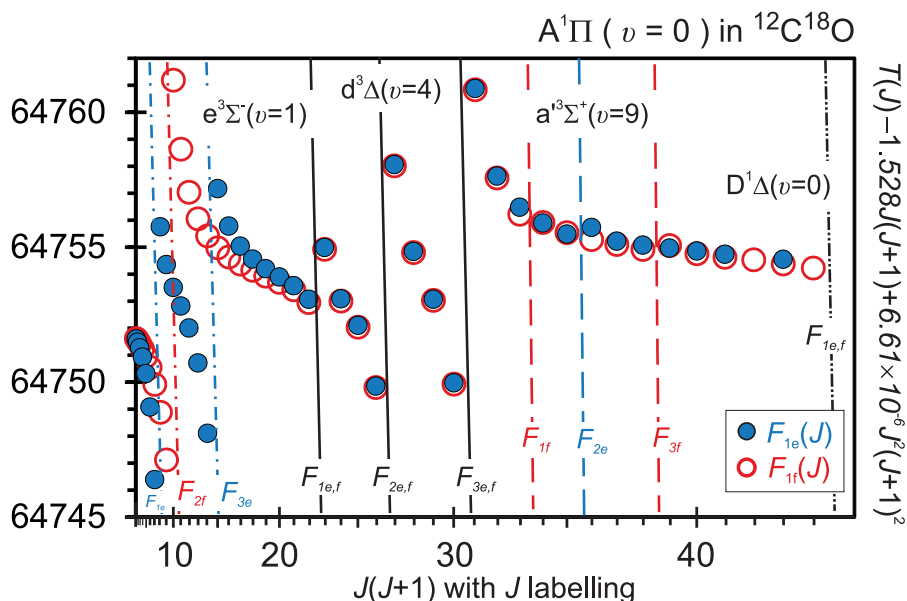


**Figure 6.7** Reduced term values (in  $\text{cm}^{-1}$ ) of the  $^{12}\text{C}^{18}\text{O}$   $A^1\Pi (v = 0)$  level and the perturbing rovibronic levels.

$C^1\Sigma^+ - X^1\Sigma^+(1,0)$  were used for calibration as well. The estimated accuracy of this absolute calibration is  $0.02 \text{ cm}^{-1}$ .

## 6.5 Perturbation analysis

The rotational term values of  $^{12}\text{C}^{18}\text{O}$   $A^1\Pi(v = 0)$  are plotted in Fig. 6.7 in reduced form. The crossing term series of  $e^3\Sigma^-(v = 1)$ ,  $d^3\Delta(v = 4)$ ,  $a^3\Sigma^+(v = 9)$ , and  $D^1\Delta(v = 0)$  are also indicated and are associated with shifts of the  $A(0)$  energy levels.

The  $\text{CO}$   $A^1\Pi$  state, especially its  $v = 0$  level, has one of the more complicated rotational structures among low-lying states of diatomic molecules due to the multiple rotational-electronic ( $L$ -uncoupling) and spin-orbit perturbations that affect it. The spin-orbit interactions of  $A(0)$  with the  $e^3\Sigma^-(v = 1)$ ,  $d^3\Delta(v = 4)$  and  $a^3\Sigma^+(v = 9)$  levels, as well as electronic-rotational interactions with  $D^1\Delta(v = 0)$  and  $I^1\Sigma^-(v = 0, 1)$  are responsible for these irregularities.

The strongest perturbation of A(0) rotational structure is due to spin-orbit interaction with the  $e^3\Sigma^-(v=1)$  at low  $J$  and is associated with a large splitting of  $e$ - and  $f$ -symmetry levels. An accurate treatment of this interaction is essential for determining a deperturbed value for the A(0) term origin and its mass dependence. All three spin substates of the  $d^3\Delta(v=4)$  level strongly perturb A(0) at mid- $J$ . The  $F_3$  substate induces the largest shifts because of the Hund's case (a) selection rule limiting the spin-orbit interaction of  $^1\Pi$  and  $^3\Delta$  states to their  $\Omega = 1$  components, in this case the  $F_3$  level of the inverted  $d^3\Delta$ . Relaxation of this rule by spin-rotational mixing then permits the further interactions with  $F_1$  and  $F_2$  levels. The A(0)~a'(9) interaction is weaker, with associated level shifts of  $\sim 0.5 \text{ cm}^{-1}$  occurring between  $J = 33$  and 39.

When comparing the perturbations evident in Fig. 6.7 with similar data and figures addressing other isotopologues (e.g.,  $^{12}\text{C}^{16}\text{O}$  [39, 197],  $^{13}\text{C}^{16}\text{O}$  [40, 198], and  $^{13}\text{C}^{17}\text{O}$  [41]) the crossings of A(0) with higher- $v$  e(1), d(4), a'(9) levels all occur at decreasing  $J$  with increasing reduced-mass,  $\mu$ , as is expected from the  $-\sqrt{\mu}\omega_e(v + \frac{1}{2})$  proportionality of first-order isotope shifts. Conversely, the level crossings of A(0) and D(0) occur at higher  $J$  for higher mass because of the smaller vibrational constant,  $\omega_e$ , of  $D^1\Delta$ .

To quantify the interaction energies and deperturbed molecular constants of all directly and indirectly observed levels we employ the same methodology as Niu et al. [39] and Hakalla [41] applied to other isotopologues. We used 476 transition frequencies obtained from the laser, VIS-FT and VUV-FT studies of A-X(0,0), B-A(0,0) and B-X(0,0) transitions and their satellite extra lines. We computed level energies and transition frequencies in a matrix diagonalization of all interacting levels. The effective Hamiltonian used has matrix elements described in Niu et al. (see Table 6 in [39]) and the deperturbation was performed using the Pgopher software [189]. The interpretation of the interaction parameters  $\xi$  and  $\eta$  were also discussed in [39] and in [181]. The rotational structure of the ground state was fixed to the  $^{12}\text{C}^{18}\text{O}$  constants of Coxon and Hajigeorgiou [178] throughout the analysis in the present paper and are listed in a footnote to Table 6.7.

The different sets of experimental data have different accuracies so we use relative weights to integrate them into a single molecular-parameter fit. A relative weight of 5 is assigned to data obtained from  $2 + 1'$  REMPI laser spectroscopy; 2 to isolated and strong lines in the VIS-FTS spectrum, and  $1 - 0.5$  for weak and/or blended transitions; and 1 to isolated and strong

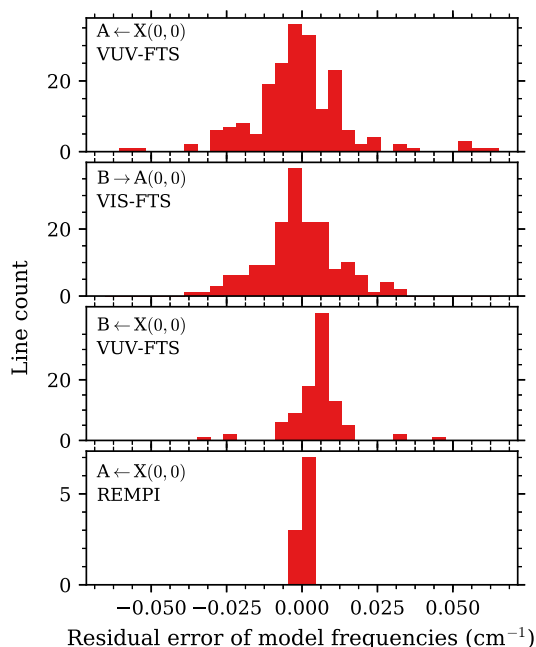


**Figure 6.8** Residual error of modelled line frequencies after deperturbation, shown separately for each experimental measurement. The histograms consist of residuals for the main bands and all observed extra lines.

lines in the the VUV-FTS spectrum and 0.5 – 0.1 to weak and/or blended transitions.

Fitted deperturbed molecular constants and interaction parameters are given in Table 6.7 with the same parameter definitions as in Niu et al. [39]. The root-mean-square error (RMSE) of unweighted transition-frequency residuals is  $0.014 \text{ cm}^{-1}$  after finalising the deperturbation fit. This measure of the overall quality-of-fit of the model to the experimental data is dominated by uncertainty in the least accurate  $B^1\Sigma^+ - X^1\Sigma^+(0,0)$  lines. This demonstrates an overall high level of agreement between the experimental and model frequencies. A correlation matrix was calculated during the least-squares fitting procedure and checked to ensure satisfactorily low correlation coefficients between the model parameters.

Figure 6.8 shows the residual error of the deperturbation model when compared with experimental frequencies. Histograms for each data set contributing to the deperturbation fit have a width representative of the random uncertainties for each experiment. As expected, the laser-absorption REMPI frequencies are least scattered; all values are within  $0.003 \text{ cm}^{-1}$  (see Table 6.1). The greater scatter of VUV-FTS data in the  $A \leftarrow X(0,0)$  region relative to  $B \leftarrow X(0,0)$  is due to a combination of the somewhat better instrumental resolution adopted for measurements of the latter and the greater number of weak and overlapped lines present in the former. A small  $+0.005 \text{ cm}^{-1}$  bias of the VUV-FTS  $B \leftarrow X(0,0)$  model residuals indicates a slight disagreement of the absolute calibration of this experiment relative to the others with a superior calibration to the REMPI laser experiment. Actually, under optimal conditions the VUV-FTS experiment is limited to an accuracy of  $0.01 \text{ cm}^{-1}$  [179], which is significantly larger than the systematic offset found here.

Modelled energies for all bands and excited-state term values are given as an online data archive. All bands and levels are extrapolated to  $J = 60$  but increasing errors are expected for levels which are not well constrained by the observed lines and crossings. There are also archived experimental spectra and the Pggopher input file used to perform our deperturbation.

The level mixing deduced from deperturbing the interaction of  $A(0)$  and its perturbers also provides a means to calculate the linestrength borrowed by extra lines that appear in the experimental  $B \rightarrow A$  and  $A \leftarrow X$  spectra. Modelled band  $f$ -values are compared with  $A \leftarrow X(0,0)$  absorption  $f$ -values in Fig. 6.5 and show good agreement, further validating the deperturbation model deduced from level energies.

The careful absolute calibration of our laser-based measurements with respect to the ground state energy means that the value for the deperturbed  $A(0)$   $T_v$  constant can be determined at high accuracy. Least-squares fitting of the deperturbation model returns a statistical uncertainty of  $0.0006 \text{ cm}^{-1}$  for this parameter. However, this statistical uncertainty is smaller than the  $0.001 \text{ cm}^{-1}$  absolute frequency uncertainty of our data (tied to the REMPI-laser experiment) and we conclude that the estimated uncertainty of  $T_0$  is  $0.001 \text{ cm}^{-1}$ . We list all residual differences of laser-measured and modelled frequencies in Table 6.1 and these show agreement between  $0.0001$  and  $0.003 \text{ cm}^{-1}$ .

A deperturbation analysis of  $^{12}\text{C}^{18}\text{O}$   $A(0)$  and perturbers was previously performed by Beaty et al. [167] based on comprehensive emission spectra of

$A-X(0, 0)$  and extra lines from perturbing states, with their deperturbed constants also listed in Table 6.7. A similar scale of experimental information was used in that previous work but with frequency uncertainties of  $0.05\text{ cm}^{-1}$  or more. Our new measurements, with uncertainties between about  $0.001$  and  $0.02\text{ cm}^{-1}$ , enable the determination of more constants defining the  $A(0)$  and perturber levels than previously, and with better precision. All comparable parameters show consistency between this work and that of Beaty et al. [167], given their estimated uncertainties, apart from the  $A(0)$  and  $d(4)$  term origins and the  $\eta_{A(0)\sim d(4)}$  interaction parameter. The  $T_v$  discrepancies likely arise from correlation of this parameter with high-order rotational constants and our inclusion of an additional constant,  $H$ , relative to Beaty et al. [167].

Some parameters in Table 6.7 are experimentally determined for the first time, for example, the  $\xi$  parameters that control the  $L$ -uncoupling matrix elements  $\langle A(0)|J_+L_-|D(0)\rangle$  and  $\langle A(0)|J_+L_-|I(1)\rangle$ . We do not experimentally observe spectral lines associated with  $D(0)$  nor  $I(1)$  and their avoided crossings with  $A(0)$  occur above our highest-observed  $J$  level. Fixed molecular constants representing the  $D(0)$  and  $I(1)$  levels are nevertheless included in our perturbation analysis by isotopically rescaling their electronic-state equilibrium constants found in the literature [199–202]. The  $D(0)\sim A(0)$  and  $I(1)\sim A(0)$  interaction parameters then exhibit quantitatively well-defined values  $\xi_{A(0)\sim D(0)} = 0.0229(48)\text{ cm}^{-1}$  and  $\xi_{A(0)\sim I(1)} = 0.0944(24)\text{ cm}^{-1}$  when included in the deperturbation optimisation. The  $\xi_{A(0)\sim D(0)}$  parameter is consistent within its uncertainty with a value calculated from the isotopically-invariant rotational-interaction parameter determined by Lefloch et al. [197] (parameter  $b$  in their Table. IV). A similar mass-scaling calculation is described by Hakalla [41]. The newly-determined  $\xi_{A(0)\sim I(1)}$  does not show such good agreement, differing by 36% from its rescaled value. This may be due to a poorer determination of this parameter in our deperturbation than suggested by its estimated uncertainty. The crossing point of  $A(0)$  and  $I(1)$  rotational series in  $^{12}\text{C}^{18}\text{O}$  occurs near  $J = 49$  while the maximum  $J$  of our experimentally-constrained term values is significantly lower  $J = 44$ , suggesting the possibility of some uncertainty.

**Table 6.7** Deperturbed molecular parameters of  $^{12}\text{C}^{18}\text{O}$  for the A(0) state and its perturbers, and B(0).<sup>a,b</sup> Perturbation parameters as discussed in Refs. [39, 181].

Constant	A <sup>1</sup> Π( $v=0$ ) (this work)	A <sup>1</sup> Π( $v=0$ ) Ref. [167] <sup>e</sup>	B <sup>1</sup> Σ <sup>+</sup> ( $v=0$ ) (this work)	D <sup>1</sup> Δ( $v=0$ ) (this work)	I <sup>1</sup> Σ <sup>-</sup> ( $v=0$ ) (this work)	I <sup>1</sup> Σ <sup>-</sup> ( $v=1$ ) (this work)
$T_v$	64755.71358(61)	64755.7020(92)	86916.6923(15)	65435.784 <sup>f</sup>	64558.877 <sup>h</sup>	65604.206 <sup>h</sup>
$B$	1.527662(10)	1.527624(29)	1.8554295(50)	1.18878 <sup>f</sup>	1.20084 <sup>h</sup>	1.184498 <sup>h</sup>
$D \times 10^6$	6.610(19)	6.700(16)	6.1022(28)	6.38 <sup>f</sup>	6.21 <sup>g</sup>	6.23 <sup>g</sup>
$H \times 10^{12}$	-36.6(85)			-0.26 <sup>g</sup>	2.59 <sup>g</sup>	2.59 <sup>g</sup>
$\xi$				0.0229(48)		0.0944(24)
$\xi_{theoret}^c$				0.0247	-0.04104	0.06942
$\delta_\xi^d$				7.1		36.0

**Table 6.7** (continued from last page) Deperturbed molecular parameters of  $^{12}\text{C}^{18}\text{O}$  for the A(0) state and its perturbers, and B(0).<sup>a,b</sup> Perturbation parameters as discussed in Refs. [39, 181].

Constant	$e^3\Sigma^-(v=1)$ (this work)	$e^3\Sigma^-(v=1)$ Ref. [167] <sup>e</sup>	$d^3\Delta(v=4)$ (this work)	$d^3\Delta(v=4)$ Ref. [167] <sup>e</sup>	$a'^3\Sigma^+(v=9)$ (this work)	$a'^3\Sigma^+(v=9)$ Ref. [167] <sup>e</sup>
$T_v(F_1)$	64787.6689(13)	64787.651(10)		64982.44(13)	65281.120(11)	65281.14(63)
$T_v(F_2)$			65015.4993(38)	65014.71(19)		
$T_v(F_3)$				65048.25(12)		
$B$	1.197568(17)		1.1759189(60)		1.1287 <sup>j</sup>	
$A$			-16.5441(41)			
$\lambda$	0.5311(27)	0.562(17)	1.257(17)		-1.15 <sup>j</sup>	
$\gamma \times 10^3$	-2.11(25)		-9 <sup>j</sup>			
$D \times 10^6$	6.18 <sup>h</sup>		5.98 <sup>j</sup>		5.81 <sup>j</sup>	
$H \times 10^{12}$	-1.73 <sup>g</sup>		-0.69 <sup>g</sup>		-0.35 <sup>g</sup>	
$A_D \times 10^4$			-0.1 <sup>j</sup>			
$\eta$	14.7564(21)	14.780(14) <sup>i</sup>	-21.9065(53)	-21.273(36) <sup>i</sup>	-2.538(22)	-2.54(14) <sup>i</sup>
$\eta_{theoret}^c$	14.6659	14.6659	-21.7426	-21.7426	-2.554	-2.554
$\delta_\eta^d$	0.6	0.8	0.8	2.2	0.6	0.5

<sup>a</sup> All values are in  $\text{cm}^{-1}$  except for relative errors which are given as percentages. <sup>b</sup> Molecular constants fitted during the model optimisation have uncertainties indicated in parentheses ( $1\sigma$ , in units of the least significant digit). All other parameters were fixed during the fitting procedure. The  $^{12}\text{C}^{18}\text{O}$  fundamental ground state level, X( $v=0$ ), was fixed to the following constants determined by Coxon and Hajigeorgiou [178]:  $G_v = 1\,055,717\,274\,0$ ,  $B_v = 1,830\,980\,706$ ,  $D_v = 5,550\,781\,79 \cdot 10^{-6}$ ,  $H_v = 5,018\,43 \cdot 10^{-12}$ ,  $L_v = -3,000\,8 \cdot 10^{-17}$ ,  $M_v = -3,80 \cdot 10^{-23}$ ,  $N_v = -6,0 \cdot 10^{-28}$ , and  $O_v = -3,0 \cdot 10^{-33} \text{cm}^{-1}$ .

<sup>c</sup> Theoretical rotation and spin-orbit interaction parameters calculated on the basis of isotopically-invariant scaling and calculation of vibrational overlap integrals for  $^{12}\text{C}^{18}\text{O}$ . <sup>d</sup> Difference between theoretical value, based on isotopic scaling, and the experimentally determined value in terms of a percentage:  $\delta_\eta = (\eta_{theoret} - \eta)/\eta_{theoret} \times 100$ . <sup>e</sup> We only list the free parameters fitted in [167]. <sup>f</sup> Obtained by isotopic scaling values taken from [202]. <sup>g</sup> Obtained by isotopic scaling values taken from [197]. <sup>h</sup> Obtained by isotopic scaling values taken from [199]. <sup>i</sup> Recalculated to the current definition of the spin-orbit parameter,  $\eta$ , using the relationship  $\eta = \alpha \times \sqrt{3}$ . <sup>j</sup> Obtained by isotopic scaling values taken from [167].

## Conclusion

The isotopologue-independent  $A^1\Pi\sim a'^3\Sigma^+$  perturbation parameter has a typical magnitude for spin-orbit interactions in CO [41],  $84.02(10)\text{ cm}^{-1}$ , and the weakness of the fitted  $A(0)\sim a'(9)$  interaction energy is then due to a relatively small overlap of vibrational wavefunctions. We calculate a normalised value for this matrix element,  $\langle v_{A(0)}|v_{a'(9)}\rangle = 0.071$  using the method of Refs. [41, 181] and find a value similar to other CO isotopologues, e.g. 0.070 and 0.072 with respect to  $^{12}\text{C}^{17}\text{O}$  and  $^{13}\text{C}^{17}\text{O}$ .

## 6.6 Conclusion

Three different state-of-the-art techniques were employed to gather transition frequencies of the  $A^1\Pi-X^1\Sigma^+(0,0)$ ,  $B^1\Sigma^+-X^1\Sigma^+(0,0)$ , and  $B^1\Sigma^+-A^1\Pi(0,0)$  bands in  $^{12}\text{C}^{18}\text{O}$  with the highest resolution and accuracy obtained to date. The spectra show many extra lines probing optically-forbidden transitions to the  $d^3\Delta(4)$ ,  $e^3\Sigma^-(1)$ , and  $a'^3\Sigma^+(9)$  levels, due to their interaction with  $A^1\Pi(0)$  by spin-orbit and rotational-electronic  $L$ -uncoupling. This spectroscopic data was included into an effective Hamiltonian model of all observed levels and their interactions.

Lines probing the  $d^3\Delta(4)$ ,  $e^3\Sigma^-(1)$ , and  $a'^3\Sigma^+(9)$  triplet state perturbers were observed directly, while interactions with the further remote perturber states  $D^1\Delta(0)$  and  $I^1\Sigma^-(1)$  were found to measurably affect the  $A(0)$  term values. As expected, the extents and strengths of perturbations arising in  $A^1\Pi(0)$  in  $^{12}\text{C}^{18}\text{O}$  level are similar to the cases of  $^{12}\text{C}^{16}\text{O}$  [39],  $^{13}\text{C}^{16}\text{O}$  [40], and  $^{13}\text{C}^{17}\text{O}$  [41].

The deperturbed term origin of  $A^1\Pi(v=0)$  is found with a precision of  $0.001\text{ cm}^{-1}$ . This term origin will be compared with our past and future measurements in other CO isotopologues to determine the precise magnitude of the  $A^1\Pi-X^1\Sigma^+(0,0)$  electronic isotopic shift.



## Bibliography

- [1] G. Herzberg. *Molecular Spectra and Molecular Structure I: Spectra of Diatomic Molecules*. Krieger Publishing Company, New York, second edition, (1989).
- [2] M. Born and R. Oppenheimer. Zur quantentheorie der molekeln. *Annalen der Physik*, 389(20), 457–484, (1927).
- [3] W. Demtroder. *Molecular Physics*. WILEY-VCH, (2005).
- [4] K. Pachucki and J. Komasa. Schrödinger equation solved for the hydrogen molecule with unprecedented accuracy. *J. Chem. Phys.*, 144, 164306, (2016).
- [5] K. Pachucki and J. Komasa. Accurate adiabatic correction in the hydrogen molecule. *J. Chem. Phys.*, 141, 224103, (2014).
- [6] K. Pachucki and J. Komasa. Nonadiabatic corrections to rovibrational levels of H<sub>2</sub>. *J. Chem. Phys.*, 130, 164113, (2009).
- [7] B. H. Bransden and C. J. Joachain. *Physics of Atoms and Molecules, Second edition*. Pearson, (2003).
- [8] K. Piszczatowski, G. Łach, M. Przybytek, J. Komasa, K. Pachucki, and B. Jeziorski. Theoretical determination of the dissociation energy of molecular hydrogen. *J. Chem. Theory Comput.*, 5, 3039–3048, (2009).
- [9] H. A. Bethe and E. E. Salpeter. *Quantum Mechanics of One- and Two-Electrons Atoms*. Dover Publications, (1977).
- [10] J. Komasa, K. Piszczatowski, G. Łach, M. Przybytek, B. Jeziorski, and K. Pachucki. Quantum electrodynamics effects in rovibrational spectra of molecular hydrogen. *J. Chem. Theory Comput.*, 7, 3105–3115, (2011).

## Bibliography

- [11] H. A. Bethe. The electromagnetic shift of energy levels. *Phys. Rev.*, 72, 339–341, (1947).
- [12] W. E. Lamb and R. C. Retherford. Fine structure of the hydrogen atom by a microwave method. *Phys. Rev.*, 72, 241–243, (1947).
- [13] G. Gabrielse, D. Hanneke, T. Kinoshita, M. Nio, and B. Odom. New determination of the fine structure constant from the electron  $g$  value and QED. *Phys. Rev. Lett.*, 97, 030802, (2006).
- [14] H. M. James and A. S. Coolidge. The ground state of the hydrogen molecule. *J. Chem. Phys.*, 1, 825–835, (1933).
- [15] W. Kołos and C. C. J. Roothaan. Accurate electronic wave functions for the  $H_2$  molecule. *Rev. Mod. Phys.*, 32, 219–232, (1960).
- [16] W. Kołos and L. Wolniewicz. Improved potential energy curve and vibrational energies for the electronic ground state of the hydrogen molecule. *J. Mol. Spectrosc.*, 54, 303–311, (1975).
- [17] W. Kołos and J. Rychlewski. Improved theoretical dissociation energy and ionization potential for the ground state of the hydrogen molecule. *J. Chem. Phys.*, 98, 3960–3967, (1993).
- [18] L. Wolniewicz. Relativistic energies of the ground state of the hydrogen molecule. *J. Chem. Phys.*, 99, 1851–1868, (1993).
- [19] L. Wolniewicz. Relativistic corrections to the energies of the  $EF$ ,  $GK$ , and  $H\bar{H} \ ^1\Sigma_g$  states of the hydrogen molecule. *J. Chem. Phys.*, 109(6), 2254, (1998).
- [20] K. Pachucki and J. Komasa. Gerade-ungerade mixing in the hydrogen molecule. *Phys. Rev. A*, 83, 042510, (2011).
- [21] M. Puchalski, J. Komasa, P. Czachorowski, and K. Pachucki. Complete  $\alpha^6 m$  corrections to the ground state of  $H_2$ . *Phys. Rev. Lett.*, 117, 263002, (2016).
- [22] J. Liu, E. J. Salumbides, U. Hollenstein, J. C. J. Koelemeij, K. S. E. Eikema, W. Ubachs, and F. Merkt. Determination of the ionization and dissociation energies of the hydrogen molecule. *J. Chem. Phys.*, 130, 174306, (2009).

## Bibliography

- [23] E. J. Salumbides, G. D. Dickenson, T. I. Ivanov, and W. Ubachs. QED effects in molecules: Test on rotational quantum states of H<sub>2</sub>. *Phys. Rev. Lett.* , 107, 043005, (2011).
- [24] G. D. Dickenson, M. L. Niu, E. J. Salumbides, J. Komasa, K. S. E. Eikema, K. Pachucki, and W. Ubachs. Fundamental vibration of molecular hydrogen. *Phys. Rev. Lett.* , 110, 193601, (2013).
- [25] R. Pohl, A. Antognini, F. Nez, F. D. Amaro, F. Biraben, J. M. R. Cardoso, D. S. Covita, A. Dax, S. Dhawan, L. M. P. Fernandes, A. Giesen, T. Graf, T. W. Hänsch, P. Indelicato, L. Julien, C. Y. Kao, P. Knowles, E.-O. L. Bigot, Y.-W. Liu, J. A. M. Lopes, L. Ludhova, C. M. B. Monteiro, F. Mulhauser, T. Nebel, P. Rabinowitz, J. M. F. dos Santos, L. A. Schaller, K. Schuhmann, C. Schwob, D. Taqqu, J. F. C. A. Veloso, and F. Kottmann. The size of the proton. *Nature*, 466, 213–216, (2010).
- [26] S. Karshenboim. Precision physics of simple atoms: QED tests, nuclear structure and fundamental constants. *Phys. Rep.*, 422(1-2), 1, (2005).
- [27] A. Campargue, S. Kassi, K. Pachucki, and J. Komasa. The absorption spectrum of H<sub>2</sub>: CRDS measurements of the (2-0) band, review of the literature data and accurate ab initio line list up to 35 000 cm<sup>-1</sup>. *Phys. Chem. Chem. Phys.*, 14, 802–815, (2012).
- [28] W. Ubachs, J. C. J. Koelemeij, K. S. E. Eikema, and E. J. Salumbides. Physics beyond the Standard Model from hydrogen spectroscopy. *J. Mol. Spectrosc.* , 320, 1 – 12, (2016).
- [29] E. J. Salumbides, J. C. J. Koelemeij, J. Komasa, K. Pachucki, K. S. E. Eikema, and W. Ubachs. Bounds on fifth forces from precision measurements on molecules. *Phys. Rev. D* , 87, 112008, (2013).
- [30] K. Pachucki. Born-Oppenheimer potential for H<sub>2</sub>. *Phys. Rev. A*, 82, 032509, (2010).
- [31] E. J. Salumbides, W. Ubachs, and V. I. Korobov. Bounds on fifth forces at the sub-Ångström length scale. *J. Mol. Spectrosc.* , 300, 65–69, (2014).
- [32] M. L. Niu, E. J. Salumbides, and W. Ubachs. Communication: Test of quantum chemistry in vibrationally hot hydrogen molecules. *J. Chem. Phys.* , 143, 081102, (2015).

- [33] J. Steadman and T. Baer. The production and characterization by resonance enhanced multiphoton ionization of  $\text{H}_2$  ( $v = 10 - 14$ ) from photodissociation of  $\text{H}_2\text{S}$ . *J. Chem. Phys.*, 91, 6113–6119, (1989).
- [34] S. Hannemann, E. J. Salumbides, S. Witte, R. T. Zinkstok, E. J. van Duijn, K. S. E. Eikema, and W. Ubachs. Frequency metrology on the  $EF^1\Sigma_g^+ - X^1\Sigma_g^+$  (0,0) transition in  $\text{H}_2$ , HD, and  $\text{D}_2$ . *Phys. Rev. A*, 74, 062514, (2006).
- [35] T. M. Trivikram, M. L. Niu, P. Wcisło, W. Ubachs, and E. J. Salumbides. Precision measurements and test of molecular theory in highly excited vibrational states of  $\text{H}_2$  ( $v = 11$ ). *Appl. Phys. B*, 122, 294, (2016).
- [36] M. Schlösser, X. Zhao, T. M. Trivikram, W. Ubachs, and E. J. Salumbides. CARS spectroscopy of the ( $v = 0 \rightarrow 1$ ) band in  $\text{T}_2$ . *J. Phys. B*, 50(21), 214004, (2017).
- [37] T. M. Trivikram, M. Schlösser, W. Ubachs, and E. J. Salumbides. Relativistic and QED effects in the fundamental vibration of  $\text{T}_2$ . *Phys. Rev. Lett.*, 120, 163002, (2018).
- [38] A. J. de Nijs, E. J. Salumbides, K. S. E. Eikema, W. Ubachs, and H. L. Bethlem. UV-frequency metrology on CO ( $a^3\Pi$ ): Isotope effects and sensitivity to a variation of the proton-to-electron mass ratio. *Phys. Rev. A*, 84, 052509, (2011).
- [39] M. L. Niu, E. J. Salumbides, D. Zhao, N. de Oliveira, D. Joyeux, L. Nahon, R. W. Field, and W. Ubachs. High resolution spectroscopy and perturbation analysis of the CO A  $^1\Pi - X^1\Sigma^+$  (0,0) and (1,0) bands. *Mol. Phys.*, 111, 2163–2174, (2013).
- [40] M. L. Niu, R. Hakalla, T. M. Trivikram, A. N. Heays, N. de Oliveira, E. J. Salumbides, and W. Ubachs. Spectroscopy and perturbation analysis of the A  $^1\Pi$  ( $v=0$ ) state of  $^{13}\text{C}^{16}\text{O}$ . *Mol. Phys.*, 114(19), 2857–2867, (2016).
- [41] R. Hakalla, M. L. Niu, R. W. Field, A. N. Heays, E. J. Salumbides, G. Stark, J. R. Lyons, M. Eidelsberg, J. L. Lemaire, S. R. Federman, N. de Oliveira, and W. Ubachs. Fourier-transform spectroscopy of  $^{13}\text{C}^{17}\text{O}$  and deperturbation analysis of the A  $^1\Pi$  ( $v = 0 - 3$ ) levels. *J. Quant. Spectr. Rad. Transfer*, 189, 312–328, (2017).

## Bibliography

- [42] T. M. Trivikram, R. Hakalla, A. N. Heays, M. L. Niu, S. Scheidegger, E. J. Salumbides, N. de Oliveira, R. W. Field, and W. Ubachs. Perturbations in the  $A^1\Pi, v = 0$  state of  $^{12}\text{C}^{18}\text{O}$  investigated via complementary spectroscopic techniques. *Mol. Phys.*, 115(24), 3178–3191, (2017).
- [43] R. Hakalla, T. M. Trivikram, A. N. Heays, E. J. Salumbides, N. de Oliveira, R. W. Field, and W. Ubachs. Precision spectroscopy and comprehensive analysis of perturbations in the  $A^1\Pi(v = 0)$  state of  $^{13}\text{C}^{18}\text{O}$ . *Mol. Phys.*, 0(0), 1–18, (2018). doi: 10.1080/00268976.2018.1495848.
- [44] T. W. Hänsch. Repetitively pulsed tunable dye laser for high resolution spectroscopy. *Appl. Opt.*, 11(4), 895–898, (1972).
- [45] T. W. Hänsch, M. D. Levenson, and A. L. Schawlow. Complete hyperfine structure of a molecular iodine line. *Phys. Rev. Lett.*, 26, 946–949, (1971).
- [46] T. W. Hänsch, S. A. Lee, R. Wallenstein, and C. Wieman. Doppler-free two-photon spectroscopy of hydrogen  $1s - 2s$ . *Phys. Rev. Lett.*, 34, 307–309, (1975).
- [47] T. W. Hänsch and B. Couillaud. Laser frequency stabilization by polarization spectroscopy of a reflecting reference cavity. *Opt. Commun.*, 35(3), 441 – 444, (1980).
- [48] R. Holzwarth, T. Udem, T. W. Hänsch, J. C. Knight, W. J. Wadsworth, and P. S. J. Russell. Optical frequency synthesizer for precision spectroscopy. *Phys. Rev. Lett.*, 85, 2264–2267, (2000).
- [49] T. W. Hänsch. Nobel lecture: Passion for precision. *Rev. Mod. Phys.*, 78, 1297–1309, (2006).
- [50] Ch. G. Parthey, A. Matveev, J. Alnis, B. Bernhardt, A. Beyer, R. Holzwarth, A. Maistrou, R. Pohl, K. Predehl, T. Udem, T. Wilken, N. Kolachevsky, M. Abgrall, D. Rovera, C. Salomon, P. Laurent, and T. W. Hänsch. Improved measurement of the hydrogen  $1s - 2s$  transition frequency. *Phys. Rev. Lett.*, 107, 203001, (2011).
- [51] A. Antognini, F. Nez, K. Schuhmann, F. D. Amaro, F. Biraben, J. M. R. Cardoso, D. S. Covita, A. Dax, S. Dhawan, M. Diepold, L. M. P. Fernandes, A. Giesen, A. L. Gouvea, T. Graf, T. W. Hänsch, P. Indelicato,

- L. Julien, C.-Y. Kao, P. Knowles, F. Kottmann, E.-O. Le Bigot, Y.-W. Liu, J. A. M. Lopes, L. Ludhova, C. M. B. Monteiro, F. Mulhauser, T. Nebel, P. Rabinowitz, J. M. F. dos Santos, L. A. Schaller, C. Schwob, D. Taqu, J. F. C. A. Veloso, J. Vogelsang, and R. Pohl. Proton structure from the measurement of 2s-2p transition frequencies of muonic hydrogen. *Science*, 339(6118), 417–420, (2013).
- [52] K. Pachucki and J. Komasa. Leading order nonadiabatic corrections to rovibrational levels of  $H_2$ ,  $D_2$ , and  $T_2$ . *J. Chem. Phys.*, 143, 034111, (2015).
- [53] V. I. Korobov, L. Hilico, and J.-P. Karr. Theoretical transition frequencies beyond 0.1 ppb accuracy in  $H_2^+$ ,  $HD^+$ , and antiprotonic helium. *Phys. Rev. A*, 89, 032511, (2014).
- [54] J. Biesheuvel, J.-P. Karr, L. Hilico, K. Eikema, W. Ubachs, and J. C. J. Koelemeij. Probing QED and fundamental constants through laser spectroscopy of vibrational transitions in  $HD^+$ . *Nat Commun.*, 7, 10385, (2015).
- [55] J.-P. Karr, L. Hilico, J. C. J. Koelemeij, and V. I. Korobov. Hydrogen molecular ions for improved determination of fundamental constants. *Phys. Rev. A*, 94, 050501, (2016).
- [56] E. J. Salumbides, A. N. Schellekens, B. Gato-Rivera, and W. Ubachs. Constraints on extra dimensions from precision molecular spectroscopy. *New J. Phys.*, 17, 033015, (2015).
- [57] S. Hannemann, E. J. Salumbides, and W. Ubachs. Reducing the first-order Doppler shift in a Sagnac interferometer. *Opt. Lett.*, 32(11), 1381, (2007).
- [58] U. Fantz and D. Wunderlich. Franck–condon factors, transition probabilities, and radiative lifetimes for hydrogen molecules and their isotopomers. *Atomic Data and Nuclear Data Tables*, 92(6), 853 – 973, (2006).
- [59] U. Fantz and D. Wunderlich. *Franck-Condon factors, transition probabilities and radiative lifetimes for Hydrogen molecules and their isotopomers*. Monograph INDC(NDS)-457, University Augsburg, Germany, (2004).

## Bibliography

- [60] M. Glass-Maujean, Ch. Jungen, H. Schmoranzner, I. Tulin, A. Knie, P. Reiss, and A. Ehresmann. Experimental and theoretical studies of excited states of H<sub>2</sub> observed in the absorption spectrum: II. The  $6p\pi$  and  $7p\pi$   $^1\Pi_u$  states. *J. Mol. Spectros.*, 293-294, 11–18, (2013).
- [61] M. Glass-Maujean, Ch. Jungen, A. Spielfiedel, H. Schmoranzner, I. Tulin, A. Knie, P. Reiss, and A. Ehresmann. Experimental and theoretical studies of excited states of H<sub>2</sub> observed in the absorption spectrum: I. The  $5p\pi D''$   $^1\Pi_u$  state. *J. Mol. Spectros.*, 293-294, 1–10, (2013).
- [62] M. Glass-Maujean, Ch. Jungen, H. Schmoranzner, I. Tulin, A. Knie, P. Reiss, and A. Ehresmann. Experimental and theoretical studies of excited states of H<sub>2</sub> observed in the absorption spectrum: III. The  $5p\sigma$ ,  $6p\sigma$  and  $7p\sigma$  states. *J. Mol. Spectros.*, 293-294, 19–26, (2013).
- [63] G. Herzberg and Ch. Jungen. Rydberg series and ionization potential of the H<sub>2</sub> molecule. *J. Mol. Spectrosc.*, 41, 425–486, (1972).
- [64] M. Glass-Maujean, Ch. Jungen, H. Schmoranzner, A. Knie, I. Haar, R. Hentges, W. Kielich, K. Jänkälä, and A. Ehresmann. H<sub>2</sub> superexcited states: Experimental and theoretical characterization of their competing decay-channel fluorescence, dissociation, and ionization. *Phys. Rev. Lett.*, 104, 183002, (2010).
- [65] S. Xu, R. van Dierendonck, W. Hogervorst, and W. Ubachs. A dense grid of reference iodine lines for optical frequency calibration in the range 595 - 655 nm. *J. Mol. Spectrosc.*, 201(2), 256, (2000).
- [66] B. Bodermann, H. Knöckel, and E. Tiemann. Widely usable interpolation formulae for hyperfine splittings in the  $^{127}\text{I}_2$  spectrum. *Eur. Phys. J. D*, 19(1), 31–44, (2002).
- [67] M. L. Niu, F. Ramirez, E. J. Salumbides, and W. Ubachs. High-precision laser spectroscopy of the CO  $A^1\Pi - X^1\Sigma^+$  (2,0), (3,0), and (4,0) bands. *J. Chem. Phys.*, 142(4), 044302, (2015).
- [68] J. Bakos. AC stark effect and multiphoton processes in atoms. *Phys. Rep.*, 31(3), 209 – 235, (1977).
- [69] J. Ye, H. J. Kimble, and H. Katori. Quantum state engineering and precision metrology using state-insensitive light traps. *Science*, 320 (5884), 1734–1738, (2008).

- [70] C. E. Otis and P. M. Johnson. The ac stark effect in molecular multiphoton ionization spectroscopy. *Chem. Phys. Lett.* , 83(1), 73 – 77, (1981).
- [71] W. M. Huo, K. P. Gross, and R. L. McKenzie. Optical stark effect in the two-photon spectrum of NO. *Phys. Rev. Lett.*, 54, 1012–1015, (1985).
- [72] B. Girard, N. Billy, J. Vigue, and J. C. Lehmann. Evidence for a dynamical stark effect in CO( $A^1\Pi$ ) two-photon excitation. *Chem. Phys. Lett.*, 102(2-3), 168 – 173, (1983).
- [73] T. Srinivasan, H. Egger, T. Luk, H. Pummer, and C. Rhodes. The influence of the optical stark shift on the two-photon excitation of the molecular hydrogen E,  $F^1\Sigma_g^+$  state. *IEEE J Quantum Electron*, 19(12), 1874–1876, (1983).
- [74] M. J. J. Vrakking, A. S. Bracker, T. Suzuki, and Y. T. Lee. Ultrasensitive detection of hydrogen molecules by (2+1) resonance-enhanced multiphoton ionization. *Rev. Scient. Instr.* , 64(3), 645–652, (1993).
- [75] A. Yiannopoulou, N. Melikechi, S. Gangopadhyay, J. C. Meiners, C. H. Cheng, and E. E. Eyler. Determinations of  $EF^1\Sigma_g^+ - X^1\Sigma_g^+$  transition frequencies in  $H_2$ ,  $D_2$ , and HD. *Phys. Rev. A* , 73(2), 022506, (2006).
- [76] L. Li, B.-X. Yang, and P. M. Johnson. Alternating-current stark-effect line shapes in multiphoton ionization spectra. *J. Opt. Soc. Am. B*, 2(5), 748–752, (1985).
- [77] P. F. Liao and J. E. Bjorkholm. Direct observation of atomic energy level shifts in two-photon absorption. *Phys. Rev. Lett.*, 34, 1540–1540, (1975).
- [78] M. L. Niu, E. J. Salumbides, G. D. Dickenson, K. S. E. Eikema, and W. Ubachs. Precision spectroscopy of the  $X^1\Sigma_g^+, v = 0 \rightarrow 1 (J = 0 - 2)$  rovibrational splittings in  $H_2$ , HD and  $D_2$ . *J. Mol. Spectrosc.* , 300, 44–54, (2014).
- [79] W. L. Glab and J. P. Hessler. Multiphoton excitation of high singlet np Rydberg states of molecular hydrogen: Spectroscopy and dynamics. *Phys. Rev. A*, 35, 2102–2110, (1987).

## Bibliography

- [80] H. Pummer, H. Egger, T. S. Luk, T. Srinivasan, and C. K. Rhodes. Vacuum-ultraviolet stimulated emission from two-photon-excited molecular hydrogen. *Phys. Rev. A*, 28, 795–801, (1983).
- [81] T. Srinivasan, H. Egger, H. Pummer, and C. K. Rhodes. Generation of extreme ultraviolet radiation at 79 nm by sum frequency mixing. *IEEE J Quantum Electron*, 19, 1270–1276, (1983).
- [82] D. Bailly, E. Salumbides, M. Vervloet, and W. Ubachs. Accurate level energies in the  $EF^1\Sigma_g^+$ ,  $GK^1\Sigma_g^+$ ,  $H^1\Sigma_g^+$ ,  $B^1\Sigma_u^+$ ,  $C^1\Pi_u$ ,  $B'^1\Sigma_u^+$ ,  $D^1\Pi_u$ ,  $I^1\Pi_g$ ,  $J^1\Delta_g$  states of  $H_2$ . *Mol. Phys.*, 108, 827–846, (2010).
- [83] M. Puchalski, J. Komasa, P. Czachorowski, and K. Pachucki. Complete  $\alpha^6 m$  corrections to the ground state of  $H_2$ . *Phys. Rev. Lett.*, 117, 263002, (2016).
- [84] M. Puchalski, J. Komasa, and K. Pachucki. Relativistic corrections for the ground electronic state of molecular hydrogen. *Phys. Rev. A*, 95, 052506, (2017).
- [85] E. E. Marinero, R. Vasudev, and R. N. Zare. The E, F  $^1\Sigma_g^+$  double-minimum state of hydrogen: Two-photon excitation of inner and outer wells. *J. Chem. Phys.*, 78(2), 692–699, (1983).
- [86] G. D. Dickenson, E. J. Salumbides, M. Niu, Ch. Jungen, S. C. Ross, and W. Ubachs. Precision spectroscopy of high rotational states in  $H_2$  investigated by Doppler-free two-photon laser spectroscopy in the  $EF^1\Sigma_g^+ - X^1\Sigma_g^+$  system. *Phys. Rev. A*, 86(3), 032502, (2012).
- [87] A. T. J. B. Eppink and D. H. Parker. Velocity map imaging of ions and electrons using electrostatic lenses: Application in photoelectron and photofragment ion imaging of molecular oxygen. *Rev. Scient. Instr.*, 68(9), 3477–3484, (1997).
- [88] P. M. Dehmer and W. A. Chupka. Very high resolution study of photoabsorption, photoionization, and predissociation in  $H_2$ . *J. Chem. Phys.*, 65, 2243–2273, (1976).
- [89] M. A. O'Halloran, S. T. Pratt, F. S. Tomkins, J. L. Dehmer, and P. M. Dehmer. Competition between rotational and vibrational autoionization in  $H_2$ . *Chem. Phys. Lett.*, 146(3-4), 291–296, (1988).

## Bibliography

- [90] Ch. Jungen, S. T. Pratt, and S. C. Ross. Multichannel quantum defect theory and double-resonance spectroscopy of autoionizing levels of molecular hydrogen. *J. Phys. Chem.*, 99, 1700–1710, (1995).
- [91] M. Glass-Maujean, Ch. Jungen, G. Reichardt, A. Balzer, H. Schmoranzler, A. Ehresmann, I. Haar, and P. Reiss. Competing decay-channel fluorescence, dissociation, and ionization in superexcited levels of H<sub>2</sub>. *Phys. Rev. A*, 82, 062511, (2010).
- [92] D. Wunderlich and U. Fantz. Franck-Condon factors for molecule-ion reactions of H<sub>2</sub> and its isotopomers. *Atomic Data and Nuclear Data Tables*, 97(2), 152 – 185, (2011).
- [93] S. Yu and K. Dressler. Calculation of rovibronic structures in the lowest nine excited  $^1\Sigma_g^+$ ,  $^1\Pi_g$ ,  $^1\Delta_g$  states of H<sub>2</sub>, D<sub>2</sub>, and T<sub>2</sub>. *J. Chem. Phys.*, 101(9), 7692, (1994).
- [94] W. Huo, K. Rinnen, and R. N. Zare. Rotational and vibrational effects in the  $E^1\Sigma_g^+ - X^1\Sigma_g^+$  two-photon transitions of H<sub>2</sub>, HD, and D<sub>2</sub>. *J. Chem. Phys.*, 95(1), 205, (1991).
- [95] N. Mukherjee, W. E. Perreault, and R. N. Zare. Stark-induced adiabatic Raman ladder for preparing highly vibrationally excited quantum states of molecular hydrogen. *J. Phys. B*, 50(14), 144005, (2017).
- [96] M. Agúndez, J. R. Goicoechea, J. Cernicharo, A. Faure, and E. Roueff. The chemistry of vibrationally excited H<sub>2</sub> in the interstellar medium. *Astroph. J.*, 713(1), 662, (2010).
- [97] I. Dabrowski. The Lyman and Werner bands of H<sub>2</sub>. *Can. J. Phys.*, 62(12), 1639–1664, (1984).
- [98] P. Senn, P. Quadrelli, K. Dressler, and G. Herzberg. Spectroscopic identification of the lowest rotation-vibration levels of the  $2p\sigma^2F^1\Sigma_g^+$  state of the H<sub>2</sub> molecule. *J. Chem. Phys.*, 83(3), 962, (1985).
- [99] E. E. Marinero, C. T. Rettner, and R. N. Zare. Quantum-state-specific detection of molecular hydrogen by three-photon ionization. *Phys. Rev. Lett.*, 48(19), 1323–1326, (1982).

## Bibliography

- [100] A. J. R. Heck, W. M. Huo, R. N. Zare, and D. W. Chandler.  $D_2 E, F^1\Sigma_g^+$  ( $v' = 0$  and  $1$ ) -  $X^1\Sigma_g^+$  ( $v = 0 - 5$ ) transition energies for  $J' = J'' = 0-26$ : Comparison of experiment and theory. *J. Mol. Spectrosc.*, 173(2), 452, (1995).
- [101] M. Ashfold, J. Bayley, R. Dixon, and J. Prince. Molecular predissociation dynamics revealed through multiphoton ionisation spectroscopy. III. New  $^1A_2$  and  $^1B_1$  Rydberg states in  $H_2S$  and  $D_2S$ . *Chem. Phys.*, 98 (2), 289 – 313, (1985).
- [102] C. A. Mayhew, J.-P. Connerade, M. A. Baig, M. N. R. Ashfold, J. M. Bayley, R. N. Dixon, and J. D. Prince. High-resolution studies of the electronic spectra of  $H_2S$  and  $D_2S$ . *J. Chem. Soc., Faraday Trans. 2*, 83, 417–434, (1987).
- [103] R. Roberge and D. R. Salahub. Valence and Rydberg excited states of  $H_2S$ : An SCF- $X\alpha$ -SW molecular orbital study. *J. Chem. Phys.*, 70(3), 1177–1186, (1979).
- [104] R. S. Mulliken. Electronic structures of polyatomic molecules. VII. Ammonia and Water type molecules and their derivatives. *J. Chem. Phys.*, 3(8), 506–514, (1935).
- [105] G. Herzberg. *Molecular Spectra and Molecular Structure III: Electronic spectra and electronic structure of polyatomic molecules; page 447*. Van Nostrand, New York, First edition, (1966).
- [106] G. N. A. van Veen, K. A. Mohamed, T. Baller, and A. E. de Vries. Photofragmentation of  $H_2S$  in the first continuum. *Chem. Phys.*, 74 (2), 261 – 271, (1983).
- [107] R. E. Continetti, B. A. Balko, and Y. T. Lee. Photodissociation of  $H_2S$  and the HS radical at 193.3 nm. *Chem. Phys. Lett.*, 182(5), 400 – 405, (1991).
- [108] J. W. Thoman Jr, D. W. Chandler, D. H. Parker, and M. H. M. Janssen. Two-dimensional imaging of photofragments. *Laser Chemistry*, 9(1-3), 27–46, (1988).
- [109] J. Steadman and T. Baer. The production and spectroscopy of excited sulfur atoms from the two-photon dissociation of  $H_2S$ . *J. Chem. Phys.*, 89, 5507–5513, (1988).

- [110] Ch. Jungen. *Handbook of High Resolution Spectroscopy*, Editors F. Merkt and M. Quack, Chapter: Elements of Quantum Defect Theory. Wiley, Chichester and New York, (2011).
- [111] M. Glass-Maujean and Ch. Jungen. Nonadiabatic ab initio multichannel quantum defect theory applied to absolute experimental absorption intensities in H<sub>2</sub>. *J. Phys. Chem. A*, 113, 13124–13132, (2009).
- [112] G. Staszewska and L. Wolniewicz. Adiabatic energies of excited <sup>1</sup>Σ<sub>u</sub> states of the hydrogen molecule. *J. Mol. Spectrosc.*, 212, 208–212, (2002).
- [113] M. Glass-Maujean, Ch. Jungen, A. Vasserot, H. Schmoranzler, A. Knie, S. Kübler, A. Ehresmann, and W. Ubachs. Experimental and theoretical studies of the *n*pσ<sup>1</sup>Σ<sub>u</sub><sup>+</sup> and *n*pπ<sup>1</sup>Π<sub>u</sub><sup>+</sup> (*n* ≥ 4, *N'* = 1 – 6) states of D<sub>2</sub>: Energies, natural widths, absorption line intensities, and dynamics. *J. Mol. Spectrosc.*, 338, 22 – 71, (2017).
- [114] Ch. Jungen and M. Raoult. Spectroscopy in the ionisation continuum. vibrational preionisation in H<sub>2</sub> calculated by multichannel quantum-defect theory. *Faraday Discuss. Chem. Soc.*, 71, 253–271, (1981).
- [115] F. Texier, Ch. Jungen, and S. C. Ross. Quantum beats and Kepler motion in fast competing photoionization and photodissociation processes. *Faraday Discuss.*, 115, 71–78, (2000).
- [116] P. Maddaloni, P. Malara, E. D. Tommasi, M. D. Rosa, I. Ricciardi, G. Gagliardi, F. Tamassia, G. D. Lonardo, and P. D. Natale. Absolute measurement of the S(0) and S(1) lines in the electric quadrupole fundamental band of D<sub>2</sub> around 3 μm. *J. Chem. Phys.*, 133, 154317, (2010).
- [117] S. Kassi and A. Campargue. Electric quadrupole and dipole transitions of the first overtone band of HD by CRDS between 1.45 and 1.33 μm. *J. Mol. Spectrosc.*, 267(1-2), 36–42, (2011).
- [118] S. Kassi, A. Campargue, K. Pachucki, and J. Komasa. The absorption spectrum of D<sub>2</sub>: Ultrasensitive cavity ring down spectroscopy of the (2-0) band near 1.7 μm and accurate ab initio line list up to 24 000 cm<sup>-1</sup>. *J. Chem. Phys.*, 136, 184309, (2012).

## Bibliography

- [119] Y. Tan, J. Wang, C.-F. Cheng, X.-Q. Zhao, A.-W. Liu, and S.-M. Hu. Cavity ring-down spectroscopy of the electric quadrupole transitions of in the 784 – 852 nm region. *J. Mol. Spectrosc.*, 300, 60–64, (2014).
- [120] J. Liu, D. Sprecher, Ch. Jungen, W. Ubachs, and F. Merkt. Determination of the ionization and dissociation energies of the deuterium molecule ( $D_2$ ). *J. Chem. Phys.*, 132, 154301, (2010).
- [121] D. Sprecher, J. Liu, Ch. Jungen, W. Ubachs, and F. Merkt. Communication: The ionization and dissociation energies of HD. *J. Chem. Phys.*, 133, 111102, (2010).
- [122] G. H. Dieke. The molecular spectrum of hydrogen and its isotopes. *J. Mol. Spectrosc.*, 2, 494–517, (1958).
- [123] H. G. M. Edwards, D. A. Long, and H. R. Mansour. Pure rotational and vibration-rotational Raman spectra of tritium,  $^3H_2$ . *J. Chem. Soc., Faraday Trans. 2*, 74, 1203–1207, (1978).
- [124] H. G. M. Edwards, D. A. Long, H. R. Mansour, and K. A. B. Najm. The pure rotational and vibration-rotational Raman spectra of  $^1H^3H$  and  $^2H^3H$ . *J. Raman Spectrosc.*, 8(5).
- [125] D. Veirs and G. Rosenblatt. Raman line positions in molecular hydrogen:  $H_2$ , HD, HT,  $D_2$ , DT, and  $T_2$ . *J. Mol. Spectrosc.*, 121, 401–419, (1987).
- [126] M.-C. Chuang and R. N. Zare. Rotation-vibration spectrum of HT: Line position measurements of the 1-0, 4-0, and 5-0 bands. *J. Mol. Spectrosc.*, 121(2), 380 – 400, (1987).
- [127] C. Schwartz and R. J. Le Roy. Nonadiabatic eigenvalues and adiabatic matrix elements for all isotopes of diatomic hydrogen. *J. Mol. Spectrosc.*, 121, 420–439, (1987).
- [128] KATRIN Collaboration. *KATRIN design report 2004*. FZK - FZKA 7090, (2005).
- [129] L. I. Bodine, D. S. Parno, and R. G. H. Robertson. Assessment of molecular effects on neutrino mass measurements from tritium  $\beta$  decay. *Phys. Rev. C*, 91, 035505, (2015).

- [130] A. Saenz, S. Jonsell, and P. Froelich. Improved molecular final-state distribution of  $\text{HeT}^+$  for the  $\beta$ -decay process of  $\text{T}_2$ . *Phys. Rev. Lett.*, 84, 242–245, (2000).
- [131] N. Doss, J. Tennyson, A. Saenz, and S. Jonsell. Molecular effects in investigations of tritium molecule  $\beta$  decay endpoint experiments. *Phys. Rev. C*, 73, 025502, (2006).
- [132] R. J. H. Clark and R. E. Hester. *Advances in Non-Linear Spectroscopy*, volume 15 of *Advances in Spectroscopy*. Wiley, (1988).
- [133] D. J. Taylor, M. Glugla, and R.-D. Penzhorn. Enhanced Raman sensitivity using an actively stabilized external resonator. *Rev. Sci. Instrum.*, 72(4), 1970–1976, (2001).
- [134] M. Sturm, M. Schlösser, R. J. Lewis, B. Bornschein, G. Drexlin, and H. H. Telle. Monitoring of all hydrogen isotopologues at Tritium Laboratory Karlsruhe using Raman spectroscopy. *Laser Phys.*, 20(2), 493–507, (2010).
- [135] L. Dörr, U. Besserer, N. Bekris, B. Bornschein, C. Caldwell-Nichols, D. Demange, I. Cristescu, I. Cristescu, M. Glugla, G. Hellriegel, P. Schäfer, S. Weite, and J. Wendel. A decade of tritium technology development and operation at the Tritium Laboratory Karlsruhe. *Fusion Sci. Technol.*, 54(1), 143–148, (2008).
- [136] M. Schlösser, B. Bornschein, S. Fischer, T. M. James, F. Kassel, S. Rupp, M. Sturm, and H. H. Telle. Raman spectroscopy at the Tritium Laboratory Karlsruhe. *Fusion Science and Technology*, 67(3), 555–558, (2015).
- [137] S. Gerstenkorn and P. Luc. *Atlas du Spectre d’Absorption de la Molecule d’Iode* 15 600 – 17 600  $\text{cm}^{-1}$ . Laboratoire Aimé Cotton, CNRS II, 91405 Orsay, France, (1977).
- [138] A. Slenczka, G. Marowsky, and M. Vodegel.  $\text{H}_2$  vibrational CARS thermometry. *Appl. Phys. B*, 47(1), 41–46, (1988).
- [139] L. A. Rahn, R. L. Farrow, M. L. Koszykowski, and P. L. Mattern. Observation of an optical stark effect on vibrational and rotational transitions. *Phys. Rev. Lett.*, 45, 620–623, (1980).

## Bibliography

- [140] R. L. Farrow and L. A. Rahn. Optical stark splitting of rotational Raman transitions. *Phys. Rev. Lett.*, 48, 395–398, (1982).
- [141] M. J. Dyer and W. K. Bischel. Optical stark shift spectroscopy: Measurement of the  $v = 1$  polarizability in  $H_2$ . *Phys. Rev. A*, 44, 3138–3143, (1991).
- [142] A. D. May, V. Degen, J. C. Stryland, and H. L. Welsh. The Raman effect in gaseous hydrogen at high pressures. *Can. J. Phys.*, 39(12), 1769–1783, (1961).
- [143] L. Rahn and G. Rosasco. Measurement of the density shift of the  $H_2$  Q(0-5) transitions from 295 to 1000 K. *Phys. Rev. A*, 41, 3698–3706, (1990).
- [144] E. Looi, J. Stryland, and H. Welsh. Pressure shifts in the vibrational Raman spectra of hydrogen and deuterium, 315-85 K. *Can. J. Phys.*, 56, 1102, (1978).
- [145] S. Kassi and A. Campargue. Electric quadrupole transitions and collision-induced absorption in the region of the first overtone band of  $H_2$  near  $1.25 \mu m$ . *J. Mol. Spectrosc.*, 300, 55 – 59, (2014).
- [146] C.-F. Cheng, Y. R. Sun, H. Pan, J. Wang, A.-W. Liu, A. Campargue, and S.-M. Hu. Electric-quadrupole transition of  $H_2$  determined to  $10^{-9}$  precision. *Phys. Rev. A*, 85, 024501, (2012).
- [147] K. Pachucki and J. Komasa. Rovibrational levels of HD. *Phys. Chem. Chem. Phys.*, 12, 9188–9196, (2010).
- [148] R. P. Lucht and R. L. Farrow. Saturation effects in coherent anti-stokes Raman scattering spectroscopy of hydrogen. *J. Opt. Soc. Am. B*, 6(12), 2313–2325, (1989).
- [149] A. Owyong and P. Esherick. Sub-doppler Raman saturation spectroscopy. *Opt. Lett.*, 5(10), 421–423, (1980).
- [150] K. S. E. Eikema, W. Ubachs, W. Vassen, and W. Hogervorst. Lamb shift measurement in the  $1^1S$  ground state of helium. *Phys. Rev. A*, 55(3), 1866, (1997).

## Bibliography

- [151] M. S. Fee, K. Danzmann, and S. Chu. Optical heterodyne measurement of pulsed lasers: Toward high-precision pulsed spectroscopy. *Phys. Rev. A*, 45, 4911–4924, (1992).
- [152] S. Gangopadhyay, N. Melikechi, and E. E. Eyler. Optical phase perturbations in nanosecond pulsed amplification and second-harmonic generation. *J. Opt. Soc. Am. B*, 11(1), 231–241, (1994).
- [153] M. Stanke and L. Adamowicz. Non-born-oppenheimer calculations of the pure vibrational spectrum of T<sub>2</sub> including relativistic corrections. *J. Chem. Phys.*, 141(15), 154302, (2014).
- [154] I. Angeli and K. Marinova. Table of experimental nuclear ground state charge radii: An update. *Atomic Data and Nuclear Data Tables*, 99(1), 69 – 95, (2013).
- [155] R. Pohl, F. Nez, L. M. P. Fernandes, F. D. Amaro, F. Biraben, J. M. R. Cardoso, D. S. Covita, A. Dax, S. Dhawan, M. Diepold, A. Giesen, A. L. Gouvea, T. Graf, T. W. Hänsch, P. Indelicato, L. Julien, P. Knowles, F. Kottmann, E.-O. Le Bigot, Y.-W. Liu, J. A. M. Lopes, L. Ludhova, C. M. B. Monteiro, F. Mulhauser, T. Nebel, P. Rabinowitz, J. M. F. dos Santos, L. A. Schaller, K. Schuhmann, C. Schwob, D. Taqqu, J. F. C. A. Veloso, A. Antognini, and The CREMA Collaboration. Laser spectroscopy of muonic deuterium. *Science*, 353(6300), 669–673, (2016).
- [156] R. T. Birge. The band spectra of CO. *Phys. Rev.*, 28, 1157–1181, (1926).
- [157] G. Herzberg. On the band spectra of CO. *Zeitschr. f. Physik*, 52, 815–845, (1929).
- [158] R. W. Field, S. G. Tilford, R. A. Howard, and J. D. Simmons. Fine structure and perturbation analysis of the a<sup>3</sup>Π state of CO. *J. Mol. Spectrosc.*, 44(2), 347–382, (1972).
- [159] R. W. Field, B. G. Wicke, J. D. Simmons, and S. G. Tilford. Analysis of perturbations in the a<sup>3</sup>Π and A<sup>1</sup>Π states of CO. *J. Mol. Spectrosc.*, 44(2), 383–399, (1972).
- [160] M. Rytel. *Acta Phys. Polonica*, A38, 299, (1970).
- [161] J. Janjić, J. Danielak, R. Kepa, and M. Rytel. Weak angstrom bands of <sup>13</sup>C<sup>16</sup>O and <sup>12</sup>C<sup>18</sup>O molecules. *Acta Phys. Polon. A*, 41, 757, (1972).

## Bibliography

- [162] J. Janjić, L. U. Čonkić, D. S. Pešić, R. Kepa, and M. Rytel. The Herzberg system of  $^{12}\text{C}^{18}\text{O}$  molecule. *J. Mol. Spectr.*, 72(2), 297 – 300, (1978).
- [163] R. Kępa, M. Rytel, and Z. Rzeszut.  $E^1\Pi-A^1\Pi$  system bands in (CO)- $\text{C}^{13}\text{O}^{16}$  and (CO)- $\text{C}^{12}\text{O}^{18}$  molecules. *Acta Phys. Polon. A*, 54, 355–361, (1978).
- [164] R. Kępa. High-resolution emission-spectra of the 0-0, 0-1 and 0-2 bands of  $E^1\Pi-A^1\Pi$  and  $B^1\Sigma^+-A^1\Pi$  transitions in (CO)- $\text{C}^{12}\text{O}^{18}$  molecule. *Acta Phys. Hung.*, 60, 227–237, (1986).
- [165] C. Haridass, S. P. Reddy, and A. C. Le Floch. Precise rovibronic term values of some vibrational levels of the  $A^1\Pi$ ,  $B^1\Sigma^+$ ,  $C^1\Sigma^+$ , and  $E^1\Pi$  states of  $^{12}\text{C}^{18}\text{O}$  and  $^{13}\text{C}^{18}\text{O}$ . *J. Mol. Spectr.*, 168(2), 429–441, (1994).
- [166] C. Haridass, S. P. Reddy, and A. C. Le Floch. The fourth positive ( $A^1\Pi - X^1\Sigma^+$ ) system of  $^{12}\text{C}^{18}\text{O}$  and  $^{13}\text{C}^{18}\text{O}$ : Perturbations in the  $a^1\Pi$  state. *J. Mol. Spectr.*, 167(2), 334–352, (1994).
- [167] L. M. Beaty, V. D. Braun, K. P. Huber, and A. C. Le Floch. A high-resolution  $^{18}\text{O}$  isotope study in the vacuum ultraviolet of the  $A^1\Sigma - X^1\Sigma^+$  4th positive system of CO. *Astroph. J. Suppl. Ser.*, 109(1), 269, (1997).
- [168] C. M. Steinmann, E. G. Rohwer, and H. Stafast. Accurate laboratory wavelengths of the vacuum ultraviolet  $A(v' = 3) - X(v'' = 0)$  band of  $^{12}\text{C}^{17}\text{O}$  and  $^{12}\text{C}^{18}\text{O}$ . *Astrophys. J. Lett.*, 590(2), L123, (2003).
- [169] A. du Plessis, E. G. Rohwer, and C. M. Steenkamp. Accurate laboratory wavelengths of the  $a^1\Pi(v' = 0 - 5) - x^1\Sigma^+(v'' = 0)$  vibronic bands of  $^{12}\text{C}^{17}\text{O}$  and  $^{12}\text{C}^{18}\text{O}$ . *Astrophys. J. Suppl. Ser.*, 165(1), 432, (2006).
- [170] M. Eidelsberg, J.-Y. Roncin, A. L. Floch, F. Launay, C. Letzelter, and J. Rostas. Reinvestigation of the vacuum ultraviolet spectrum of {CO} and isotopic species: The B-X transition. *J. Mol. Spectr.*, 121(2), 309 – 336, (1987).
- [171] G. Stark, A. N. Heays, J. R. Lyons, P. L. Smith, M. Eidelsberg, S. R. Federman, J. L. Lemaire, L. Gavilan, N. de Oliveira, D. Joyeux, and L. Nahon. High-resolution oscillator strength measurements of the  $v' = 0, 1$  bands of the  $B - X$ ,  $C - X$ , and  $E - X$  systems in five isotopologues of carbon monoxide. *Astroph. J.*, 788(1), 67, (2014).

- [172] M. Eidelsberg, J. L. Lemaire, S. R. Federman, G. Stark, A. N. Heays, L. Gavilan, J. R. Lyons, P. L. Smith, N. de Oliveira, and D. Joyeux. High-resolution study of oscillator strengths and predissociation rates for  $^{13}\text{C}^{16}\text{O}$  and  $^{12}\text{C}^{18}\text{O}$ . *Astron. Astroph.*, 566, A96, (2014).
- [173] P. Cacciani, W. Ubachs, P. C. Hinnen, C. Lyngå, A. L'Huillier, and C.-G. Wahlström. Lifetime measurements of the  $E^1\Pi, v = 0$  and  $v = 1$  States of  $^{12}\text{C}^{16}\text{O}$ ,  $^{13}\text{C}^{16}\text{O}$ , and  $^{13}\text{C}^{18}\text{O}$ . *Astroph. J. Lett.*, 499(2), L223, (1998).
- [174] W. Ubachs, I. Velchev, and P. Cacciani. Predissociation in the  $E^1\Pi, v = 1$  state of the six natural isotopomers of CO. *J. Chem. Phys.*, 113(2), 547, (2000).
- [175] G. Klapper, F. Lewen, R. Gendriesch, S. P. Belov, and G. Winnewisser. Sub-doppler measurements and terahertz rotational spectrum of  $^{12}\text{C}^{18}\text{O}$ . *Zeitschr. für Naturf. A*, 56(3-4), 329–332, (2001).
- [176] G. Cazzoli, C. Puzzarini, and A. V. Lapinov. Precise laboratory frequencies for the  $J = 1-0$  and  $J = 2-1$  rotational transitions of  $\text{C}^{18}\text{O}$ . *Astrophys. J. Lett.*, 592(2), L95, (2003).
- [177] P. de Natale, M. Inguscio, C. R. Orza, and L. R. Zink. Far-infrared fourier transform spectroscopy of  $\text{C}^{12}\text{O}^{18}$ . *Astroph. J. Lett.*, 370, L53–L55, (1991).
- [178] J. A. Coxon and P. G. Hajigeorgiou. Direct potential fit analysis of the  $X^1\Sigma^+$  ground state of CO. *J. Chem. Phys.*, 121(7), 2992–3008, (2004).
- [179] E. J. Salumbides, M. L. Niu, J. Bagdonaite, N. de Oliveira, D. Joyeux, L. Nahon, and W. Ubachs. CO  $A-X$  system for constraining cosmological drift of the proton-electron mass ratio. *Phys. Rev. A*, 86, 022510, (2012).
- [180] M. L. Niu, E. J. Salumbides, A. N. Heays, N. de Oliveira, R. W. Field, and W. Ubachs. Spectroscopy and perturbation analysis of the  $(2,0)$ ,  $(3,0)$  and  $(4,0)$  bands. *Mol. Phys.*, 114(5), 627–636, (2016).
- [181] R. Hakalla, M. L. Niu, R. W. Field, E. J. Salumbides, A. N. Heays, G. Stark, J. R. Lyons, M. Eidelsberg, J. L. Lemaire, S. R. Federman, M. Zachwieja, W. Szajna, P. Kolek, I. Piotrowska, M. Ostrowska-Kopec, R. Kepa, N. de Oliveira, and W. Ubachs. VIS and VUV spectroscopy of

## Bibliography

- $^{12}\text{C}^{17}\text{O}$  and deperturbation analysis of the  $\text{A}^1\Pi, v = 1 - 5$  levels. *Roy. Soc. Chem. Adv.*, 6, 31588–31606, (2016).
- [182] A. J. de Nijs, D. Zhao, H. L. Bethlem, H. Linnartz, and W. Ubachs. Testing the mass-scaling relations in the  $\text{a}^3\Pi$  state of  $^{12}\text{C}^{18}\text{O}$  and  $^{13}\text{C}^{16}\text{O}$ . *J. Mol. Spectr.*, 292, 20–22, (2013).
- [183] W. Ubachs, K. S. E. Eikema, W. Hogervorst, and P. C. Cacciani. Narrow-band tunable extreme-ultraviolet laser source for lifetime measurements and precision spectroscopy. *J. Opt. Soc. Am. B*, 14(10), 2469–2476, (1997).
- [184] E. E. Eyler, A. Yiannopoulou, S. Gangopadhyay, and N. Melikechi. Chirp-free nanosecond laser amplifier for precision spectroscopy. *Opt. Lett.*, 22, 49–51.
- [185] R. Hakalla, W. Szajna, and M. Zachwieja. Extended analysis of the Ångström band system  $\text{B}^1\Sigma^+ - \text{A}^1\Pi$  in the rare  $^{12}\text{C}^{17}\text{O}$  isotopologue. *J. Phys. B*, 45(21), 215102, (2012).
- [186] R. Hakalla, M. Zachwieja, and W. Szajna. First analysis of the  $1v''$  progression of the Ångström  $\text{B}^1\Sigma^+ - \text{A}^1\Pi$  band system in the rare  $^{13}\text{C}^{17}\text{O}$  isotopologue. *J. Phys. Chem. A*, 117(47), 12299–12312, (2013).
- [187] R. Hakalla. First analysis of the Herzberg ( $\text{C}^1\Sigma^+ \rightarrow \text{A}^1\Pi$ ) band system in the less-abundant  $^{13}\text{C}^{17}\text{O}$  isotopologue. *Roy. Soc. Chem. Adv.*, 4, 44394–44407, (2014).
- [188] R. Hakalla, M. Zachwieja, and W. Szajna. First analysis of the  $\text{B}^1\Sigma^+$  ( $v=1$ ) Rydberg state in the lesser-abundant  $^{12}\text{C}^{17}\text{O}$  isotopologue on the basis of the  $1 - v''$  progression of the Ångström band system. *J. Quant. Spectr. Rad. Transfer*, 140, 7–17, (2014).
- [189] C. M. Western. PGOPHER: A program for simulating rotational, vibrational and electronic spectra. *J. Quant. Spectr. Rad. Transfer*, 186, 221–242, (2017).
- [190] N. de Oliveira, M. Roudjane, D. Joyeux, D. Phalippou, J.-C. Rodier, and L. Nahon. High-resolution broad-bandwidth Fourier-transform absorption spectroscopy in the VUV range down to 40 nm. *Nature Photon.*, 5, 149–253, (2011).

- [191] N. de Oliveira, D. Joyeux, M. Roudjane, J.-F. Gil, B. Pilette, L. Archer, K. Ito, and L. Nahon. The high-resolution absorption spectroscopy branch on the VUV beamline DESIRS at SOLEIL. *J. Synch. Rad.*, 23, 887–900, (2016).
- [192] J. L. Lemaire, M. Eidelsberg, A. N. Heays, L. Gavilan, S. R. Federman, G. Stark, J. R. Lyons, N. de Oliveira, and D. Joyeux. High-resolution spectroscopy of the  $A^1\Pi(v' = 0 - 10) - X^1\Sigma^+(v'' = 0)$  bands in  $^{13}\text{C}^{18}\text{O}$ : term values, ro-vibrational oscillator strengths and Hönl–London corrections. *J. Phys. B*, 49(15), 154001, (2016).
- [193] M. L. Niu, A. N. Heays, S. Jones, E. J. Salumbides, E. F. van Dishoeck, N. de Oliveira, L. Nahon, and W. Ubachs. VUV-synchrotron absorption studies of  $\text{N}_2$  and  $\text{CO}$  at 900 K. *J. Mol. Spectr.*, 315, 137–146, (2015).
- [194] H. Lefebvre-Brion and R. W. Field. *The spectra and dynamics of diatomic molecules*. Elsevier, Amsterdam, (2004).
- [195] M. Larsson. Conversion formulas between radiative lifetimes and other dynamical variables for spin-allowed electronic transitions in diatomic molecules. *Astron. Astrophys.*, 128, 291–298, (1983).
- [196] M. Drabbels, J. Heinze, J. J. ter Meulen, and W. L. Meerts. High-resolution double-resonance spectroscopy on Rydberg states of  $\text{CO}$ . *J. Chem. Phys.*, 99(8), 5701–5711, (1993).
- [197] A. C. Le Floch, F. Launay, J. Rostas, R. W. Field, C. M. Brown, and K. Yoshino. Reinvestigation of the  $\text{CO } A^1\Pi$  state and its perturbations: The  $v = 0$  level. *J. Mol. Spectrosc.*, 121(2), 337–379, (1987).
- [198] C. Haridass and K. P. Huber. A high-resolution C-13 isotope study in the vacuum ultraviolet of spectra of  $\text{CO } (A - X)$ ,  $\text{C I}$ , and  $\text{C II}$ . *Astroph. J.*, 420, 433–438, (1994).
- [199] R. W. Field. *Spectroscopy and Perturbation Analysis in Excited States of CO and CS*. PhD thesis, Harvard University, (1971).
- [200] S. G. Tilford and J. D. Simmons. Atlas of the observed absorption spectrum of carbon monoxide between 1060 and 1900 Å. *J. Phys. Chem. Ref. Data*, 1, 147–188, (1972).

## Bibliography

- [201] K. P. Huber and G. Herzberg. *Constants of diatomic molecules*. Van Nostrand Reinhold, New York, (1979).
- [202] C. Kittrell and B. A. Garetz. Analysis of the  $D^1\Delta - X^1\Sigma^+$  transition in CO observed by two-photon excitation. *Spectrochim. Acta*, 1(45), 31–40, (1989).



## List of publications

The following publications are reproduced as chapters in this thesis:

**Chapter 2:** T. M. Trivikram, M. L. Niu, P. Wcisło, W. Ubachs, and E. J. Salumbides

‘Precision measurements and test of molecular theory in highly excited vibrational states of  $\text{H}_2(v = 11)$ ’.

*Applied Physics B* **122**, 294 (2016).

**Chapter 4:** M. Schlösser, X. Zhao, T. M. Trivikram, W. Ubachs, and E. J. Salumbides

‘CARS spectroscopy of the  $(v = 0 \rightarrow 1)$  band in  $\text{T}_2$ ’.

*Journal of Physics B: Atomic, Molecular and Optical Physics* **50**, 214004 (2017).

**Chapter 5:** T. M. Trivikram, M. Schlösser, W. Ubachs, and E. J. Salumbides

‘Relativistic and QED Effects in the Fundamental Vibration of  $\text{T}_2$ ’.

*Physical Review Letters* **120**, 163002 (2018).

**Chapter 6:** T. M. Trivikram, R. Hakalla, A. N. Heays, M. L. Niu, S. Scheidegger, E. J. Salumbides, N. de Oliveira, R. W. Field, and W. Ubachs

‘Perturbations in the  $A^1\Pi, v = 0$  state of  $^{12}\text{C}^{18}\text{O}$  investigated via complementary spectroscopic techniques’.

*Molecular Physics* **115**, 3178-3191 (2017).

**The author also contributed to the following publications:**

- (ii) R. Hakalla, T. M. Trivikram, A. N. Heays, E. J. Salumbides, N. de Oliveira, R. W. Field, and W. Ubachs  
'Precision spectroscopy and comprehensive analysis of perturbations in the  $A^1\Pi(v = 0)$  state of  $^{13}\text{C}^{18}\text{O}$ '.  
*Molecular Physics* **117**, 79-96 (2019).
- (i) M. L. Niu, R. Hakalla, T. M. Trivikram, A. N. Heays, N. de Oliveira, E. J. Salumbides, and W. Ubachs  
'Spectroscopy and perturbation analysis of the  $A^1\Pi(v = 0)$  state of  $^{13}\text{C}^{16}\text{O}$ '.  
*Molecular Physics* **114**, 2857-2867 (2016).

## Acknowledgements

First I am thankful to my promoter Prof. Wim Ubachs for providing an opportunity to work at LaserLaB Amsterdam. I admire at your passion for science and diligence in dealing with different scientific problems at the same time, from precision molecular spectroscopy to astrophysics at VU and laser-produced plasmas at the other research institute in Amsterdam.

I am grateful to my co-promotor Dr. Edcel Salumbides, a one-stop solution for the experimental issues in the lab. Your enthusiasm and dedication towards the laser spectroscopy inspired me a lot. The discussions with you in the lab helped me to make the progress in the experiments and to hold my nerve during the difficult times.

I want to acknowledge our collaborators who made important contributions to this work. Magnus Schlösser for the CARS studies on the molecular tritium, Piotr Wicłó for line shape analysis of the ac-Stark broadened REMPI spectra and Rafal Hakalla for the perturbation studies on the CO isotopologues.

I am lucky to be assisted by the highly-motivated masters students in different experiments. Simon Scheidegger, Xiadong Zhao, and Meissa Diouf thank you for your assistance and I wish you all the best for your doctoral studies.

I want to express my gratitude to Rob Kortekaas, the technical workhorse of the group, who has always been quick to respond to the technical issues.

It gives me immense pleasure to acknowledge the support of the other group members. I am fortunate to be associated with Sayan Patra. Besides a fellow Indian, Sayan is like a younger brother. Special thanks Adonis Flores and Cunfen Chen for their support. Many thanks to Xavier, Frank, Jowel, Mingli, Yuanqing, Bob, Ruud, and other colleagues for your cooperation in making a smooth stay for me at VU.

## 6 Acknowledgements

Finally, I want to acknowledge the continuous support and understanding of my family members, especially to my mother and my wife Anupama, to whom I dedicate my thesis.



